1-1-1981

The interaction of HII regions with molecular clouds.

John, Bally
University of Massachusetts Amherst

THE INTERACTION OF HII REGIONS WITH MOLECULAR CLOUDS

A Dissertation Presented

By

JOHN BALLY

Submitted to the Graduate School of the
University of Massachusetts in partial fulfillment
of the requirements for the degree of

DOCTOR OF PHILOSOPHY

February 1981

Department of Physics and Astronomy

THE INTERACTION OF HII REGIONS WITH MOLECULAR CLOUDS

A Dissertation Presented

By

JOHN BALLY

Approved as to style and content by:

Dr. Nicholas Z. Scoville, Chairman of Committee

Dr. G. Richard Huguenin, Member

Dr. Paul Goldsmith, Member

Dr. Robert V. Krotkov, Member

Dr. Edward R. Harrison, Member

Dr. David Van Blerkom, Department Head
Department of Astronomy

ACKNOWLEDGEMENTS

I would like to express my thanks to the many people who made this thesis possible. I wish to thank Nick Scoville, whose encouragement, support, and critical evaluations guided me through the course of this work. This research was made possible by the efforts of G.Richard Huguenin, director of the FCRAO, whose enthusiastic support was invaluable. Many individuals contributed, either directly or indirectly to this project through scientific discussions, suggestions, and assistance. Special thanks go to Bill Langer, Paul Goldsmith, and Tom Arny. John Kapitzky helped in innumerable ways at Quabbin during many observing runs. I would like to express my deepest appreciation to the FCRAO staff who helped with fixing and running receivers, filterbanks, and all the tools used in mm wavelength astronomy. Special thanks to Steve Lord who spent many a night trying to resurrect the correlator. I also acknowledge the help of Dick Joyce of KPNO who's help led to the success of our infrared runs.

ABSTRACT

The Interaction of HII Regions with Molecular Clouds

(February 1981)

John Bally, B.A.,University of California, Berkeley
M.S.,Ph.D.,University of Massachusetts,Amherst

Directed by: Professor Nicholas Z. Scoville

The energetics and dynamics of molecular gas associated with HII regions are investigated. Six sources were selected for detailed study from a survey of fifty relatively nearby Sharpless HII regions. The energetics of the molecular cloud boundary layer was probed by CO line observations. In S87, S155-Cepheus B, and S125 the radiation field is too weak and the gas density is too small to heat the cloud edge to the observed temperature by means of gas-dust collisions. A new energy input mechanism for the molecular gas is postulated; direct heating of the gas by photoelectrons ejected from grains by the intense UV radiation available just outside HII regions.

Several of the youngest HII regions are young biconical nebulae (e.g. S87 and S106) whose peculiar morphology reflects the initial conditions in which isolated stars can form. In S106 a ridge of molecular emission is interpreted as a massive ($100M_o$) disk constraining the development of the HII region. The model of disk constrained HII regions can explain the observed high velocity outflows observed in

the ionized gas associated with S106 and explain the hourglass shape of the nebula. Dense neutral gas close to the star (the inner disk) supplies the HII region with freshly ionized plasma. A diverging high velocity (V_{exp} ~ 30 -40 km s^{-1}) outflow of gas develops, removing plasma from the dense inner region.

In more-evolved HII regions (S184, S155-Cepheus B), shock waves are seen as doppler shifted spectral line components whose location correlates well with the distribution of high electron density plasma. In several of the oldest regions studied (S125 and S117), large amounts of gas have been swept up by the post shock layer. In the Pelican Nebula (S117), 3 -6x10^4 M_o of gas is distributed in an expanding shell of gas that has been accelerated by the rocket effect to a velocity of V = 5 km s^{-1}. The development of an HII region can disrupt the associated molecular cloud. Although some of the mass is dissociated or ionized, much material can survive in the molecular state as accelerated cloud fragments.

TABLE OF CONTENTS

LIST OF TABLES

LIST OF FIGURES

Note: Unless otherwise indicated, all angular coordinates are in units of equatorial arcminutes ($1' = 4^s$ - independent of Declination. Forshortening correction ($\cos \delta$) is not applied. All velocities in spectra and spatial-velocity diagrams are in units of km s^{-1}.

C H A P T E R I

INTRODUCTION

A. Overview

The picture of star formation as the gravitational collapse of interstellar clouds is generally accepted, yet many fundamental aspects of the process are not understood. Both observations and theoretical evidence support the view that shock waves passing through molecular clouds trigger star formation. Star-forming shocks could be generated by supernovae (Herbst and Assousa 1977), the spiral density wave (Woodward 1976), cloud-cloud collisions (Loren 1976), stellar winds (Castor et al. 1978), or expanding ionization fronts of HII regions (Elmegreen and Lada 1977). Shock waves associated with the expansion of HII regions are ideally suited for investigation since their presence is expected to be marked by ionization fronts. The interaction between ionized and molecular gas at the boundary of an HII region reveals the properties of the dense gas out of which stars form. The dynamic evolution of older HII region complexes reflects the processes by which star forming clouds are dispersed or destroyed.

Understanding of the dynamical evolution and thermodynamics of giant molecular clouds has been hampered by the lack observations of structurally simple clouds against which to test models. In the well-known giant clouds such as Orion, M17, and W3, many sources of energy

exist at different locations in the cloud, while in the smaller dark clouds such as those in Taurus, no distinctive energy sources occur. In the former clouds, diverse objects such as HII regions, low and high mass stars, and numerous infrared sources confuse the relationship between exciting sources and the observed energetic and kinematic properties. The complicated morphology of HII regions and molecular clouds reflects the importance of stochastic phenomena in their development. The structure and evolution of planetary nebulae and supernovae remnants are dominated by well-organized flows which give rise to simple shapes such as spherical shells. HII regions and molecular clouds, on the other hand, exhibit more chaotic forms and less organization in their kinematics. This chaotic behavior has hampered our understanding of star formation and its effects on surrounding gas.

In this thesis, the interaction between HII regions and surrounding molecular clouds is investigated. Millimeter wavelength emission lines of CO, CS, HCN, and C_2H were observed in order to probe the velocity fields, temperatures, and densities of the clouds associated with a number of relatively nearby Sharpless HII regions (Sharpless 1959). Near-infrared observations were made to locate potential protostars, heating sources for the molecular gas, and hidden early type stars that may contribute to the excitation of the associated nebulae. The observational phase has resulted in the detection of numerous CO hot spots with no obvious internal heat sources, a massive neutral disk surrounding the central star of a biconi-

cal HII region, examples of ionization front driven shocks, and expanding shells of molecular gas surrounding the more evolved nebulae. These discoveries have led to theoretical modeling of the heating of the boundary layer between molecular clouds and HII regions, an analysis of young disk-constrained nebulae, and a discussion of the evolution of the post-shock layer when the ionized gas expands beyond the confines of the original molecular cloud.

B. The Observations

The identification of relatively simple sources to be studied in detail started with the selection of HII regions from the list of optical nebulosities catalogued by Sharpless (1959). An initial list containing 60 regions (see Appendix I) was compiled on the basis of the strength of the observed thermal radio continuum emission as reported in the observations of Churchwell and Felli (1972). The appearance of each region on the Palomar Sky Survey (PSS), along with an estimate of the excitation based on the free-free data, was used so as to include both high and low excitation nebulae in diverse evolutionary states.

The millimeter wavelength observations were made with the Five College Radio Astronomy (FCRAO) 14 meter telescope located at the Quabbin Reservoir in New Salem, Massachusetts. This instrument has a half-power beamwidth of 44 arcsec at 115 GHz, the frequency of the strong CO J=1-0 transition.

The initial source list was observed in ^{12}CO during the Spring of 1978 by mapping 5 to 9 points per source in order to identify the associated molecular clouds. This survey phase led to the compilation of a subset of sources exhibiting spectral line shape changes or high temperatures that may indicate interaction with nearby HII regions. The follow-up list, used in a more detailed study, was biased towards sources that had been observed with the Westerbork aperture synthesis telescope by Felli et al. (1978). These radio continuum maps give high spatial resolution information on the density and distribution of the ionized gas. A program of more extensive CO mapping for the sources in the second list was started in April 1978. Maps were made for six sources in ^{12}CO and for three sources in ^{13}CO ; partial ^{12}CO maps were made for an aditional six regions.

A third phase of observations studied the hot emission regions located in the ^{12}CO work. These regions were observed in the microwave transitions of high excitation molecules such as HCN, CS, and C_2H, and were also searched for buried near-infrared sources and for 22 GHz water vapor maser emission. All infrared observations were obtained with the KPNO 1.3 m telescope, using the Joyce InSb detector in either a dewar containing a cooled grating spectrometer ($/\Delta\lambda$ = 500), or a dewar containing a circular variable filter ($\lambda/\Delta\lambda$ = 70) and standard IJHKLMN broadband photometric filters. The 120 ft NEROC antenna in Westford Massschusetts was used in April 1979 to search for water masers in the vicinity of CO hot spots. The presence of near IR sources and H_2O masers in molecular cloud cores may be taken as evidence of recent star formation activity (Genzel and Downes 1978).

Detailed results of the observational program are presented in Chapter II. Appendix I describes the survey observations. Observing and data reduction methods are discussed in Appendix II.

C. Theory

The six HII regions studied in detail in this work cover a wide range in physical size, electron density, and evolutionary state. Inasmuch as these sources can be sorted in terms of relative age, a simple pattern emerges. The young, compact HII regions tend to be surrounded with molecular clouds that show enhanced heating effects but little evidence of gas dynamic disturbance due to interaction with the ionized gas. On the other hand, older highly evolved regions exhibit pronounced effects of dynamic interaction. Enhanced heating in the older complexes is more or less restricted to those parts of the molecular cloud that are bathed in strong ultraviolet radiation from hot, young stars.

The theory of photoelectric heating of the molecular boundary layer by intense UV from massive stars associated with HII regions is discussed in Chapter III. This effect may be responsible for the enhanced temperatures observed near young HII regions, where the total available radiative flux is insufficient to heat dust grains to a high enough temperature to provide the observed heating of the gas.

Several of the young regions, namely S87, S106, and LkHα208, are biconical nebulae exhibiting two lobes of luminous gas

symmetrically located around the exciting star (Calvet and Cohen 1978). This configuration may indicate the presence of a nearly edge on circumstellar disk that obscures the central star and permits radiation to escape preferentially along the disk axis. Until the disk evaporates, the evolution of the HII region is very different from that of a Stromgren sphere. A simple model for the ionization structure and development of an HII region containing a massive molecular disk is presented in Section IV.A. Highly supersonic gas flows that have been observed in S106 and other regions can be readily explained in terms of the divergent isothermal flow of ionized gas ablating from the disk.

The older HII region complexes studied here, such as S125, S155, S184, and S117, exhibit abrupt transitions in their velocity fields that may indicate the presence of shocks associated with expanding ionization fronts driven by the high pressure of the ionized gas. The theory of the development of ionization shock front systems in a late evolutionary phase of an HII region, when the hot ionized bubble has burst through the nearest cloud boundary, is analyzed in Section IV.B. After the bulk of the original molecular cloud has been accumulated in a post-shock layer, the rocket effect becomes effective in accelerating the gas. The velocity fields seen in these regions imply dispersal of the intial clouds that gave birth to the exciting stars. On a galactic scale, HII region expansion may provide the dominant mechanism by which molecular clouds are disrupted and dispersed. The model is used to explain the expanding molecular cloud network observed surrounding the Pelican nebula in Cygnus.

D. Background

1. Molecular Clouds

Surveys of the galactic plane in the CO molecule have revealed the presence of about 3,000 giant molecular clouds with masses in the range 10^5 to 10^6 solar masses, distributed in an annulus with an inner radius of 4 kpc and a more diffuse outer boundary at 8 to 12 kpc (Scoville and Solomon 1975, Burton and Gordon 1975, Solomon Sanders snd Scoville 1980). The total mass of all molecular gas in the galaxy is about $M(H_2)=2x10^9$ M_o concentrated into clouds with mean densities around n= 200 cm^{-3}. These clouds may contain most of the non-stellar mass in the galaxy inside the solar circle, yet this component occupies only about 0.3 % of the volume of the galactic disk.

Molecular clouds appear to be gravitationally bound. The free-fall collapse time for gas at the density n=500 cm^{-3} is $t_{ff}= 1/\sqrt{G\rho} \sim 10^6$ yrs. At this rate, the conversion of giant molecular clouds into stars ought to be $dM_*/dt = M(H_2)/t_{ff} \sim 10^3$ M_o yr^{-1} , over 100 times the observed star formation rate for the galaxy as a whole (Smith et al. 1979). There must be some internal support mechanism such as magnetic pressure or rotation (Field 1978 ,Muschovias 1976) that prevents cloud collapse. Star formation occurs when the supporting pressure is overcome, possibly by the application of an external source of pressure such a shock wave.

2. The Relationship Between Molecular Clouds and HII Regions

Surveys of CO emission in the direction of galactic HII regions have shown that molecular clouds are always present in the same area of the sky (Liszt 1973, Wilson et al. 1974, Blair et al. 1975), usually at a velocity close to the velocity of the ionized gas (Israel F.P. 1979). Although the centers of molecular clouds are expected to have the highest density and be most unstable to gravitational collapse and star formation, the ionized gas is generally found at the edges of molecular clouds. Extinction effects can not explain this since HII regions selected from radio surveys also exhibit the preferential location of ionized gas near cloud surfaces. Two classes of models can explain this effect: 1) Massive star formation may preferentially occur near the cloud surface; 2) Massive star formation occurs near cloud centers, but the resulting hot ionized cavity rapidly percolates to the nearest cloud boundary, where it spends most of its observable life. Either the preferential growth of the HII region in the direction of fastest density decrease, or motion of the exciting star relative to the cloud, may result in the rapid surfacing of the HII region.

Studies of several nearby OB associations indicate that massive star formation in a given complex occurs over an extended period of time ($\sim 10^7$ yrs) (Blaauw 1955). In the Orion complex, as well as in the W3 - W4 complex, there appears to be a progressive sequence of stellar ages in the associations from one side of the complex to the

other. The molecular clouds and sites of ongoing star formation are located on the side of the association where the youngest stars are found (Kutner et al. 1977, Lada et al. 1978). These regions give the impression that a wave of star formation has propagated through a primordial giant molecular cloud at roughly $v = 5$ km s^{-1} (Elmegreen and Lada 1977). The idea of sequential star formation, where young OB stars lead to the development of an ionization-driven shock front in which further OB stars are born, has been developped in some detail. This model can explain the tendency for HII regions to be found near cloud surfaces, as well as the sequence of stellar ages found in associations. However, not all OB stars form in this way, since the chain reaction is not self-starting and isolated HII regions with a single exciting star are seen. These isolated stars form either without the aid of shock compression, or the shocks are caused by an agent other than ionization fronts. Furthermore, velocity shifts that are the expected signature of shocks have never been seen in these regions.

3. The Dynamical Evolution HII Regions

The early theoretical analysis of the development of HII regions assumed that the UV-emitting massive stars are born in a uniform density, homogeneous, neutral medium, not a realistic description of the ISM as it is known today. The value of this work lies in the systematic description of the development of ionization fronts and their associated shock waves (Oort 1954, Kahn 1954) and in the analysis of evolving Stromgren spheres (Pottasch 1958, Mathews and O'Dell

1969, Spitzer 1978). In these models, the initial burst of UV photons from a recently formed OB star sends a wave of ionization propagating supersonically (relative to the speed of sound C_{II} in the ionized gas behind the front) through the neutral gas. This is a weak R-type front (R for rarefied) when the front velocity is greater than $2C_{II}$. As the UV flux decreases at the position of the outward moving front due to absorption and geometric dilution, the front velocity decreases. When V_I falls below $2C_{II}$, a shock separates from the I-front and precedes it into the undisturbed gas. The post-shock gas is compressed and accelerated outward so that relative to it, the I-front is moving subsonically. Since the outward moving post-shock layer is much denser than the undisturbed gas, the front is called D-type (for dense).

Observations of HII regions have shown that spherical models can only be regarded as a crude approximation. The disagreement between data and simple models has emerged step by step as various workers have found results that contradict the predictions of the simple models (Wilson et al. 1959, Munch 1958, Meaburn 1971, Osterbrock 1974). In many regions, highly asymmetric ionized gas flows with supersonic velocities are seen, indicating that inhomogeneous initial conditions must be considered.

Recent hydrodynamical calculations (Tenorio-Tagle 1979, Bodenheimer et al. 1980, Tenorio-Tagle et al. 1980) have considered the details of the ionized gas flows and shock-front systems when an HII region develops at the edge of a dense cloud. The essential

feature of the asymmetric models is that at some point the ionization front reaches the cloud boundary, where the neutral gas density may drop by several orders of magnitude. The high pressure, ionized gas then flows into the intercloud medium which has a much lower pressure. The high velocity outflow of plasma can form a strong shock in the intercloud medium. The effect of this flow on the initial Stromgren sphere is the propagation of a rarefaction wave back into the dense part of the nebula, draining plasma from it. The diverging flow from the depressurizing ionized cavity can become highly supersonic with an asymmetric velocity field, in agreement with high spectral resolution observations of emission line profiles seen in many nebulae (Meaburn 1973).

The formation of an HII region can lead to some phenomena that may be revealed by mm-wavelength molecular line observations. The post-shock layer associated with a weak D-type ionization shock front system may be detectable in molecular transitions once enough gas has been swept up to trap the advancing dissociation wave that precedes the I-front within the post-shock layer. In evolved HII regions, the post shock gas should have a velocity of expansion relative to the undisturbed gas amounting to a few km s^{-1} and may be detectable as a doppler shifted line component. In large complexes, much momentum may be transferred to the molecular gas by the growing ionized bubble.

The eventual outcome of the dynamic interaction between an evolving HII region and its parent molecular cloud must depend on the

balance between the tendency of a cloud to collapse under gravity after the passage of a disturbance, and the capacity of internal pressure to prevent collapse. If parts of the cloud respond to the growth of the HII region by collapsing, induced star formation may be the consequence. If internal cloud support prevents collapse, the perpetual outward push of the nebula may result in fragmentation, disruption, and eventual dispersal of the parent molecular cloud.

4. Energetics of the Molecular Boundary Layer

Most molecular clouds are permeated by cosmic rays that by virtue of their ionization, deposit energy in the gas. The balance between this input and losses due to radiation in the rotational transitions of molecules, mainly CO, gives an equilibrium gas kinetic temperature of T_k = 10 °K (Goldreich and Kwan 1974). When additional radiation is present, either from an imbedded star or from the outside, the dust grains heat up to a radiative equilibrium temperature. Collisions of molecules with the warm grains provide energy for the gas and can raise the temperature to T_k = 100 °K in the vicinity of luminous sources (Goldreich and Kwan 1974, Scoville and Kwan 1976).

When shocks propagate through the gas, some of the energy will go into heating molecules in the post-shock layer. Rapid cooling will, however, quickly dispose of the excess energy and return the gas to a radiative equilibrium temperature, unless the shock energy can be stored and slowly released into the gas. If magnetic fields thread the gas, magnetic ion slip, or the dissipation of hydromagnetic tur-

bulence can heat the gas (Black and Lada 1978, Elmegreen et al. 1978). The decay of hydrodynamic turbulence can also result in a significant heat input if it can be regenerated. A review of cloud heating mechanisms is given by Goldsmith and Langer (1978). The molecular boundary layer at the edge of an HII region is subject to very large fluxes of UV radiation, some of which can be used to heat the gas directly by means of energetic photoeletrons liberated from grains.

C H A P T E R II

THE OBSERVATIONS

In this Chapter, the results of the observational program investigating the properties of molecular clouds associated with six HII regions are presented. The results of the survey observations that led to the selection of these sources are presented in Appendix I and the methods of data aquisition and reduction are discussed in Appendix II. The regions are presented in chronological sequence from the youngest to the oldest and include S87, S106, S125, S117, S184, and S155. These HII regions cover a wide range of excitation conditions ranging from central stars of spectral type later than B0 to earlier than O5. The youngest regions may be as young as 10^4 yrs, while the more evolved regions may be as old as 6×10^6 yrs.

A. The Chronological Sequence

Even in the absence of a detailed and realistic theory for the evolution of HII regions, radio observations of the ionized gas can be used to arrange these complexes in a rough chronological sequence based on the theory of evolving Stromgren spheres. After the very rapid initial ionization of the ambient neutral cloud of uniform proton density n_o out to an initial Stromgren radius R_o, the radius of the HII region evolves with time as

$$R_{II} = R_o \left(1 + 7C_{II}t / 4R_o \right)^{4/7} \qquad (1)$$

where $C_{II} = 10$ km s^{-1} is the isothermal sound speed in the ionized gas (Spitzer 1978). The parameters readily determined from the radio observations are the emission measure $E = n_e^2 L$ and the angular radius of the HII region θ_{II}, which can be converted into an actual radius if the distance is known. The age of the region in terms of E and R_{II} and the initial density n_o is

$$t = 1.2 \times 10^5 \left(\frac{n_o}{10^3 cm^{-3}} \right)^{1/2} \left(\frac{R_{II}}{1 \text{ pc}} \right)^{5/4} \left(\frac{E}{10^5 cm^{-6} pc} \right)^{-1/4} \qquad (2)$$

It is assumed that the region is rougly spherical so $L = 2R_{II}$. The value of n_o and the distance must be determined from the millimeter wave emission of surrounding gas and the optical properties of the region. Table 1 gives the age parameter and the values used to determine it for the six regions discussed. Equation (2) is useful because it does not depend on Q, the flux of Lyman continuum photons, so that observations of the exciting stars are not required.

B. Techniques

Observation of a variety of molecular transitions in the mm-wavelength range, hydrogen recombination and continuum in the near infrared, and a search for H_2O maser emission were used to probe the physical nature and state of evolution of the molecular clouds associated with the HII regions. The mass, extent, and temperature of the

TABLE 1

AGE PARAMETERS FOR SIX HII REGIONS

Source	R_{II}(pc)	E(cm^{-6}pc)	t(yrs)*	Comments
S87	0.07	1.8×10^5	4×10^3	Compact core
S106	0.15	3×10^3	3×10^4	
S117	20	3×10^3	1.4×10^7	
S125	3.9	3.7×10^3	1.4×10^6	
S184	16	8.4×10^3	1.4×10^6	Free-free emission dominated by compact features in both S184 and S155
S155	8.5	8.7×10^3	3×10^6	

* An initial cloud proton density n_o = 500 cm^{-3} is assumed.

clouds were determined from the 2.6 mm CO line. The ^{12}CO line at 115 GHz is usually optically thick and thermalized in molecular clouds (Penzias 1975), so it is a good indicator of the temperature distribution of the gas. Since this is the strongest and easiest to detect mm-wavelength spectral line, mapping in this transition was used to delineate the cloud shape, size, and velocity field. Four of the clouds were mapped in the 110 GHz ^{13}CO line, which usually has a small optical depth and is useful for the determination of column densities. Calculation of column densities will be discussed in detail in Appendix II. Cloud mass estimates were made using the CO cloud size and the dervied H_2 column densities.

Molecules with large dipole moments and low relative abundance are good tracers of the high density ($n = 10^5$ cm^{-3}) gas usually found in active molecular cloud cores (Scoville and Solomon 1974, Goldsmith and Linke 1980). Several molecular transitions were observed. The 89 GHz line of HCN, the 98 GHz J = 2-1 and 49 GHz J = 1-0 transitions of CS, and the 87 GHz N = 1-0, F = (3/2,2) - (1/2,0) transition C_2H were observed in several cloud cores. The molecule C_2H may be particularily suited to probe the boundary layer since its abundance is expected to be largest at the cloud surface where the UV flux is high (Langer 1976).

Water vapor masers are often found in sites of star formation (Genzel and Downes 1977, Rodriguez et al. 1979). A search for masers at 22 GHz under adverse weather conditions resulted in the discovery

of a maser associated with S87 IRS1. Near-infrared observations were undertaken in order to locate energy sources associated with molecular cloud hot spots. A search for the Bracket γ hydrogen recombination line was used as a probe of embedded ultra-compact HII regions.

C. S87

S87 is one of the hottest sources found during the initial CO survey. Its well-resolved hot spot exhibits simple structure suggesting that this may be a good source for investigation of the energetics of molecular clouds containing young HII regions. The velocity of the associated molecular cloud implies a kinematic distance of 2 kpc. On the Palomar Sky Survey plates, S87 appears as a faint patch of diffuse nebulosity 10 arcmin in diameter centered on a bright knot. Recent observations by Cohen (1979) show the compact object to be a symmetrical biconical HII region with its exciting star partially hidden by a dust lane. Aperture synthesis maps obtained at Westerbork (Felli and Harteen 1978, Israel 1979) show two compact HII regions. The stronger source, coincident with the nebulous knot, has a flux density of $S_{5\ GHz}$= 240 mJy and a size 21 x 39 arcsec. The second source, located 60 arcsec to the northeast, has $S_{5\ GHz}$= 45 mJy and a size 10 x 25 arcsec but does not have an optical counterpart. The flux of Lyman continuum photons required to ionize the stronger source is $Q = 3 \times 10^{47}$ photons s^{-1}, corresponding to a B0 type star on the main sequence (Kurutz 1979, Osterbrock 1974). The AFGL catalog (Price and Walker 1976, Davis et al. 1979) shows a bright 20 micron

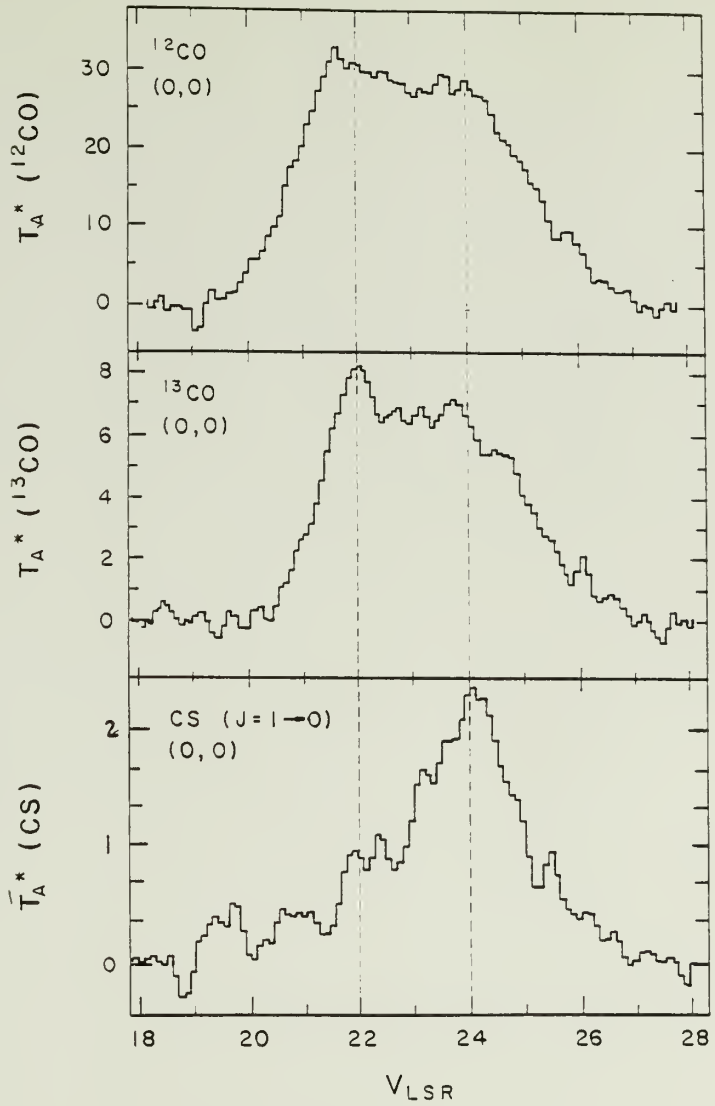

Figure 1

Line profiles seen in the direction of the S87 molecular peak: Top, ^{12}CO. Middle, ^{13}CO. Bottom, CS(1-0). Note that the higher excitation CS line peaks at a different velocity than the lower excitation CO lines.

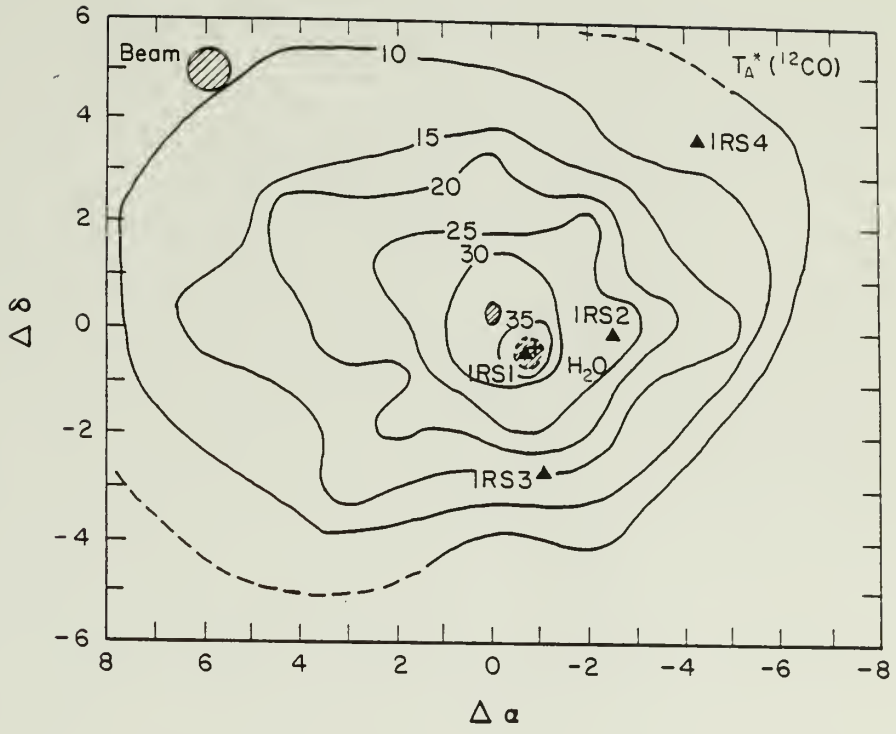

Figure 2

^{12}CO map of S87. The axes are labled with equatorial arc-minutes referred to the (0,0) position at $\alpha_{1950} = 19^h44^m16^s$ $\delta_{1950} = 24°28'28''$. The hatched ovals mark the compact HII regions. The cross is the H_2O maser, triangles mark the near-infrared sources.

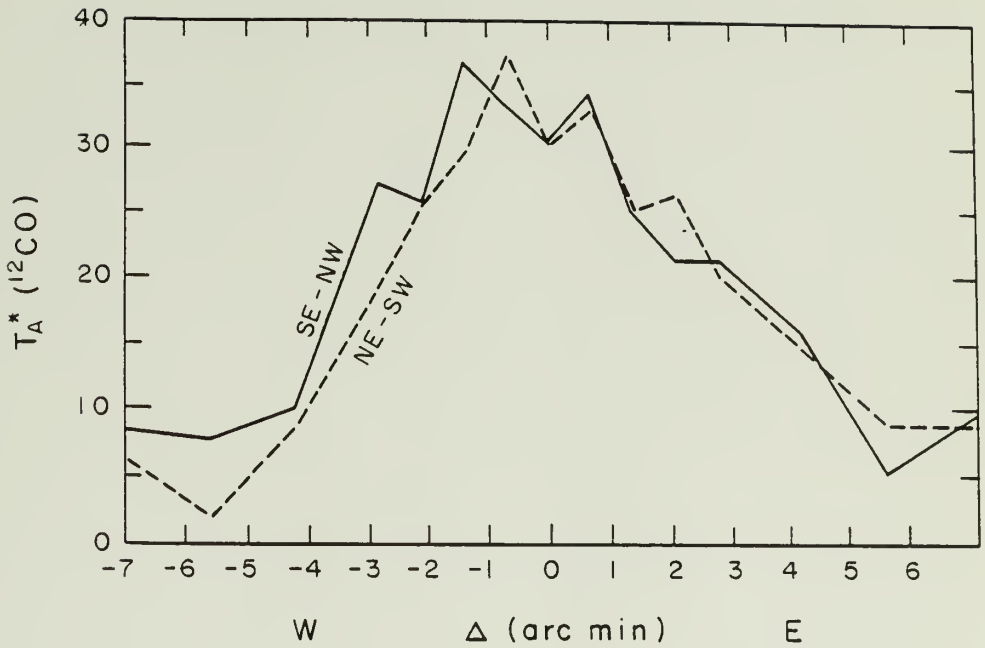

Figure 3

Peak ^{12}CO line temperatures of the S87 hot spot measured during one observing run. The solid line corresponds to a southeast to northwest diagonal strip while the dashed line is a strip in the orthogonal direction. Both strips intersect at the (0,0) position.

source CRL 2454 near S87. A search of the region at 4 microns (see Section II.C.4) led to the discovery of S87 IRS1, a very red object located at the position of the stronger radio feature, which is probably the near IR counterpart of CRL 2454.

1. CO

The CO distribution is centered at the position of the 240 mJy radio source, where a peak temperature of T_A= 32 °K is reached at V_{LSR}= 22 km s^{-1}. The kinematic distance to this velocity is 2 kpc. Line profiles at the reference position, which is located 30 arcsec from the CO peak, are shown in Figure 1. The CO temperature drops rapidly in all directions, as can be seen from the nearly circular contours in the map (Figure 2). The low-level contours exhibit a slight elongation in the east-west direction. The temperature profiles along strips running northeast-southwest and northwest-southeast through the hot spot are illustrated in Figure 3. The CO temperature drops to under 10 °K at an angular distance of 4 to 7 arcmin from the cloud center indicating a diameter of about 7 pc at the 10°K level.

In order to determine the gas density, the lower opacity ^{13}CO line was measured at 44 positions in the S87 molecular cloud. Figure 1 shows that the ^{12}CO and ^{13}CO spectra at the (0,0) reference position are identical in shape, indicating that even the rarer isotopic species may also be optically thick in the cloud core. A contour map of the integrated ^{13}CO line profile, shown in Figure 4, gives a ^{13}CO

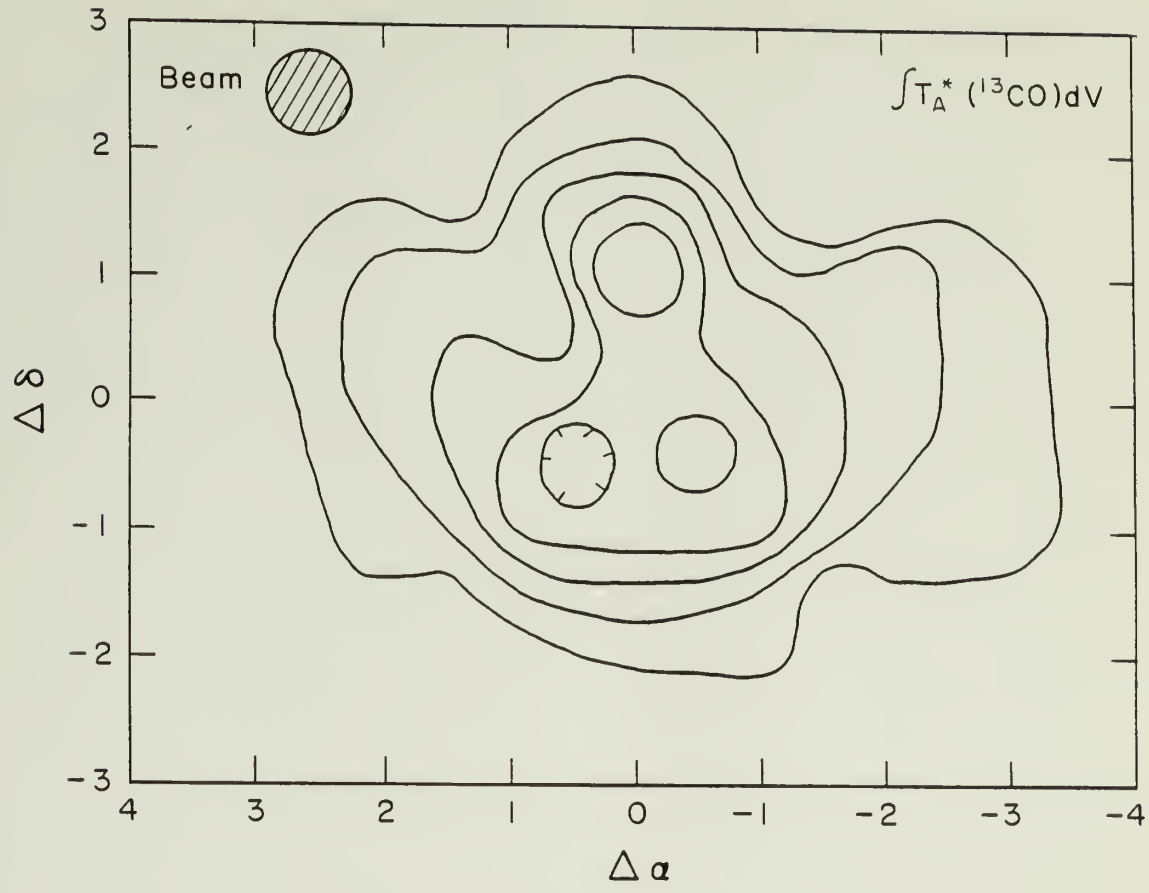

Figure 4

^{13}CO map of S87. Contours correspond to the integral under the line profile and are given by 10,15,20,25,and 30 °K km s^{-1}.

cloud diameter of 3.6 pc (at the 2°K level). The larger extent of the ^{12}CO emission suggests the presence of an extended low column density halo of molecular gas where the ratio $T(^{13}CO)/T(^{12}CO)$ is smaller than 1/10. Using a value of 4.0 km s^{-1} for the half-power full width of the ^{12}CO profile at the (0,0) position and a diameter of 3.6 pc for the cloud, the Virial Theorem gives a cloud mass estimate of $M = 4 \times 10^3$ M_o. (Kinematic disturbances may broaden the line profiles near an HII region, however, resulting in overestimates of the mass.) Using the formalism outlined in Appendix II, an H_2 column density of $N(H_2) = 7 \times 10^{22}$ cm^{-2} at the peak position is calculated. From the CO lines, assuming that the cloud is spherical and of uniform density with a diameter of 3.6 pc, a mean H_2 density $n(H_2) = 6 \times 10^3$ cm^{-3} is found, resulting in a total cloud mass $M(H_2) = 7 \times 10^3$ M_o. An onion skin model of the cloud in which the mass is calculated by summing the mass contribution of each shell, gives the same numbers for the mean density and total mass. These mass estimates may be in error by at least a factor of 2 because of the uncertain geometry of the cloud and possible optical thickness of the ^{13}CO line.

Changes in the emission line profile from point to point can yield information about the kinematics of the gas. At the position of the CO peak, the line profile is at its broadest, having a width of 8 km s^{-1} with the maximum temperature occurring at a velocity of 22.4 km s^{-1}. Away from the peak position, the profiles narrow to a width of 5 km s^{-1}, with the temperature maximum occurring at a velocity of 24 km s^{-1} in many spectra. In the outer envelope of the cloud, the lines

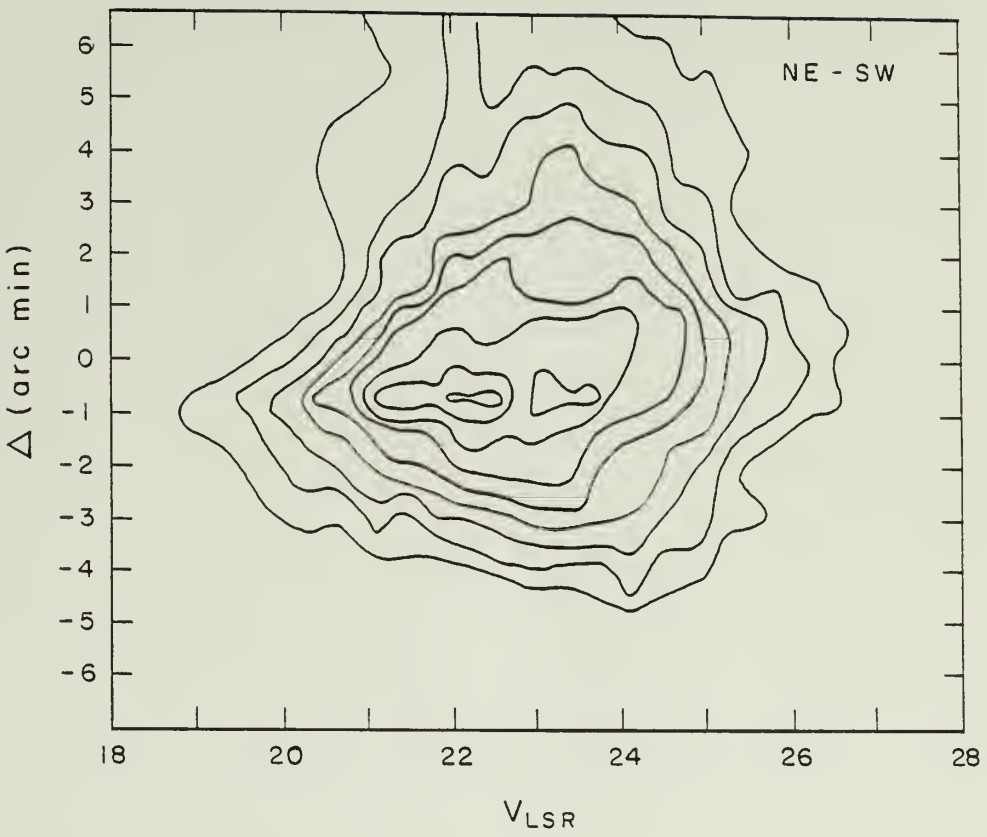

Figure 5

A northeast-southwest strip of ^{12}CO spectra crossing the S87 hot spot at $\Delta\alpha = 0$ illustrating that the hottest and broadest emission is found within one beam of the infrared source, H_2O maser, and brighter compact HII region.

have a width of 2 km s^{-1} centered at V_{LSR} = 22 km s^{-1}. The profile behavior is illustrated in the spatial velocity diagram of Figure 5, constructed from spectra on a NE-SW oriented strip. These line shape changes are also seen in the rarer isotopic species, suggesting that gas motion rather than radiative transfer effects are responsible. The small amplitude and absence of a global pattern preclude interpretation in terms of a simple kinematic model.

2. HCN, CS, and C_2H

The 89 GHz HCN profile in S87 and the 87 GHz C_2H line are shown in Figure 6. The HCN line has a peak temperature T_A = 4.5 °K and shows the hyperfine structure with normal intensity ratios (5:3:1). The C_2H line has a peak temperature of T_A= 0.8 °K in the N = 1-0, F = (3/2,2)-(1/2,0) transition. The cloud core is about 1.5 arcmin in diameter in this molecule, while mapping in the 49 GHz transition of CS gives a core diameter of 2 arcmin.

A quantitative determination of the density in the cloud core can be obtained by applying the large velocity gradient (LVG) radiative transfer calculations of Linke and Goldsmith (1980) to the CS data. Using T_A(J=2-1) = 2.6 °K and T_A(J=1-0) = 2.2 °K (determined from the FCRAO observations) for the CS lines at the (0,0) position, their results computed for T_K= 40 °K give a gas density $n(H_2)$ = 6×10^4 cm^{-3} and a CS fractional abundance X(CS)/(dv/dr) = 1×10^{-10} (km s^{-1} $pc^{-1})^{-1}$. The CS column density is N(CS) = 4×10^{13} cm^{-2} for dv/dr = 1.0 km $s^{-1}pc^{-1}$, near the lower end of column densities found for

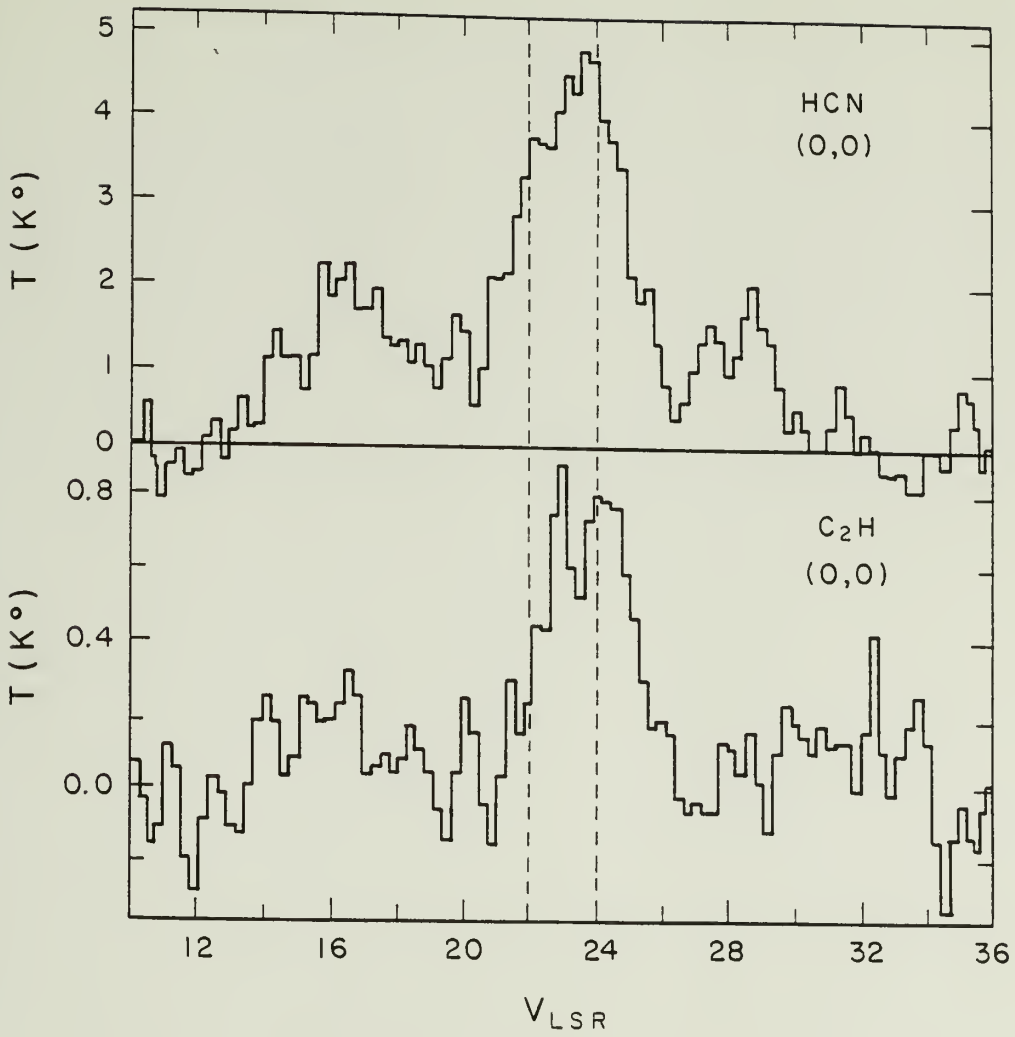

Figure 6

Profiles of HCN and C_2H seen in the direction of the S87 molecular peak.

clouds associated with HII regions studied by Linke and Goldsmith. Since the cloud core is small, beam dilution will affect these estimates, especially since the 49 GHz beam is twice the angular size of the 98 GHz beam. If the intensity distribution of the source is modeled as a 2 arcmin diameter gaussian, degradation of the 98 GHz data to the 2 arcmin beam size of the 49 GHz data decreases $T_A(2-1)$ by about 25 %. This lowers the estimate of the core density by a factor of 4 and increases the fractional abundance of CS by a similar amount. A good estimate for the mean gas density in the inner 2 arcminute core region is $n(H_2) = 1\text{-}2\times10^4$ cm^{-3}, giving a core mass of $M_{core} = 0.5\text{-}1\times10^3$ M_o.

Comparison of the CO profile with those of the high excitation species in the cloud core reveals a shift in the velocity of peak temperature. Whereas the CO profile peaks near 22 km s^{-1}, the high excitation molecules peak at 24 km s^{-1}. Emission of the high excitation molecules at the velocity of peak CO emission is about half the maximum value (see Figure 7 and 1). Apparently the dense gas giving rise to the high excitation spectra is moving away along the line of sight at a velocity of 2 km s^{-1} relative to the center of mass of the lower density CO emitting region.

3. H_2O

The H_2O maser shown in Figure 7 was discovered in April 1979 at the position of the cloud core. Two narrow and well-resolved emission peaks occur at V_{LSR}= 20.5 km s^{-1} and V_{LSR}= 25.1 km s^{-1}, coincident

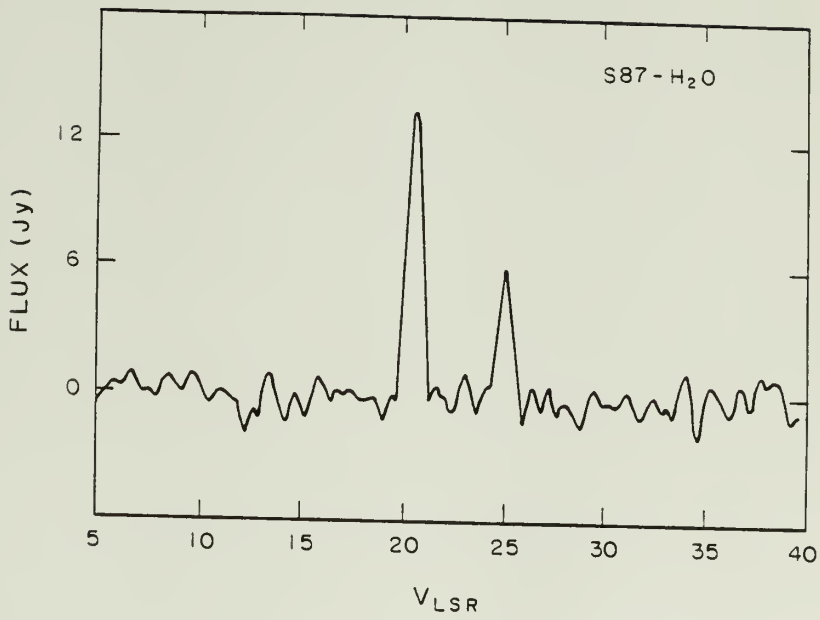

Figure 7

The S87 H_2O maser observed on April 1,1979 with the Haystack Observatory 120 ft antenna. Note that the two peaks coincide with the edges of the CO profile.

with the extreme edges of the CO profile. The highly symmetric placement of the emission peaks about the central velocity of the line profiles suggests a simple model in which the maser emission arises along the line-of-sight through the center of a uniformly expanding (or contracting) gas cloud. The high velocity component forms at the rear (front) of the expanding (contracting) cloud while the low velocity line arises in the front (rear). In general, maser line velocities exhibit a large scatter about the velocity of the cloud in which they are buried (Rodriguez et al. 1979) and the simple pattern seen in S87 may be coincidental.

4. Infrared

Infrared observations were undertaken between 1.8 and 4 microns in order to determine whether the S87 cloud contains imbedded sources that may be protostellar in nature or may contribute significantly to cloud heating. A near-infrared L band search of this region revealed the presence of four sources brighter than 11 th magnitude within a 16'x16' box centered on the (0,0) position. The results of infrared photometry are given in Table 2 and plotted in Figure 8 where the 11 and 20 micron observations from the AFGL catalog have been added. In order to determine the nature of these sources, the J, H, and K magnitudes were used to generate a color-color diagram plotting log(J-H/H-K) against J-K (Snell 1979). This technique allows the intrinsic colors of a star to be separated from the effects of interstellar reddening, thus differentiating between early-type stars,

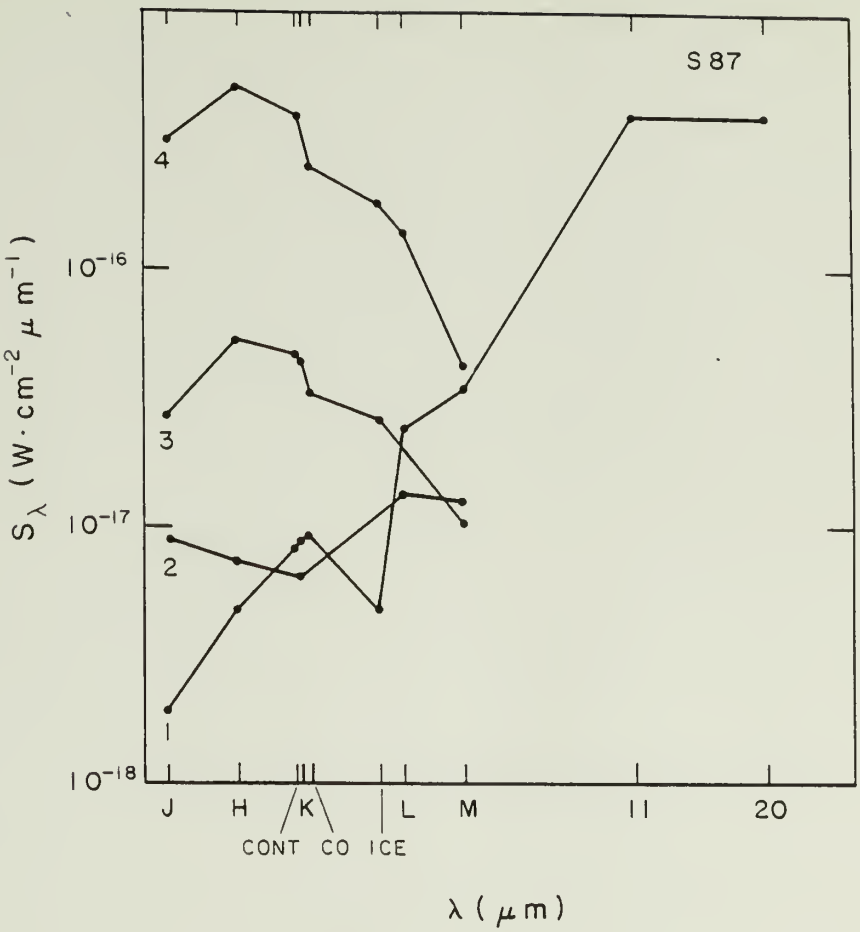

Figure 8

Broadband spectra of the four infrared sources in the vicinity of S87. IRS 1 and IRS 2 are associated with nebulosity and are related to the molecular cloud. IRS 1 coincides with the central compact HII region. IRS 3 and IRS 4 show CO absorption bands at 2.3 microns and are probably background giant stars.

late type stars, and protostars. The results indicate that IRS3 and IRS4 are probably background giant stars that have suffered 15 and 12 magnitudes of visual extinction, respectively.

Sources IRS1 and IRS2 fall in the region of the color-color diagram occupied by protostellar infrared sources such as W3 IRS5, S255 IRS1, and Becklin-Neugebauer object in Orion. IRS1 is intrinsically red, exhibiting a rising spectrum between 1.5 and 5 microns. Assuming that CRL 2454 is the mid-infrared counterpart of IRS1, the spectrum has constant slope up to 11 microns and is flat between 11 and 20 microns. When mapped with a 12" diameter aperture at 3.45 microns, IRS1 has an extended component with a 20"x30" size probably due to heated dust within the HII region. (The free-free flux expected on the basis of the observed radio emission is too feeble to detect.) The Brackett α line was marginally detected in the spectrum of IRS1 with a flux density of $S = 4 \pm 2 \times 10^{-17}$ W $cm^{-2} micron^{-1}$. This implies a 5 GHz flux density of 190 mJy, close to the actual value of 240 mJy. The broadband filter measurements of the infrared spectrum shows a dip at 3.14 microns, the wavelength of the ice feature often seen in absorption against the infrared continuum of buried protostars. Merrill (private communication) has detected the Q branch in the spectrum of H_2 in emission in the direction of S87. The 3.14 micron dip may either be the ice feature or the result of contamination of the L band photometry by Q-branch H_2 emission. The optically visible knot, the stronger radio source, the molecular peak, the H_2O maser, and the infrared source CRL 2454-IRS1 are positionally coincident within the uncertainties of measurement.

TABLE 2

S87 PARAMETERS

Ionized Gas

Source	α (1950)	δ (1950)	Size	Flux Density	ν (GHz)	$\langle n_e \rangle cm^{-3}$	M(HII)	Reference
Envelope	$19^h44^m16^s$	24°28'28"	10'	1.3 Jy	2.7	24	500 M_o	1
1	$19^h44^s13.7^s$	24°27'58"	21"x39"	240 mJy	5.0	900	1.5 M_o	2
2	$19^h44^m15.0^s$	24°28'48"	10"x25"	45 mJy	5.0	1400	< 1.0 M_o	2

Exciting Star - HD 338936 (BOV)

Infrared Sources and Magnitudes

			J	H	K	L	M	A_V
IRS 1	$19^h44^m13.5^s$	24°28'00"	(13.2)	10.9	9.1	6.2	4.7	26
IRS 2	$19^h44^m06.2^s$	25°28'16"	11.5	10.5	9.4	6.9	5.7	15
IRS 3	$19^h44^m11.6^s$	24°25'48"	10.4	8.4	7.3	6.5	5.9	15
IRS 4	$19^h43^m58.4^s$	24°32'10"	7.6	5.9	5.0	4.4	4.4	12

H_2O Maser

$19^h44^m12.4^s$	24°28'06.4"	13 Jy	V_{LSR} = 20.4 and 25.1 km s^{-1}	

(TABLE 2 Continued)

Molecular Peak

	α (1950)	δ (1950)	$T_A(^{12}CO)$	$T_A(^{13}CO)$	$T_A(CS_{1-0})$	$T_A(CS_{2-1})$	$T_A(HCN)$	$T_A(C_2H)$
	$19^h44^m14^s$	24°28'06.4"	32	8	2.2	2.6	4.5	0.8
Cloud Mass		4.4×10^3 M_o						
V_{LSR}		23 km s^{-1}						
Distance		2.0 kpc						

References

1. Felli and Churchwell (1972)
2. Felli and Harten (1980)

The second infrared source, IRS2, exhibits a flat spectrum and coincides with another nebulous star seen on the PSS red plate about 2' west and slightly north of IRS1. No radio emission above 20 mJy has been reported from this object, so it is probably later than spectral type B3. If the flat IR spectrum can be extrapolated through the mid infrared, the total luminosity of IRS2 is small compared to IRS1.

D. S106

The nebula S106 (M1-99,G76.4-0.6) is a prominant bipolar HII region (Calvet and Cohen 1978) 3 arcminutes in length and consisting of two lobes of nebulosity oriented in north-south direction. A visually obscured infrared star (IRS3 of Pihper et al. 1976, and CRL 2585 the AFGL catalog, Price et al. 1976) located midway between the two lobes is probably responsible for the excitation of the nebula. The measured infrared luminosity of this star, is consistent with the excitation of the nebula by an O or B star (Sibille et al. 1975). The literature contains many estimates of the distance to this object based on the rotation law of the galaxy. In the direction of S106 (l = 76°), the rotation curve gives inaccurate distances since all co-rotating points within 6 kpc of the sun exhibit differential doppler shifts of less than 10 km s^{-1} (S106 is at V_{LSR} = -1 km s^{-1}). A recent paper (Eiroa et al. 1979) gives a distance of 500 pc based on infrared photometry. This distance is consistent with the relatively low extinction toward the ionized gas, and will be adopted here.

The biconical distribution of the ionized gas and the presence of a highly obscured central source led Sibille et al. (1975) to suggest the presence of a nearly edge on disk or torus of high density opaque material. Models for an HII region illuminated by a radiation field with bipolar symmetry successfully reproduce the morphology of the ionized gas in S106. The intriguing possibility of observing the disk directly by the emission lines of its molecular constituents led to the present study of this region.

1. The Ionized Gas

The distribution of plasma in S106 is shown by the 5 GHz Westerbork aperture synthesis map published by Israel and Felli (1978). The entire observed radio flux arises in dense gas found in the volume associated with the optical lobes. The highest electron densities are found in the lobe edges near IRS3, the presumed exciting star, where values up to $n_e = 5.9 \times 10^3$ cm^{-3} are seen. The optical emission lines indicate even higher electron densities (Maucherat 1975, Deharveng and Maucherat 1978), with values as high as $n_e = 4 \times 10^4$ cm^{-3} seen in the brighter condenstations. With narrow passband filter photography in Hα, Hβ, [NII], and [OIII], the edges of the southern lobe are limb brightenened, with the most intense emission arising close to the infrared star. The high electron densities and brightening at the periphery of the HII region as predicted by the model of disk constrained HII regions discussed in Chapter IV.

The optical emission line profiles in S106 cover a velocity range of $\Delta V = 70$ km s^{-1}. Gas in the northern lobe emits at $V_{LSR}(H\alpha) =$

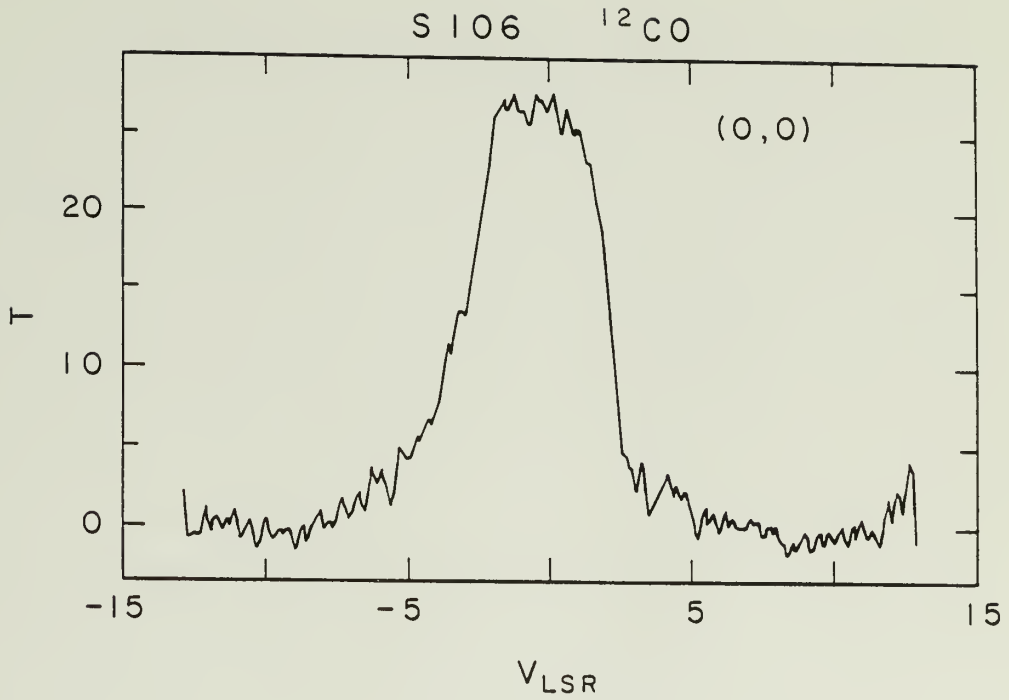

Figure 9

^{12}CO spectrum at the S106 reference position (0,0) corresponding to $\alpha_{1950} = 20^h25^m33^s$ and $\delta_{1950} = 37°12'30''$

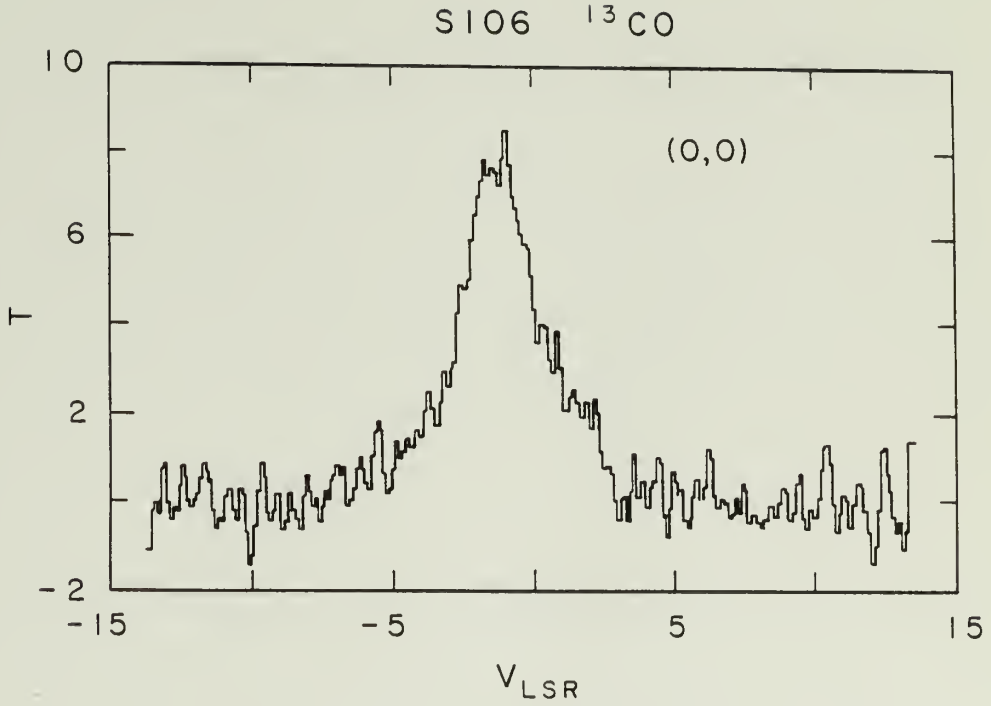

Figure 10

^{13}CO spectrum at the (0,0) position.

20 km s^{-1}, while the southern lobe has components at $V_{LSR}(H\alpha)$ = -45 km s^{-1} and 27 km s^{-1} (Maucherat 1975). The red-shift of the line centroid in the north and the increased extinction there suggest that the axis of symmetry of the biconical nebula is tilted away from the observer in this direction.

2. CO

A molecular cloud associated with S106 has been detected by Cong (1977) and mapped with the Texas antenna by Lucas et al. (1978) in the CO transition. The distribution of ammonia was mapped by Little et al. (1979). These observations suggest an overall velocity gradient in the East-West direction, consistent with rotation around an axis aligned with the biconical nebula. Water vapor maser emission was discovered by Cesarsky et al. (1978) and Blair et al. (1978) from a point about 2 arcminutes west of the infrared star, well outside the HII region. Variability in the maser is indicated by the difference in the velocity of the lines detected by these two sets of investigators on different observing dates (-1.1 km s^{-1} vs. -4.0 km s^{-1}).

The ^{12}CO and ^{13}CO profiles observed at the cloud center are shown in Figure 9 and 10. The CO line has a peak temperature of 26 °K at V_{LSR} = -1 km s^{-1} with a half-power width of 6 km s^{-1} and faint wings traceable over a 20 km s^{-1} range. Maps of the S106 cloud are shown in both isotopic species in Figures 11 to 15. Considerably more structure is evident in this data than was visible in previously published maps. Three distinct peaks are present in the maps. Peaks

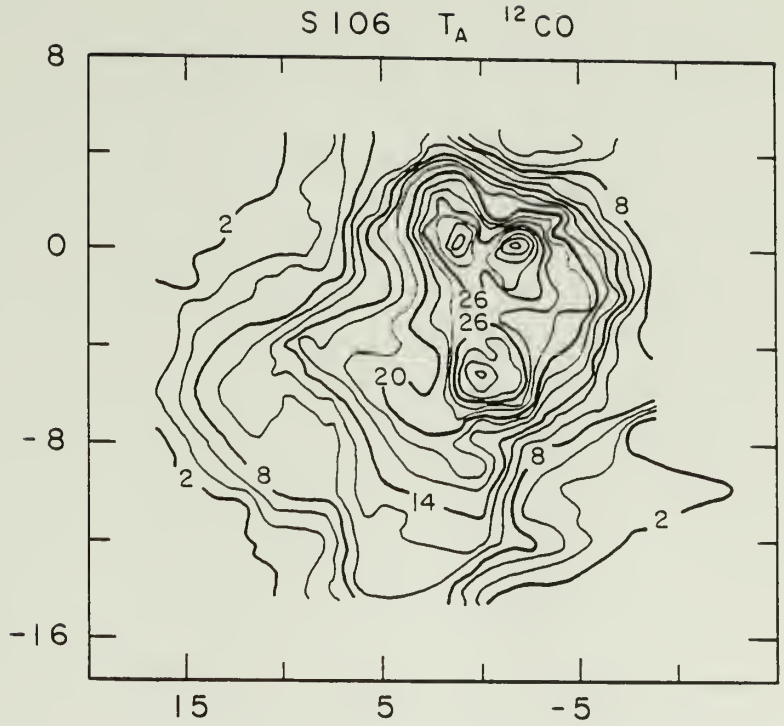

Figure 11

^{12}CO map showing the entire cloud. Peaks A and B are the hot spots close to the reference position above center while peak C is close to the center of the figure.

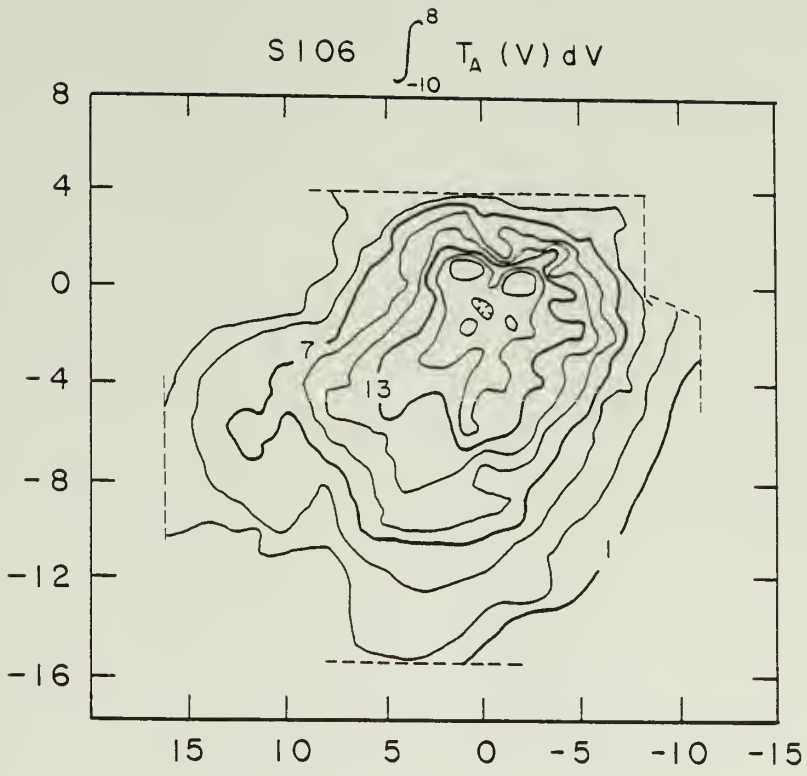

Figure 12

^{12}CO map of $\int_{-10}^{8} T_A(v)dv$, the integated line profile. Contour labels are this quantity divided by 10. Contours are chosen at 1, 4, 7, 10, 13, 17, 20, 23.

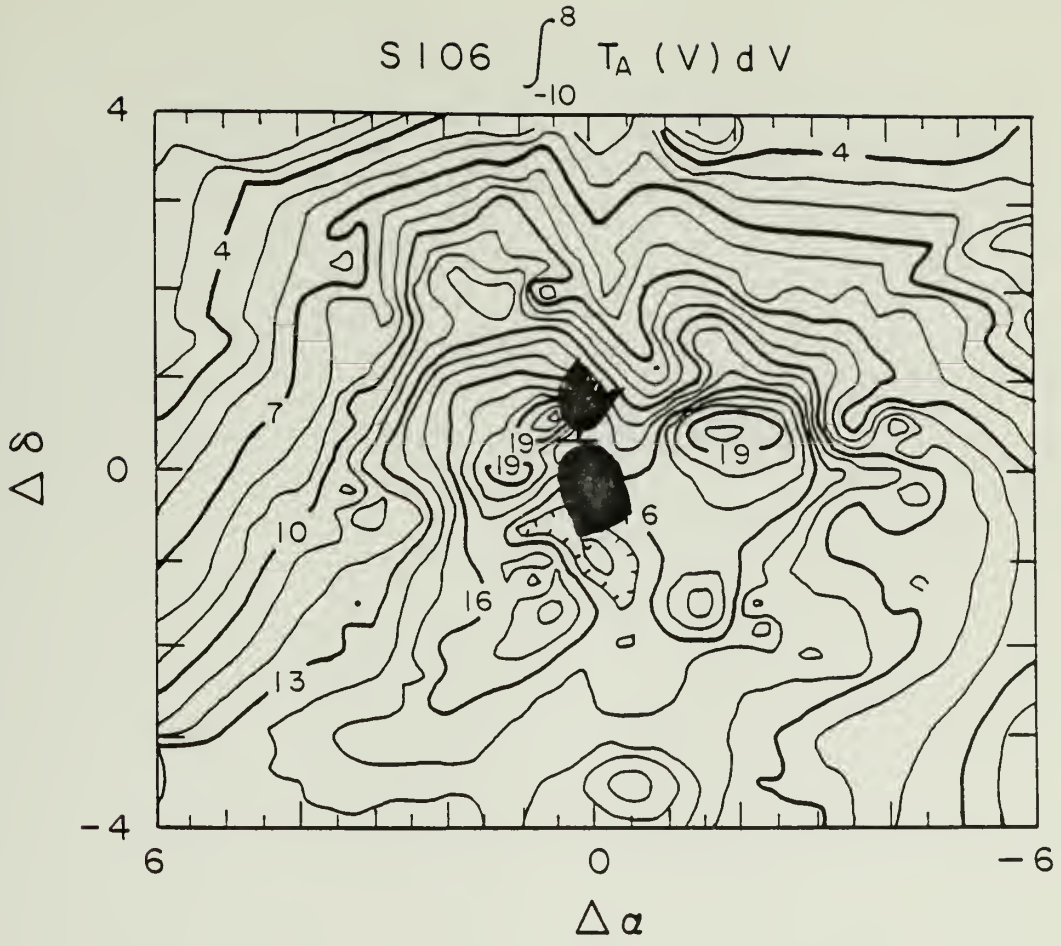

Figure 13

Map of ^{12}CO emission around S106 with the HII region superimposed. The central infrared source (exciting star) is located between the two black lobes and is marked by a black cross. The solid black marks the approximate extent of the nebula as seen on the PSS red plate. Conturs represent the integrated line profile as indicated at the top of the figure but divided by 10.

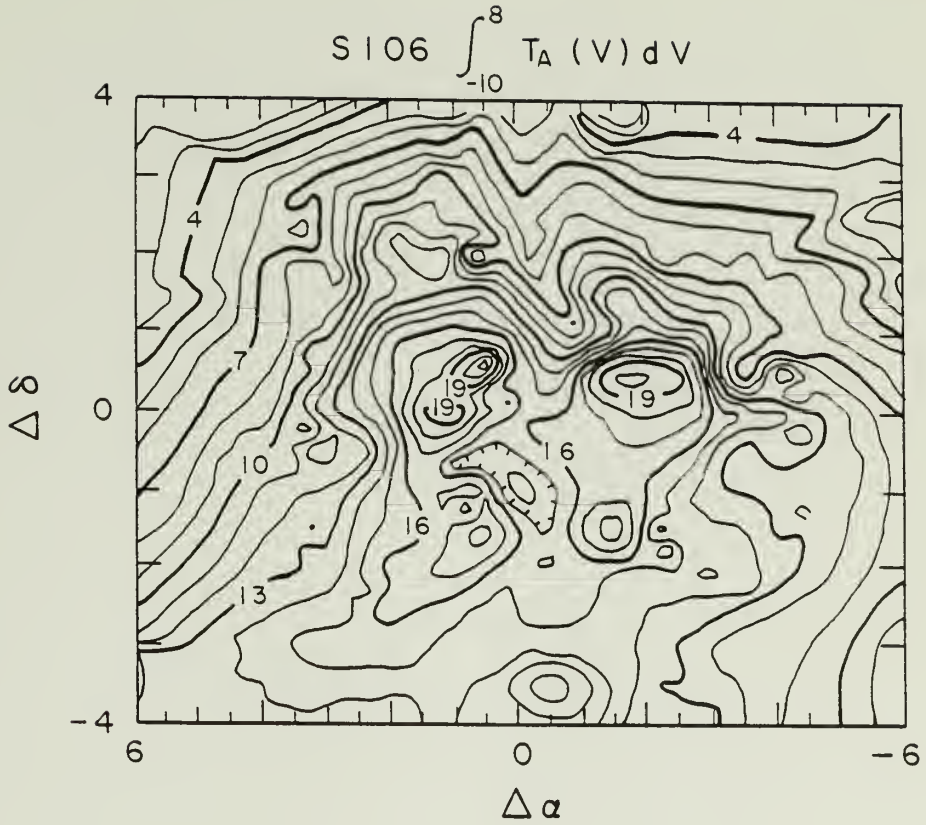

Figure 14

A ^{12}CO map of the inner region showing the disk. The (0,0) coordinates correspond to $\alpha_{1950} = 20^h25^m33^s$ $\delta_{1950} = 37°12'30"$ Contour units give the integral under the line profile in units of 10 °K km s^{-1}.

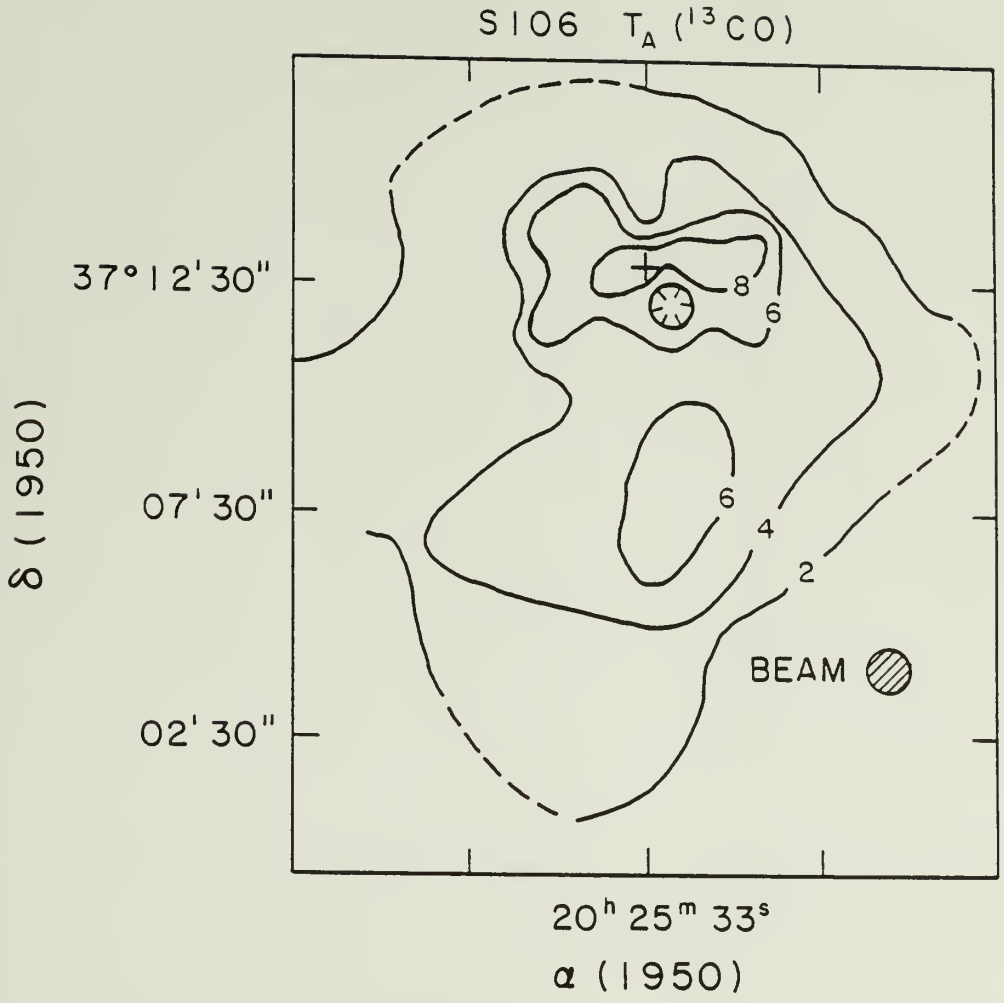

Figure 15

^{13}CO map of S106 with the position of the infrared source marked by a (+) symbol.

A and B appear 1 arcmin east and 2 arcmin west of the central infrared star. These two peaks surround the HII region in the spatial velocity diagram shown in Figure 16. The distribution of ionized gas is anti-correlated with the CO peak intensity and with the value of the integrated line profiles as shown in the high resolution map of the core region (Figure 14). While the ionized gas extends only an arcminute to the north and south of the central star, the CO hole extends over many arcminutes. Molecules situated just outside the ionization fronts may have been dissociated by UV photons with wavelengths longer than the Lyman edge.

A third CO peak, C, lies about 5 arcminutes south of the infrared star and is shown in the north-south spatial velocity map of figure 17. In the vicinity of peak C, the ^{12}CO profile is double peaked with the line inversion being traceable over several arc minutes of the position (-0.5',-4.5'). Both ^{12}CO and ^{13}CO have their peak temperatures at V_{LSR}= -1.0 km s^{-1} and the ^{13}CO line exhibits a plateau at the velocity of the secondary ^{12}CO peak (Figure 18). More observations are required to determine whether the inversion is caused by absorption by cold foreground gas or by the presence of a second velocity component giving rise to the secondary feature.

Although evidence for cloud rotation has been been reported on the basis of earlier CO data (Lucas et al. 1978), there is no clearcut overall velocity gradient in the data presented here. Apparent gradients in Lucas et al.'s data could have been produced by the super-

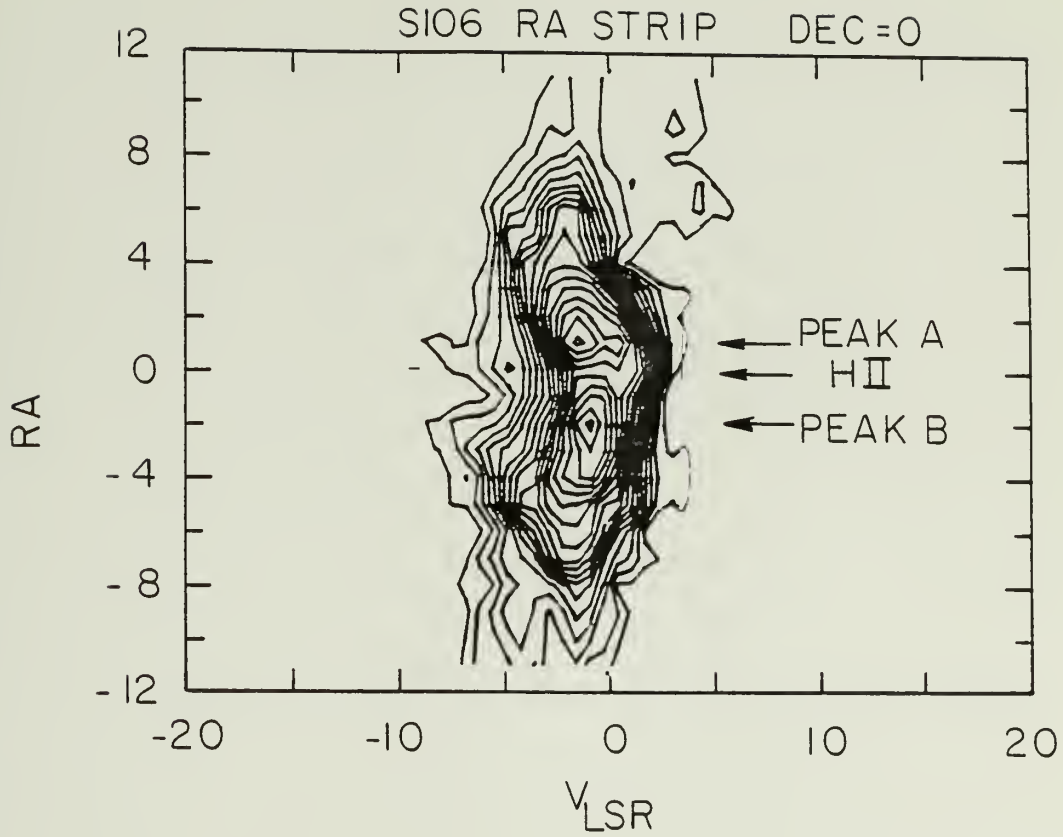

Figure 16

An east-west spatial-velocity diagram running through the center of S106 at the reference Declination of $\Delta\delta = 0$. Peaks A and B as well as the position of the HII region are marked.

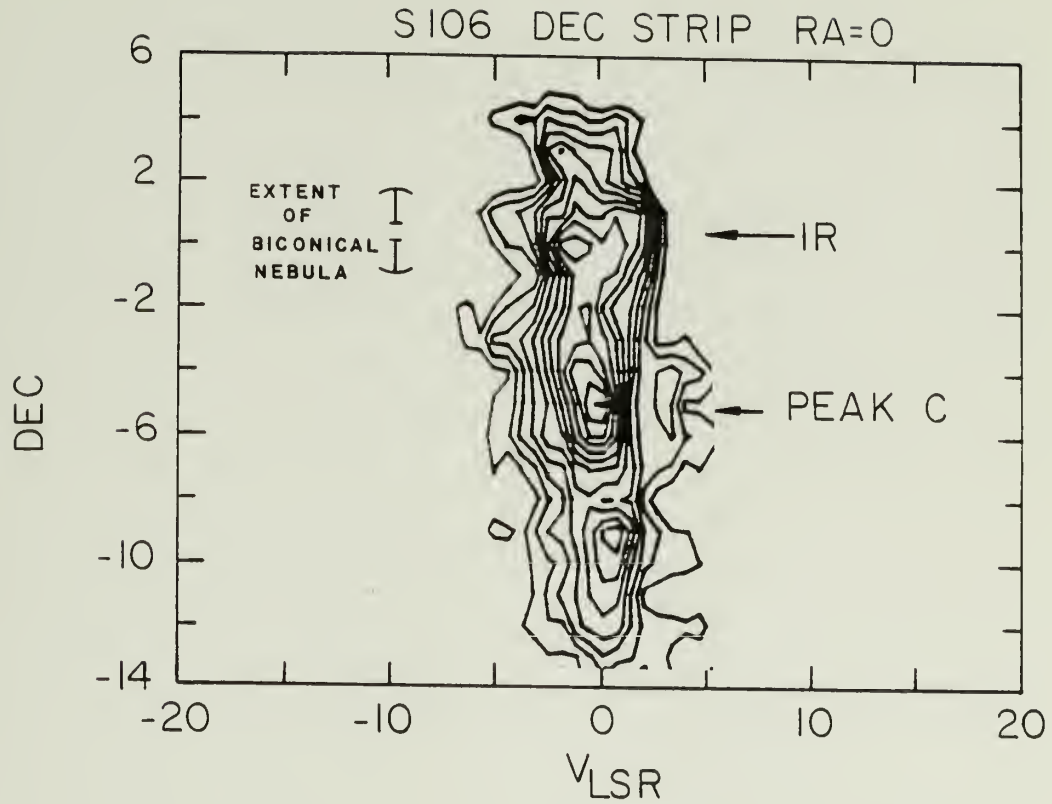

Figure 17

A north-south spatial-velocity diagram of S106 showing peak C and the position of the biconical HII region.

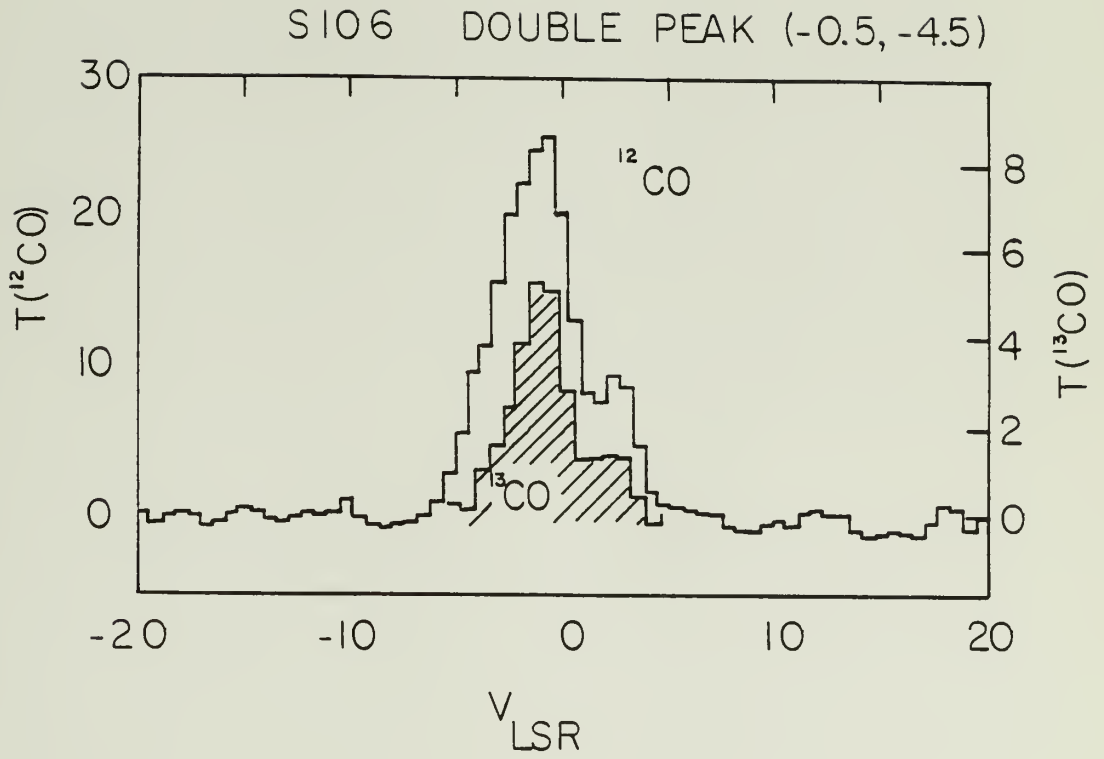

Figure 18

CO spectra near peak C showing two isotopes. Spectra taken within 2' of this position show a double peak in ^{12}CO.

position of foreground or background emission in the southeast part of the cloud. While most of the CO in S106 emits near V_{LSR}= -1.0 km s^{-1} , a component at V_{LSR}= -3.0 km s^{-1} is seen 9 arcmin southeast of the (0,0) position. A little farther in the same direction, the profiles jump to V_{LSR}= 2.0 km s^{-1}. Since these velocity components appear abruptly at locations where there are no obvious sources of kinetic energy (such as HII regions), they probably represent discrete clouds rather than velocity shifts within the S106 cloud. Localized velocity gradients are seen in some portions of the cloud such as in the region immediately surrounding the HII region and in some north-south running spatial velocity diagrams near $\Delta\alpha$ = 5' (where the gradient always amounts to less than 0.05 km s^{-1}arcmin^{-1}). Spatial velocity diagrams such as the one shown in Figure 16 show that the large scale velocity structure is best characterized as chaotic.

The mass of the S106 cloud is estimated from the CO maps using the formula

$$M = 3.3 \left(\frac{\Delta\alpha}{\text{arcmin}}\right)\left(\frac{\Delta\delta}{\text{arcmin}}\right)\left(\frac{N(H_2)}{10^{22}\ \text{cm}^{-2}}\right)\left(\frac{D}{500\ \text{pc}}\right)^2 \quad M_o$$

The cloud is separated into three regions:

(1) The central bar where $T_A(^{13}CO) > 8$ °K which shows up as a 6'x 2.5' structure elongated in the east-west direction in the ^{13}CO maps. The average molecular hydrogen column density is $N(H_2)$ =

4×10^{22} cm^{-2} resulting in a mass estimate of 200 M_o for this component if all the gas along the line of sight is contained within it.

(2) The second region is characterized by $T_A(^{12}CO) \geq 15$ °K and $T_A(^{13}CO) \geq 4$ °K and has an equivalent area of 8'x8'. This is the portion of the cloud exhibiting enhanced ^{12}CO temperatures and is probably influenced by the HII region or luminous sources associated with it. A mean column density $N(H_2) = 2 \times 10^{22}$ cm^{-2} when used in the above formula gives a mass of 320 M_o for this component, not including the contribution of the dense core region 1).

(3) The third region is a halo which is characterized by cold cloud temperatures of $T_A(^{12}CO) \leq 10$ °K and subtends an equivalent area of 16'x16'. From the weak ^{13}CO lines ($\simeq 2$ °K), a typical column density $N(H_2) = 5 \times 10^{21}$ cm^{-2} yields a mass of 320 M_o.

The total mass of the entire cloud can be estimated by summing the contributions of each component, giving M = 840 M_o. Assuming that this mass fills a cubic volume 2.3 pc on a side (corresponding to 16'x16' at d = 500 pc), a mean density $n(H_2) = 1.4 \times 10^3$ cm^{-3} results. The molecular cloud associated with S106 is a relatively low mass object.

3. CS

Mapping of the J = 1-0 transition of CS shows that the dense core region of the molecular cloud includes both peaks A and B seen in the CO map. The CS emitting gas surrounds the HII region and is

elongated in an east-west direction just like the bar feature visible in ^{13}CO. Like the CO maps, CS exhibits two peaks coincident with CO peaks A and B and a minimum in both peak line temperature and width at the position of the nebula. A small east-west velocity gradient amounting to $\Delta V = 0.1$ km s^{-1} $arcmin^{-1}$ is seen between the two peaks with the red shift occuring in the west. This is consistent with the sense of rotation detected by Little et al. (1979).

4. Interpretation of the Bar : Evidence for a Massive Molecular Disk Surrounding S106

Evidence for a disk can be found in the millimeter data in two forms: 1) the elongated, east-west oriented ridge of high column density, hot gas seen in CO, CS, and NH_3 that nearly bisects the two lobes of the biconical nebula; 2) the velocity gradient which possibly indicates rotation around an axis coincident with the axis of symmetry of the nebula.

The total mass of the disk is less than the estimate made for the bar feature above since not all gas in the line-of-sight lies in the disk. An estimate of the contribution to the column density of foreground and background gas can be made by assuming that it is the same as the column density of the 8'x8' component, e.g. 2×10^{22} cm^{-2}. Thus, about half of the column density in the direction of the disk is due to gas within the disk. A crude estimate of the disk mass is then $M_{disk} = 100\ M_o$ for an angular size 2.5'x6'. If the gas were distributed uniformly in a pancake of height h and radius r_d, the mean particle density is

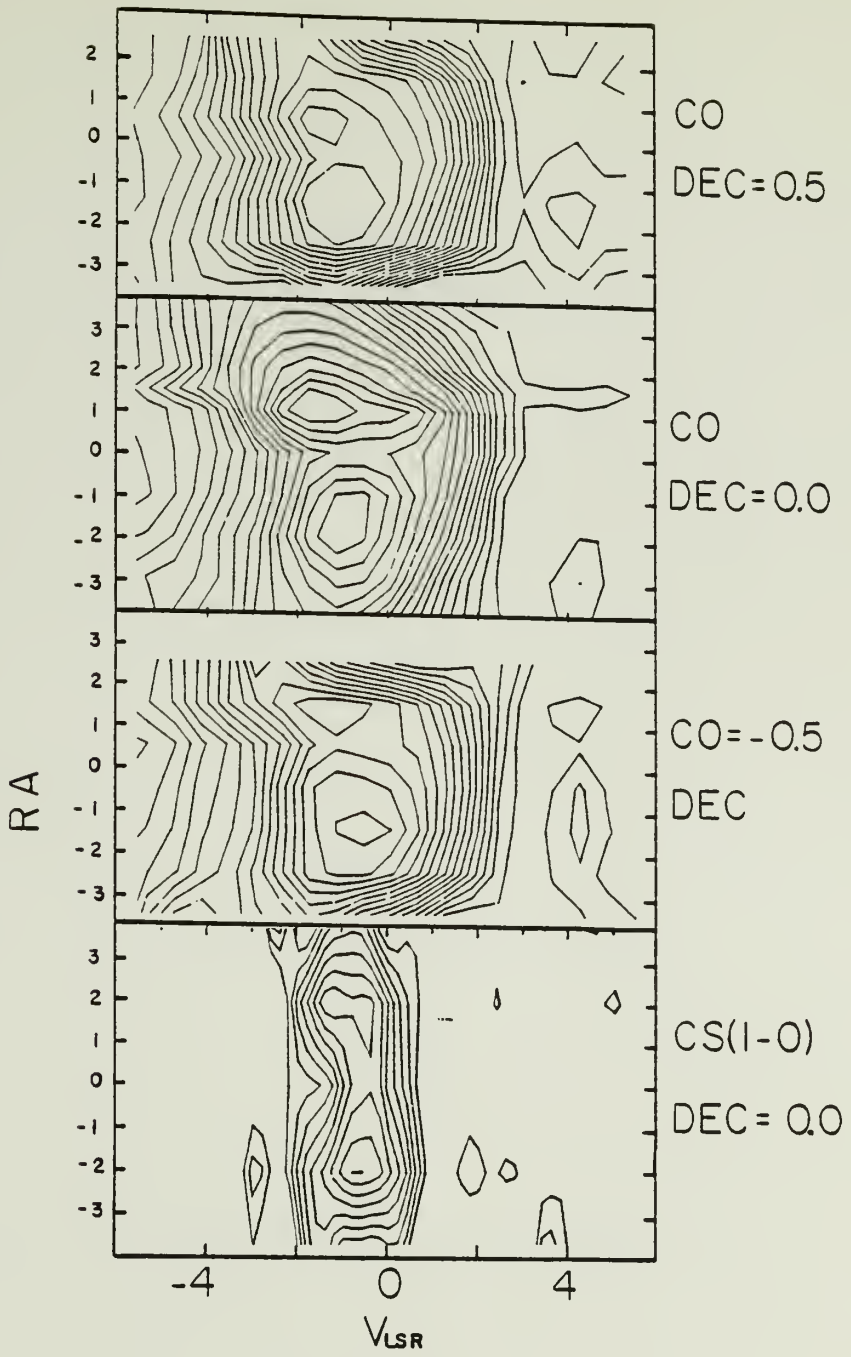

Figure 19

S106 showing the kinematics of the core region. The upper three figures show ^{12}CO strips running in the east west direction and separated by 30" in declination. Contours are at intervals of 2°K. The lowest box shows a CS(1-0) SV strip at $\Delta\delta = 0$ with contours at 1°K intervals. The HII region is nested between the two peaks.

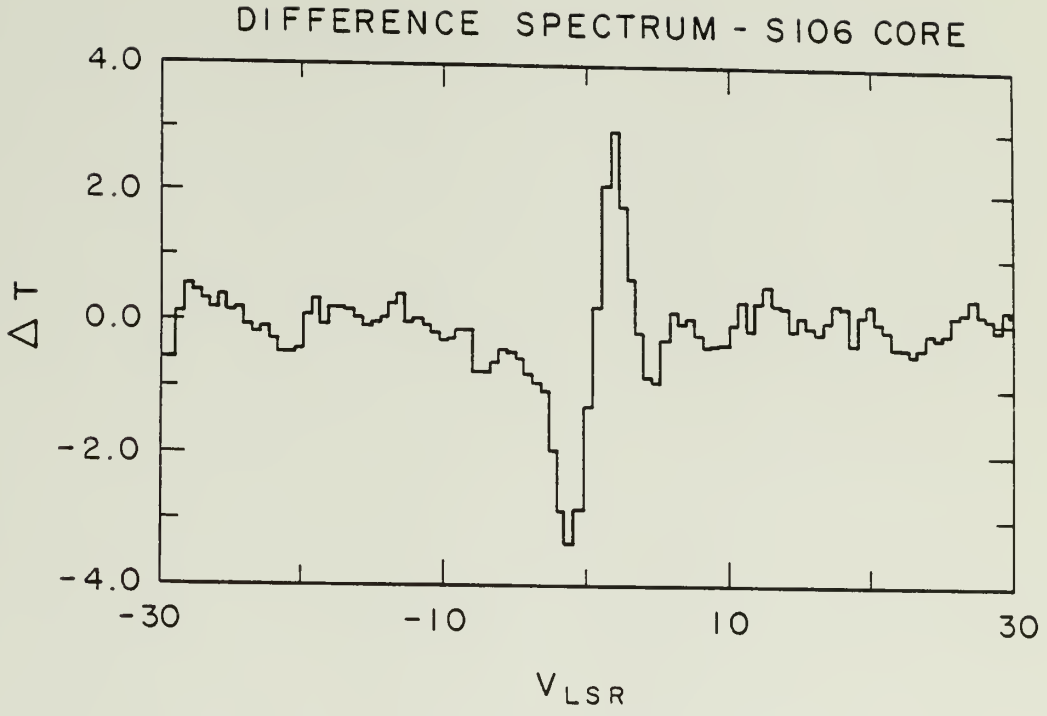

Figure 20

S106 core kinematics. All spectra within two arcmin box of peak A and peak B were averaged. The two average spectra were subtracted to illustrate the shift in the velocity of the emission comming from each peak.

TABLE 3

S106 PARAMETERS

Ionized Gas

	α (1950)	δ (1950)	Size	S_ν	ν (GHz)	$\langle n_e \rangle$ (cm^{-3})	M(HII)	Ref.
Envelope	$20^h25^m35^s$	37°12'30"	30"x140"	6.2 Jy	5.0	1800	0.2 M_o	1
A (S lobe)	$20^h25^m32.8^s$	37°12'48.5"	8"x8"	0.8 Jy	5.0	16000	10^{-3} M_o	1
B (S lobe)	$20^h25^m34.2^s$	37°12'45.9"	8"x28"	?	5.0	?	?	1
c (N lobe)	$20^h25^m34.5^s$	37°13'07.8"	18"x12"	1.3 Jy	5.0	8000	10^{-2} M_o	1
Exciting Star - IRS #3		Spectral type B0V - O8V ($L \sim 10^4 L_o$)						
	$20^h25^m33.7^s$	37°12'50"						2,3
H_2O Maser	$20^h25^m25.0^s$	37°12'30"	V_{LSR} = -1.1 and -4.0 km s^{-1}					4,5

Molecular Peaks

East Peak	$20^h25^m38^s$	37°12'40"	27°K
West Peak	$20^h25^m27^s$	37°12'50"	30°K
South Peak	$20^h25^m33^s$	37°08'30"	27°K
Cloud Mass = 840 M_o	V_{LSR} = -1.0 km s^{-1}	Distance = 500 pc	3

References:

1. Israel and Felli (1978)
2. Pipher et al. (1976)
3. Eiroa et al. (1979)
4. Cesarsky et al. (1978)
5. Blair et al. (1978)

$$n_d = M_{disk} / 2 \pi m_H r_d^2 h$$

$$= 10^4 (r_d /0.45 \text{ pc})^{-2} (h /0.3 \text{ pc})^{-1} (N /2x10^{22}) \text{ cm}^{-3}$$

This is approximately the density required to excite CS.

One way of supporting a disk is by rotation. Although little evidence exists for rotation of the entire cloud, a velocity gradient is seen in the cloud core in CO as well as in the observed high excitation molecules. Figure 19 shows spatial-velocity diagrams in the east-west direction in CO obtained with a 30" beam spacing as well as a similar diagram in CS. The reality of the velocity gradient is demonstrated by averaging all spectra within 2' of peak A and doing the same for all spectra within 2' of peak B. Subtraction of the two synthetic spectra shows an S shaped spectrum, illustrating that a difference of 2.0 km s^{-1} exists in the mean velocities of the gas associated with each peak. (Figure 20).

E. S117

The ^{12}CO line was used to map out the velocity field in the molecular gas associated with the North America and Pelican Nebulae in Cygnus. The observations indicate the presence of an expanding network of molecular filaments and clumps forming a roughly hemispherical shell of dense gas. This shell is probably the remnant of an expanding ionization/shock front system driven by the expansion of the HII region W80. The eventual bursting of the HII region into

the intercloud medium and the acceleration of the swept-up shell by the rocket effect once the shock wave has reached the parent cloud boundary has led to the currently observed large velocity of the H_2 gas.

The Pelican Nebula

The North American and Pelican Nebulae (W80, DR27, NGC7000, IC5070,S117) are part of a large HII region cloud complex located on the northeastern corner of the Cygnus X region. Radio continuum observations of the ionized gas (Wendeker 1968, Goudis 1976a, b) indicate the presence of one large HII region; the North American Nebula in the east and the Pelican in the west appear distinct in photographs because of the presence of foreground obscuration (Figure 21).

Molecular gas is plentiful in this part of the sky. Observations of CO have been reported by Penzias et al.(1972) and Milman et al. (1975a, b), who found complicated line shapes in the dust separating NGC7000 from IC5070. Cong (1976) mapped the Cygnus X region in ^{12}CO but did not include the W80 complex. His map, however, shows a molecular cloud at V_{LSR}= 0 - 2 km s^{-1} just to the southwest of W80. The velocity of this cloud is virtually identical to both the radio recombination line velocities of the HII region (Goudis 1976a,b) and the mean velocity of the expanding CO feature reported here. It is likely that this cloud is the southern extension of the parent cloud out of which the W80 complex formed.

The distance to this complex is difficult to determine accurately. Various lines of reasoning have placed the distance between 420 pc (Beer 1964) and 1980 pc (Dieter 1967). Most workers have found the value adopted here of around 1 kpc (Wendeker 1968, Downes and Rinehart 1965, Goudis 1967a), implying a diameter of 50 pc for the ionized region. This value coupled with the relatively low electron density of $n_e = 9\ cm^{-3}$ (Wendeker 1968) suggests a rather old and evolved HII region molecular cloud complex. The mass of ionized gas contained within the nebula is $M_{HII} = 1.8 \times 10^4\ M_o$.

The source of excitation of the W80 HII region has not been conclusively identified. Although the O6 star HD 199579 is capable of ionizing a sphere 50 pc in diameter at the density $n_e = 9\ cm^{-3}$, this star is not located near the geometric center of the nebula or near the peak of the radio continuum emission. Several very bright ionization fronts lie over 25 pc from this star. It is quite likely that other luminous early-type stars lie within the nebula, obscured by the foreground dust lane. We searched the central region of the W80 complex in the near-infrared for such stars. Several bright IR sources, most notably nos. 8, 9, and 10 in Table 6 have J-H and H-K color indices that indicate early spectral type as determined by plotting log(J-H/H-K) against J-K (Snell 1979). Application of the interstellar extinction curve of Becklin et al. (1978) to the color indices implies that the brightest source, IRS8, suffers 14 magnitudes of visual extinction and its dereddened magnitude is constant at a value of m = 3 mag between the J and M bands. At a distance of 1 kpc

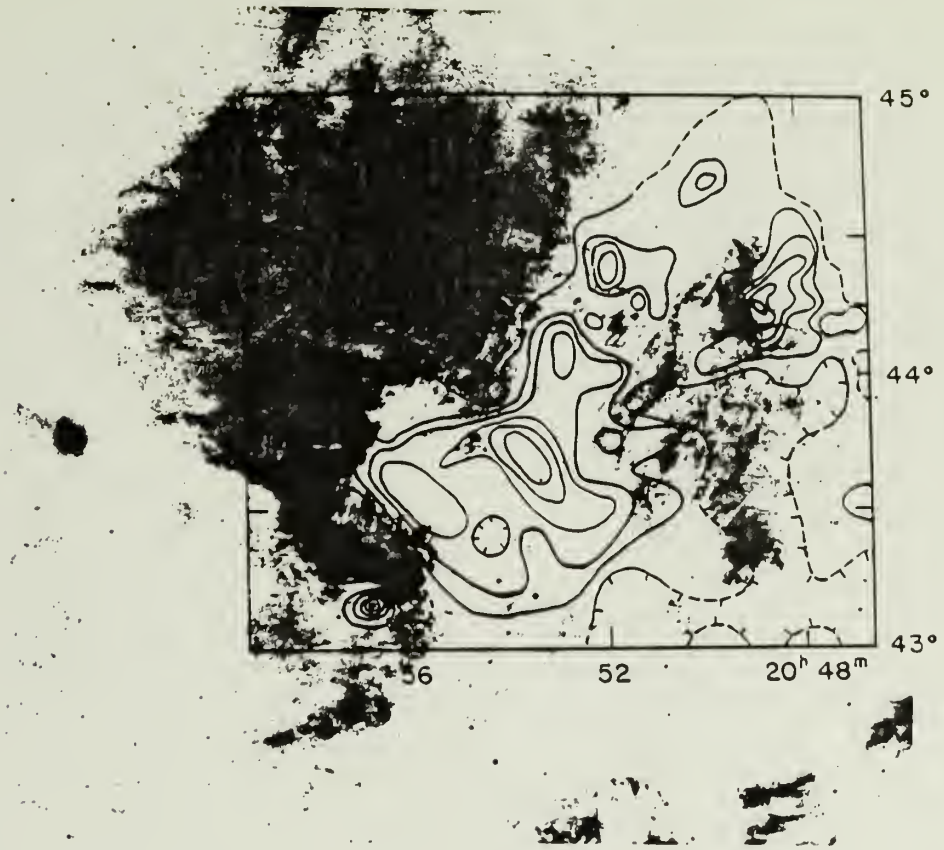

Figure 21

Contours of integrated ^{12}CO line intensity, $\int_{-10}^{10} T_A(v)dv$ plotted on the red Palomar Sky Survey (PSS) plate showing the W80 complex. Contours are drawn at intervals of 20 °K km s^{-1}. The Pelican Nebula (IC5070) is on the right and the North America Nebula (NGC7000) is on the left.

Figure 22

Schematic diagram of W80 showing the outline of the optical emission (shading), the distribution of radio emission (contours), location of spatial-velocity diagrams shown in the other figures (straight lines), and the location of various reference positions. The radio contours are after Wendeker (1968). The rectangular box corresponds to the boundary of the CO map shown in Figure 21. Letter labels indicate the following:

a) Strip corresponding to the spatial-velocity (SV) diagram shown in Figure 28.
b) SV strip shown in Figure 26.
c) SV strip shown in Figure 25.
d) SV strip shown in Figure 27.
e) Center of expansion of the molecular shell.
f) The reference position from which the offsets $\Delta\alpha$ and $\Delta\delta$ are measured, corresponding to $\alpha_{1950} = 20^h48^m00^s$ and $\delta_{1950} = 44°30'00''$.
g) Position corresponding to the spectrum shown in Figure 24, the Pelican hot spot.
h) Position corresponding to Figure 23.

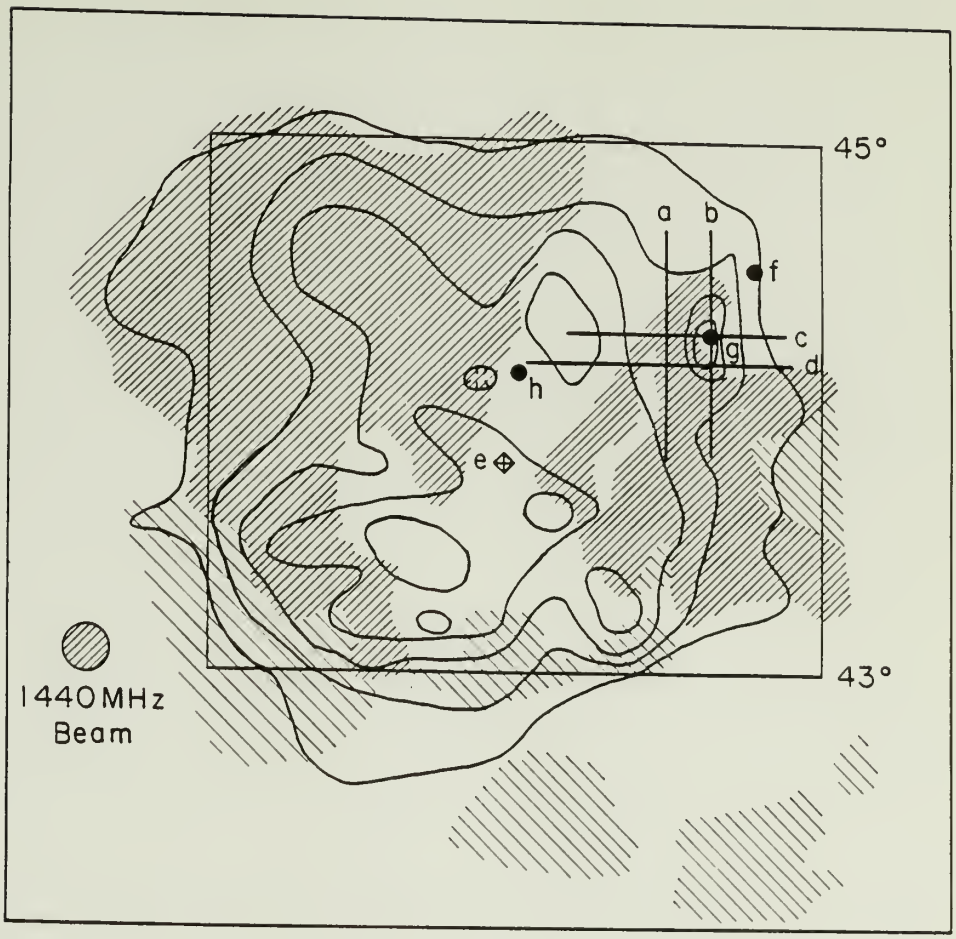
45°
43°
a
b
c
d
e
f
g
h
1440MHz
Beam

this star is of absolute magnitude M_K = -7, which corresponds to spectral type O or B on the main sequence. Although IR photometry is not accurate in determining the spectral type, the coincidence of some of these stars with the radio f-f peak suggests that they may contribute to the excitation of W80.

Much low mass star formation has also occurred in the clouds associated with the W80 complex. Emission line stars, LkHα 131 through 195, are found here (Herbig 1958, Welin 1973, Herbig and Kuhi 1963) in addition to numerous T-Tauri stars. A high concentration of emission line stars occurs near the ionization front in the Pelican. Spectroscopic observation of the nonemission line objects here show none to be earlier than spectral type A6.

In this section, extensive CO observations of the neutral gas associated with the W80 complex are reported. Coarsely spaced data serve to map the large-scale structure and kinematics; high spatial resolution observations delineate the microstructure in the vicinity of ionization fronts and several cloud core regions. Following presentation and discussion of the data, a theoretical model for the evolution of HII regions and their dynamic interaction with molecular clouds is given in Chapter IV.

2. CO Distribution

CO spectra of two characteristic positions in the nebula are shown in Figures 23 and 24. The first of these is taken in the direc-

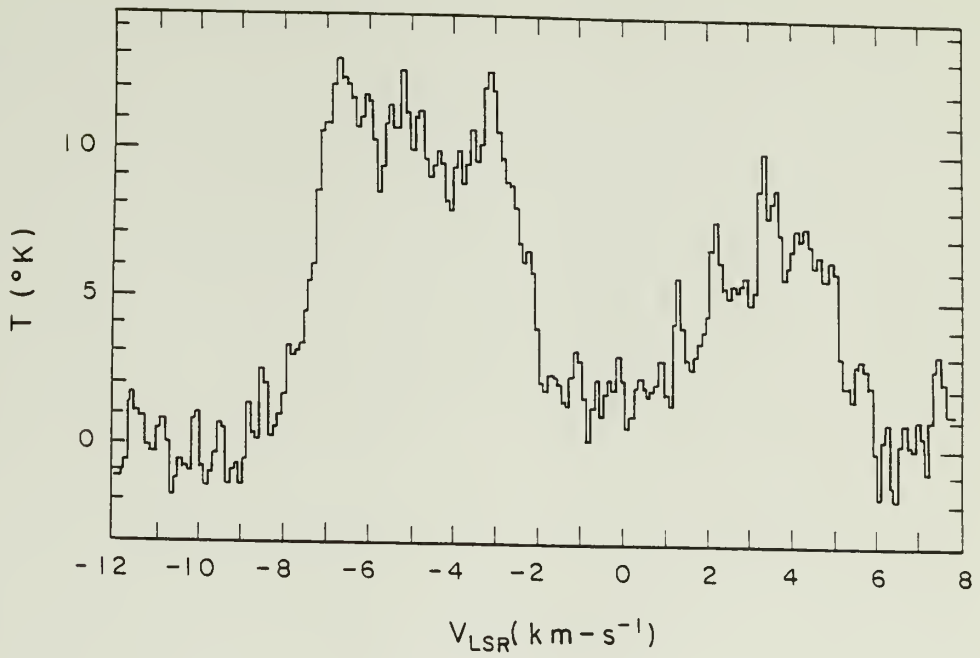

Figure 23

A ^{12}CO spectrum at $\alpha_{1950} = 20^h53^m00^s$, $\delta_{1950} = 44°08'00''$ in the direction of the dust lane separating the Pelican from the North American Nebula. Position denoted as "h" in Figure 22.

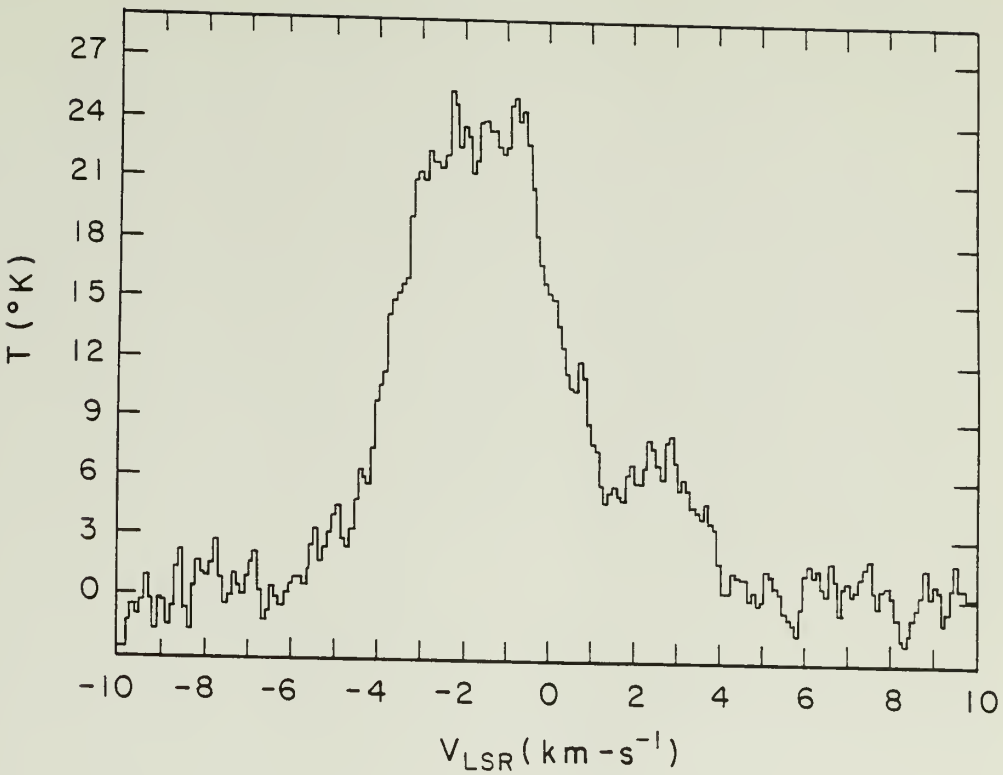

Figure 24

The hot spot in the Pelican at $\alpha_{1950} = 20^h48^m50^s$, $\delta_{1950} = 44°15'00"$. This position corresponds to a bulge of material protruding into the HII region (letter "g" in Figure 22).

tion of the dark dust lane crossing between the North American and the Pelican nebulae; the second was obtained near the CO hot spot located along the western edge of the Pelican nebula. The remarkable characteristic of the data from this area is the large radial velocity shifts encountered as one crosses the nebula. The spectral lines in some locations show structure over a 20 km s^{-1} range between V_{LSR} = -10 to 10 km s^{-1}. In the discussion below, it is pointed out that these observed velocity shifts are well correlated with the optical morphology of the HII region. The overall distribution of CO emission is displayed in figure 21. Here contours of the integrated intensity between -10 and 10 km s^{-1} are overlayed on the Palomar Sky Survey print. In the southern half of the cloud, data has been taken at very coarse intervals (5' to 10' spacing) since the goal was only to outline the boundary of the cloud; in the border area of the Pelican, data was taken down to 1 arcminute spacing as deemed necessary.

Generally there exists a strong correlation between the integrated CO emission and the dark dust lanes crossing in the foreground of the HII region and the dust areas ringing the western and southern periphery of the optical emission. The CO is less prevalent to the east in the area of the North American Nebula. Due south of the Pelican Nebula only weak mm-emission is detected. In the northern Pelican the emission is moderately strong. Most of the CO seen in the direction of the optical emission presumably arises from molecules on the back side of the HII region, since the extinction

lying in front of the visible Hα is estimated to be less than a few magnitudes. The overall morphology of the region is that of a giant molecular cloud with W80 situated on the northern extremity. Parts of the W80 HII region are still enclosed by molecular gas, since in the vicinity of the Pelican we see both foreground and background CO. In other areas where one can see Hα emission, it is clear that W80 has burst the molecular cloud on at least one side.

3. Molecular Gas Kinematics

The large-scale velocity field near the Pelican can be characterized by the following general properties: (1) Near the periphery of the HII region, the CO line is at V_{LSR}= -2 to +2 km s^{-1}. (2) As spectra closer and closer to the radio center of the W80 HII region are considered, line splitting with increasing peak separation is seen. Near the HII region center, the line splitting has a magnitude of about ΔV = 10 km s^{-1}. (3) The negative velocity component of these split lines is correlated with the dust lane crossing in front of the HII region. Similarily, the positive velocity component is often seen in areas where the Hα emission is strong, such as the head of the Pelican and hence these molecules lie behind the HII region.

The above characteristics are seen most clearly in spatial-velocity diagrams using data from strips crossing the face of the HII region. These diagrams show dramatic variations on both large and small scales, consisting of hot spots, smooth and abrupt velocity shifts, and line splitting. One such strip running east-west at the

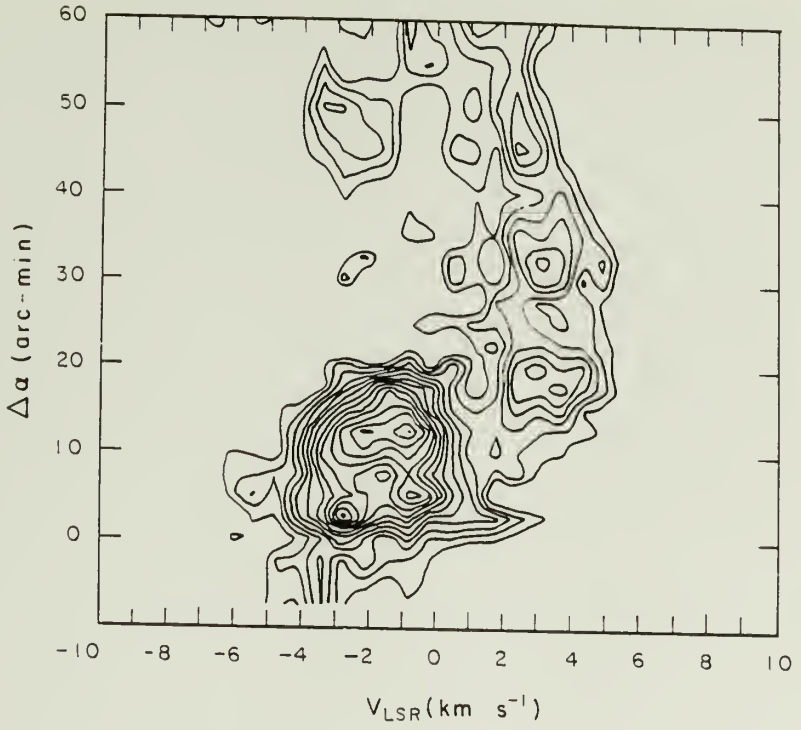

Figure 25

An SV diagram taken in the East-West direction through the Pelican hot spot. As the HII region boundary is crossed at $\Delta\alpha = 20'$, the negative velocity emission disappears, being replaced by gas emitting at $V_{LSR} \sim 3$ km s^{-1}. Offsets in R.A. are measured in equatorial arcminutes ($1' = 4^s$ of R.A.). This strip is at $\Delta\delta = -15'$.

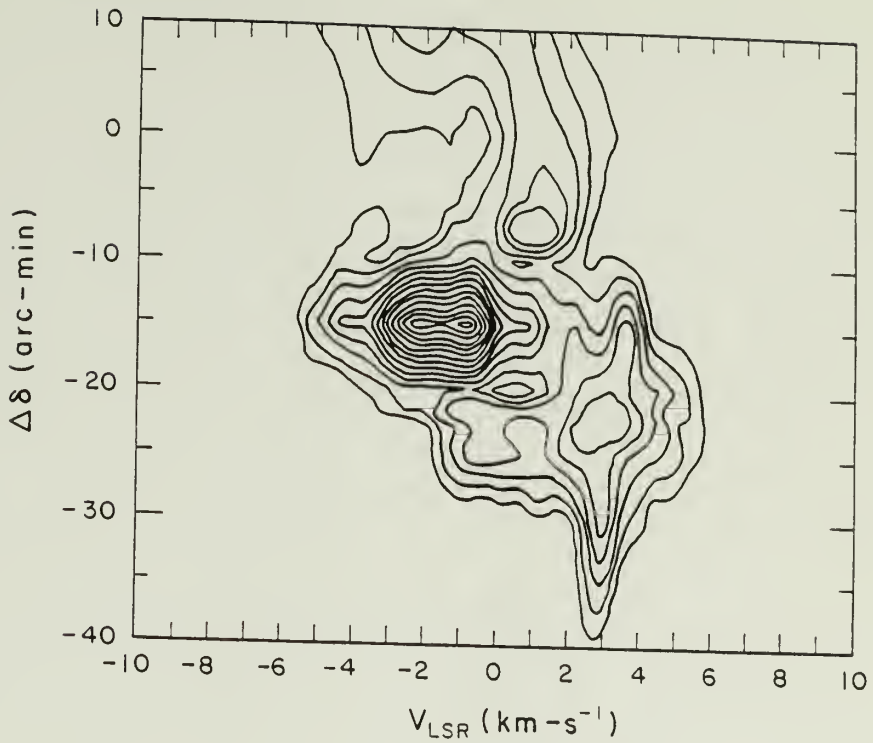

Figure 26

An SV diagram taken in the North-South direction through the Pelican hot spot. North of the hot spot, between $\Delta\delta = 5'$ and $\Delta\delta = -10'$, the strip crosses into a "bay" in the HII region. South of the hot spot, in the direction of the HII region, only redshifted emission is seen. This strip is at $\Delta\alpha = 12.5'$. Contours in all the S117 SV diagrams are taken to be at 2°K intervals.

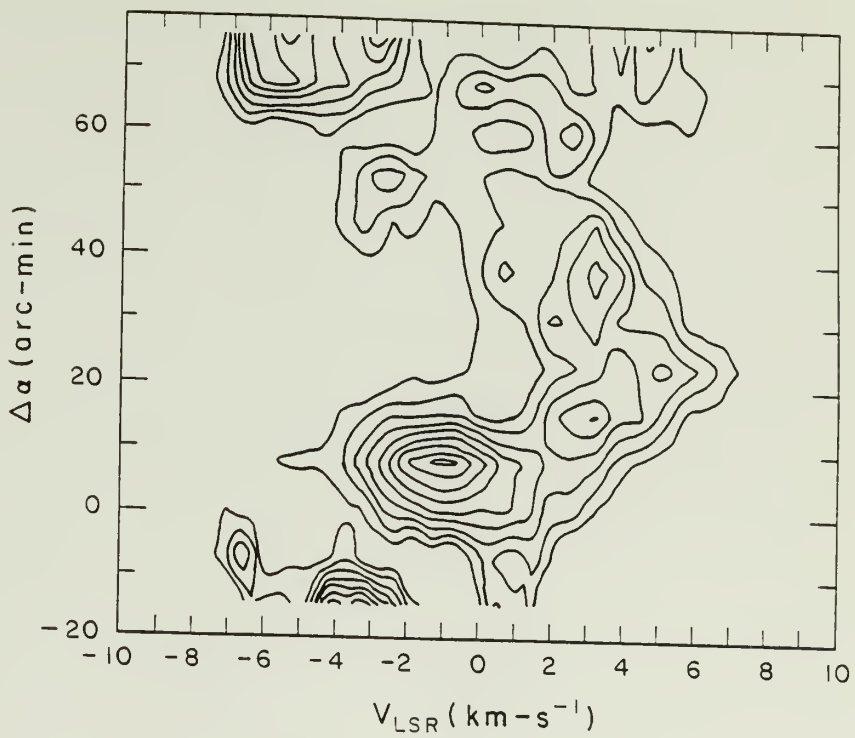

Figure 27

An SV diagram passing East-West at $\Delta\delta = -20'$, south of the Pelican hot spot. Foreground emission associated with the dust lane located between the Pelican and the North American Nebula appears at $\Delta\alpha = 70'$.

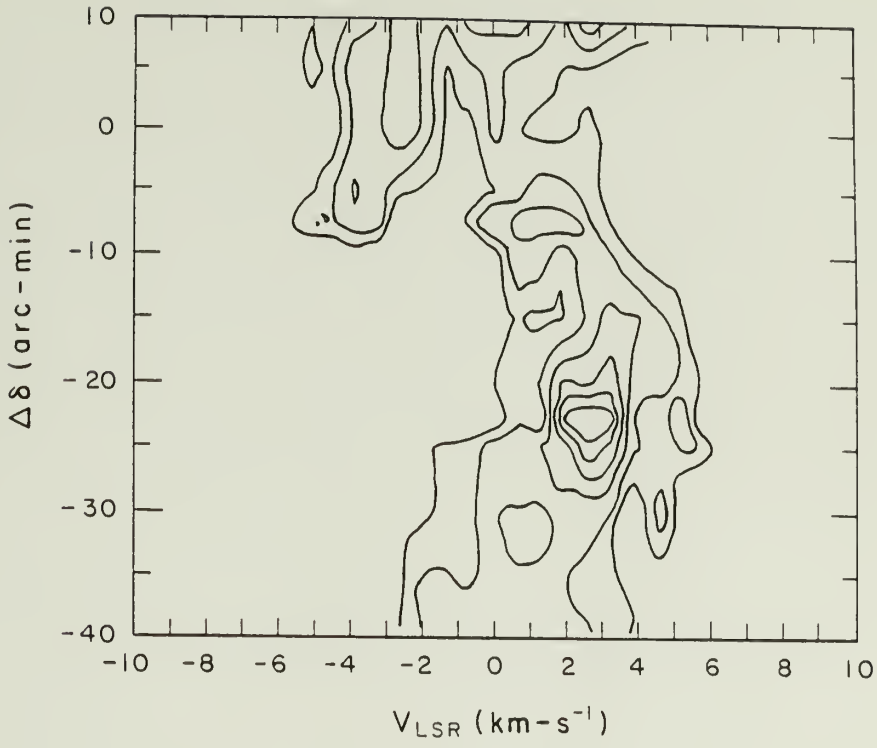

Figure 28

A North-South SV diagram at $\Delta\alpha$ = 30' showing velocity gradients associated with molecular gas at the rear of the Pelican Nebula.

declination of the bright rim in the Pelican is shown in Figure 25. A second strip runs orthogonal to this one in the north-south direction and crosses the CO hot spot in the Pelican (Figure 26). Most of the CO of the western periphery of the Pelican Nebula, near the ionization front that appears to bulge into the W80 HII region, has a velocity near V_{LSR}= 0 km s^{-1}. The center of the bulge has a 25 °K CO hot spot that exhibits a rather broad 10 km s^{-1} line profile. This source appears to be roughly spherical and 5' in diameter, and is associated with infrared source IRS4. Moving eastward along the RA strip, the line profile becomes progressively redshifted, at first abruptly, then more slowly. The zero-velocity component disappears where the ionization front is crossed at $\Delta\alpha$ = 20'. In spectra taken in the HII bay just east of the Pelican I-front, only redshifted CO at V_{LSR} = 3 km s^{-1} occurs. As the strip crosses into the foreground dust lane that separates the N.A. Nebula from the Pelican, negative velocity emission is picked up at V_{LSR} = -3 km s^{-1}.

The magnitude of the splitting of the CO line profile increases as spectra closer to the geometric center of the W80 radio source are considered. Other spatial-velocity diagrams in the east-west direction obtained north and south of the strip through the Pelican hot spot show a characteristic "bow" shaped appearance, with the CO line centroid being systematically displaced towards the red in the region where HII gas is optically visible (Figure 27). The overall picture of the line splitting when one looks toward the HII region and line narrowing at the edge may be seen in Figure 29, where <u>all</u> the

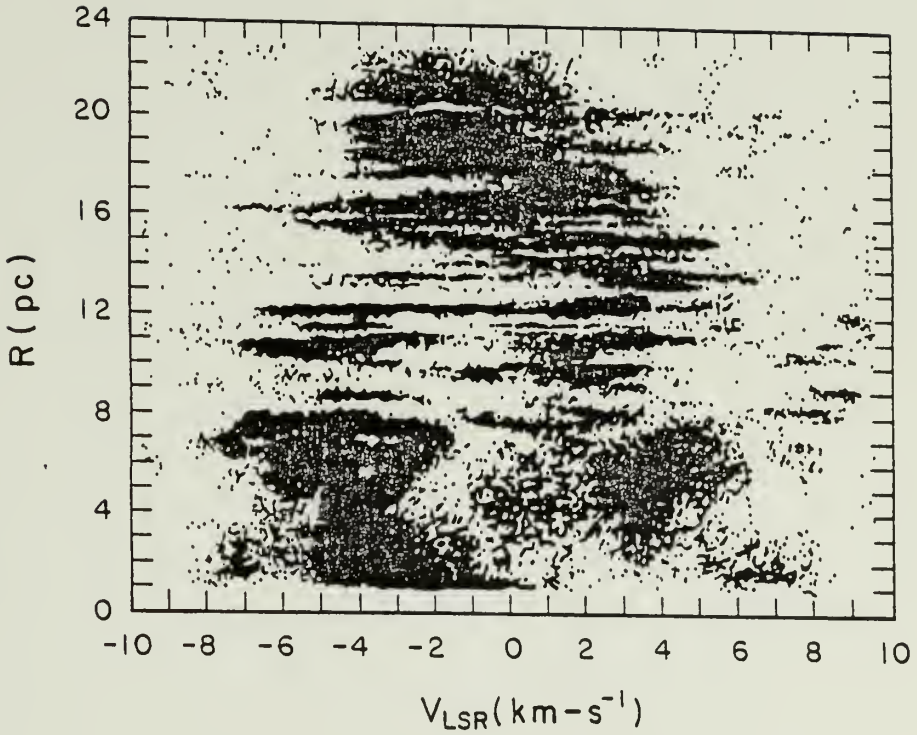

Figure 29

A radius-velocity diagram of CO emission in the northern half of S117. All spectra north of $\Delta\delta = -30$ were used (160 spectra), with the center of the radial coordinate system, R=0, taken to be at $\alpha_{1950} = 20^h53^m15^s$ and $\delta_{1950} = 43°45'00"$, which corresponds to the centroid of the free-free emission. The inclusion of all spectra would tend to fill in the hole near $V_{LSR} = 0$ km s^{-1} due to the peculiar velocity of the thick cloud in front of the southern part of W80 which is too massive to have been dynamically affected by the HII region. The narrowing of emission at large values of R is still preserved, however.

spectra obtained on the north and west half of W80 are combined to yield an overall "radius-velocity" diagram. The vertical axis represents the apparent distance of a particular point from the center of W80. Near the center of the HII region, there is a lack of CO emission at $V_{LSR} = 0$ km s^{-1}. This figure resembles optical slit spectra of the expanding shells of planetary nebulae (Osterbrock 1974). In Figure 30, the mean absolute velocity separation from the cloud rest velocity is displayed. This quantity [ΔV] is defined for each spectrum as

$$[\Delta V] = \frac{\int_{-7}^{5} T_A^2 \, (V - V_o) \, dV}{\int_{-7}^{5} T_A^2 \, dV} \quad ,$$

where the cloud rest velocity V_o is taken to be at -1 km s^{-1}. As might be expected from the earlier discussion, this quantity shows large values near the central regions of W80 but decreases at the HII region periphery. The systematic behavior of the velocity field in the northwestern half of the W80 complex can be interpreted as the emission of a uniformly expanding shell of molecular gas. The shell is incomplete; it has a number of holes where the optical emission of the W80 HII region can be seen. Since the different velocity components all merge into the same feature near the edge of the HII region, all molecular emission features arise from one physically connected cloud whose parts are moving at different velocities.

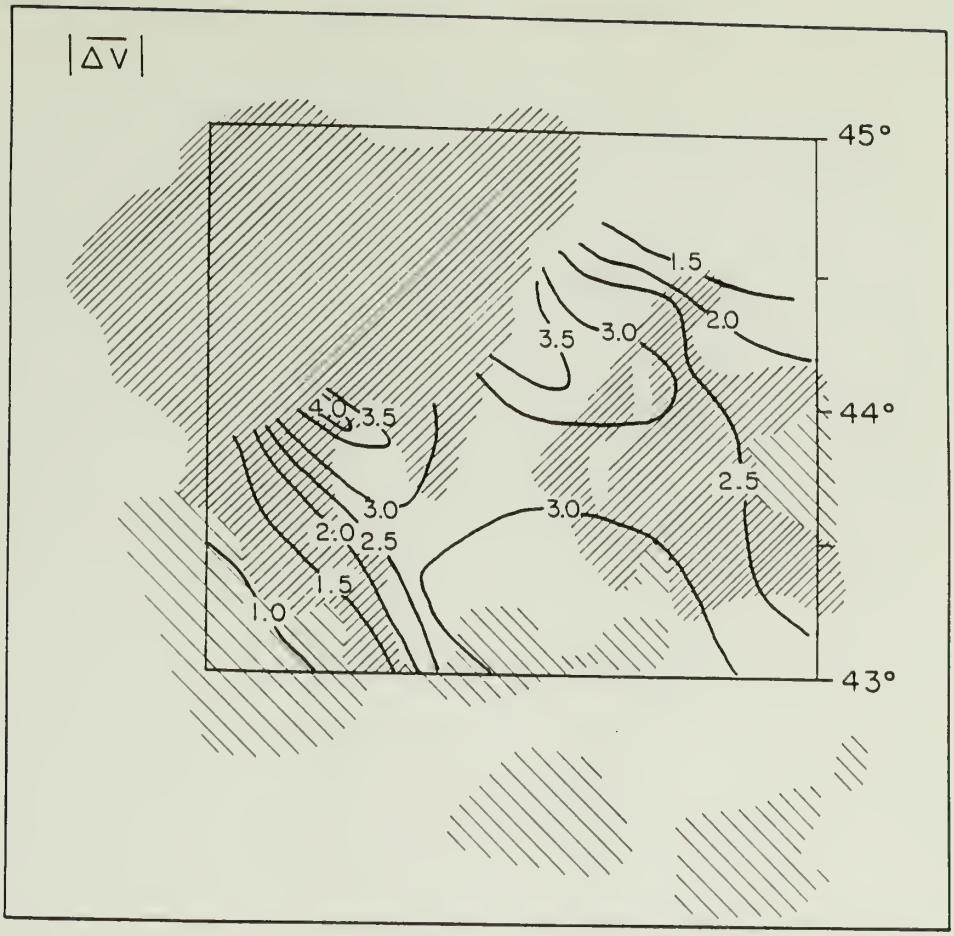

Figure 30

A contour diagram of the first moment of T_A^2 as defined in the text. The squared quantity is used in order to minimize the dependence of the parameter on low-level noise. The raw data were smoothed to an effective resolution of 15' to decrease the effect of small-scale kinematic behavior. Small numbers correspond to emission in a narrow range centered on V_o = -1 km s^{-1}; large numbers indicate emission over a large velocity range or line splitting.

Since the negative velocity gas is found to lie in front of the HII region, the positive velocity behind, and both are connected by intermediate velocity gas at the edge, the molecules are part of an expanding shell surrounding the ionized gas. The best determination of the center of expansion of the molecular gas, obtained by fitting an expanding shell form to the CO data, is close to the centroid of the free-free emission at $\alpha_{f-f} = 20^h53^m15^s$, $\delta_{f-f} = 43°45'$. The expansion velocity is 5 km s^{-1}. The radius of the shell, determined from the free-free maps, the optical nebulosity, and the CO emission, is 1.2°, which corresponds to 20 pc at a distance of 1 kpc.

In the southern portion of W80 (in the "Carribean Sea"), the behavior of the CO emission is not so ordered. In this region, the foreground dust lane shows broad emission lines with some of the emission at V_{LSR} = +4 km s^{-1}, indicating that a mass of gas is falling toward the the HII region from the near side. The western edge of the cloud is at V_{LSR} = 0 - 2 km s^{-1}, close to the ambient cloud velocity observed at the HII region periphery in the north. It is plausible that the kinematics of the southern part of the molecular shell is less ordered than in the north because the shock has not penetrated the entire line-of-sight through the foreground cloud. The extinction here is $A_V \geq 10$ mag, far greater than in the north. The optically visible ionization edge in the southeast ("West Coast of Mexico") is also seen in CO. Two hot spots with T_A = 16 °K occur at the extreme north and south ends of the front. The emission here occurs at V_{LSR}= -0.5 km s^{-1}, close to the value found for the gas near the periphery of the HII region in the north and west.

The mass of the neutral gas may be estimated by using the CO measurements or the extinction caused by the foreground portion of the cloud. The available ^{13}CO data is too sparse to yield a mass estimate for the molecular shell from the ^{13}CO column densities. The thickness of the molecular shell can be estimated from the apparent thickness of the CO ridge at the periphery of the HII region, with the result that $\Delta r = 3 - 6$ pc, assuming a distance of 1 kpc. Employing a mean particle density of 500 cm^{-3} (typical for many molecular clouds where a full analysis of the line formation has been made (Scoville and Solomon 1974, Martin and Barret 1978)), a shell radius of 20 pc, and a thickness of 3 pc, the shell mass is $M_{shell} = 3x10^5 f\ M_o$, where f is the fraction of the shell which is complete. From the fraction of the HII region which is obscured, we judge $f \leq 1/5$ so that the shell mass is about $3 - 6x10^4\ M_o$.

The visual extinction in the foreground dust lane has been measured to be in the range $A_v = 4 - 10$ mag (Goudis and Johnson 1978). Using the extinction values appropriate for the dust lane near the center of W80 and a gas-to-dust ratio of $2x10^{21}$ atoms cm^{-2} mag^{-1}, the column density of gas in the shell is found to be $N_H = 0.8 - 2.0x10^{22}$ cm^{-2}, consistent with the few scattered ^{13}CO measurements and with mass estimate of $M_{shell} = 6x10^4\ M_o$ for a mean $A_v = 4$ mag, a shell radius of 20 pc and a filling factor of 1/5. This mass combined with the expansion velocity of 5 km s^{-1} implies that the kinetic energy associated with the radial expansion of the shell is $1.5x10^{49}$ ergs.

TABLE 4

S117 PARAMETERS

Ionized Gas

	α (1950)	δ (1950)	Size	S_ν	ν (GHz)	n_e (cm^{-3})	M(HII)	Ref.
Envelope	$20^h54^m00^s$	44°00'00"	2°x3°	100 Jy	1.4	9	$1.8x10^4$ M_o	1

Exciting Star - Unknown :Required Q = $5x10^{49}$ photons s^{-1} (O5V star)

Diameter of Nebula = 50 pc

Distance = 1 kpc

Molecular Shell

	α (1950)	δ (1950)	Radius (pc)	Thickness (pc)	Mass (M_o)
Center	$20^h53^m15^s$	43°45'00"	20	3	3 - $6x10^4$

References:

1. Wendeker (1959)

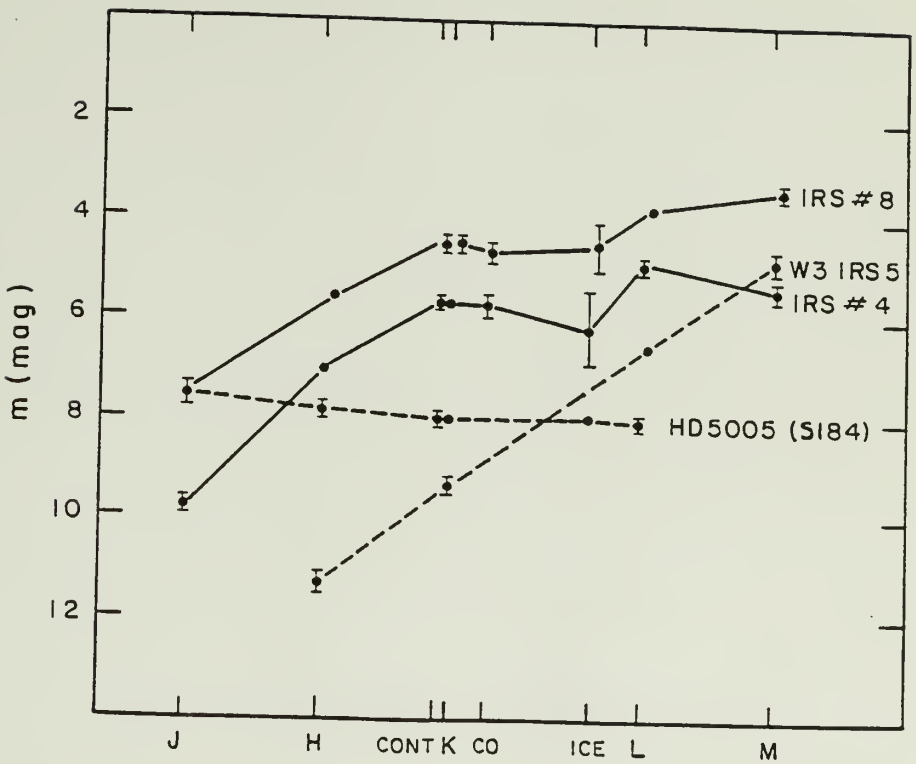

Figure 31

Near-infrared spectrum of the source in the Pelican hot spot (IRS 4). Also plotted are the magnitudes of the bright source IRS 8 located near the centroid of the f-f emission. For reference, the spectrum of the Trapezium like cluster causing the excitation of S184 and containing the O5.5f star HD 5005 is shown. (The distance to S184 is 2.1 pc, about twice the distance to S117). S117 IRS 4 and IRS 8 show the effects of a large amount of interstellar reddening. The spectra suggest that these objects are normal stars, but their spectral types remain undetermined. These sources are bright enough to contribute significantly to the excitation of the region if they are early type stars. Also shown for comparison, is the steep spectrum source W3IRS5.

TABLE 5

CENTERS OF 8'x8' BOXES SEARCHED IN THE NEAR INFRARED

Box	α (1950)	δ (1950)
1	20 48 50	44 15 00
2	20 57 00	43 08 00
3	20 58 40	43 45 00
4	20 52 00	44 23 00
5	20 52 45	44 03 00
6	20 53 45	43 41 00
7	20 56 00	43 35 00

TABLE 6

INFRARED SOURCES FOUND IN THE DIRECTION OF THE S117 MOLECULAR PEAKS

Source	α (1950)	δ (1950)	J	H	K	L	M	Cont	CO	Ice
1	20 53 54.0	43 43 52	10.64	8.48	7.16	6.26	5.92	6.94	7.34	-
2	20 49 05.3	44 13 52	-	10.92	8.22	6.63	-	8.14	7.94	-
3	20 49 14.4	44 21 09	9.76	7.93	7.18	6.55	6.77	7.03	7.34	6.32
4	20 48 49.0	44 15 12	9.69	6.98	5.65	4.85	5.19	5.50	5.74	6.21
5	20 56 40.4	43 14 09	6.58	5.72	5.43	5.24	4.95	5.40	5.44	5.72
6	20 58 52.8	43 46 51	8.52	7.42	6.94	6.50	6.00	6.91	7.20	7.68
7	20 52 57.5	44 03 38	11.29	9.06	7.86	6.73	6.34	7.74	7.84	8.30
8	20 53 54.5	43 40 41	7.47	5.59	4.56	3.73	3.35	4.40	4.71	4.58
9	20 53 54.8	43 43 54	10.52	8.56	7.15	6.16	5.32	7.00	7.26	2.23
10	20 54 03.3	43 40 51	6.36	5.50	5.02	4.76	4.60	5.02	4.89	5.02
11	20 54 08.4	43 41 28	9.31	7.53	6.63	6.03	6.36	6.59	6.52	6.76

1. Cont. filter has effective wavelength of $\lambda = 2.17$ μm and a bandwidth $\Delta\lambda = 0.1$ μm

2. CO filter: $\lambda = 2.40$ μm $\Delta\lambda = 0.10$ μm

3. ICE filter: $\lambda = 3.08$ μm $\Delta\lambda = 0.085$ μm

F. S125

The rest of the sources studied in detail are relatively evolved HII regions with large angular diameters. Attention was drawn to S125 by its nearly spherical appearance on photographs, suggesting a classic Stromgren sphere, and by the detection of hot CO emission from optically obscured regions surrounding the nebula. The initial CO data revealed velocity shifts amounting to a few km s^{-1}, the amount expected for gas that has been swept up in the post-shock layer associated with an expanding older HII region.

S125 is associated with the open cluster IC5146 located at a distance of 900 pc in the Cygnus arm (Walker 1959) at the eastern tip of an extended filamentary dark cloud that stretches about 2 ° to the west. Herbig (1959) found strong optical continuum in the nebular spectrum, indicating the presence of large amounts of reflective dust imbedded in the HII region. Ionization is caused by the BOV star BD 46°3474 located at the center of the nebula.

In a Westerbork synthesis map of S125 presented by Israel (1978), the radio emission arises in exactly the same area visible in photographs, indicating the absence of strong foreground obscuration. The small emission measure of $E = 6 \times 10^3$ pc cm^{-6} and the 1.9 pc diameter of the ionized region give a low mean electron density of $n_e = 57$ cm^{-3}, characteristic of an evolved HII region. The age of the associated star cluster is 3×10^6 yrs as determined by the shape of the main sequence (Walker 1959). The absence of high electron density

concentrations at the boundaries of the HII region suggests that there has been no recent formation of massive stars. The total mass of ionized gas is between 7 and 10 M_o (Israel 1978, Felli and Churchwell 1972).

A large neutral hydrogen cloud roughly 25' in diameter (6.5 pc) and containing about 670 M_o of gas surrounds S125 (Riegel 1967). The 21 cm linewidth of 6 km s^{-1} can be interpreted in terms of either expansion at 3.0 km s^{-1} or turbulence with a one dimensional velocity dispersion of 2.6 km s^{-1}. Low resolution CO observations of the S125 region and the dark filament (Israel 1970) show a shift in the velocity field of the filament from V_{LSR} = 8 km s^{-1} at the position of S125 to V_{LSR} = 3 km s^{-1} 70 arcmin to the west. Lada and Elmegreen (1979) found that the emission near S125 is resolved into three emission peaks when mapped with a 2.6' beam. Elias (1978) surveyed the region at 2 microns in a search for buried infrared sources and found a source near the 33 °K hot spot. Lack of photometric data prevents determination of the nature of this source; it may be a background giant star like most of the near-infrared sources detected in his survey. Despite several searches for H_2O masers, none have been found (Blitz and Lada 1978; this thesis).

1. CO

S125 was mapped in the ^{12}CO line during February 1978 and again in March 1980 in order to study the kinematics and thermal structure of the molecular gas surrounding an HII region or low excitation. The

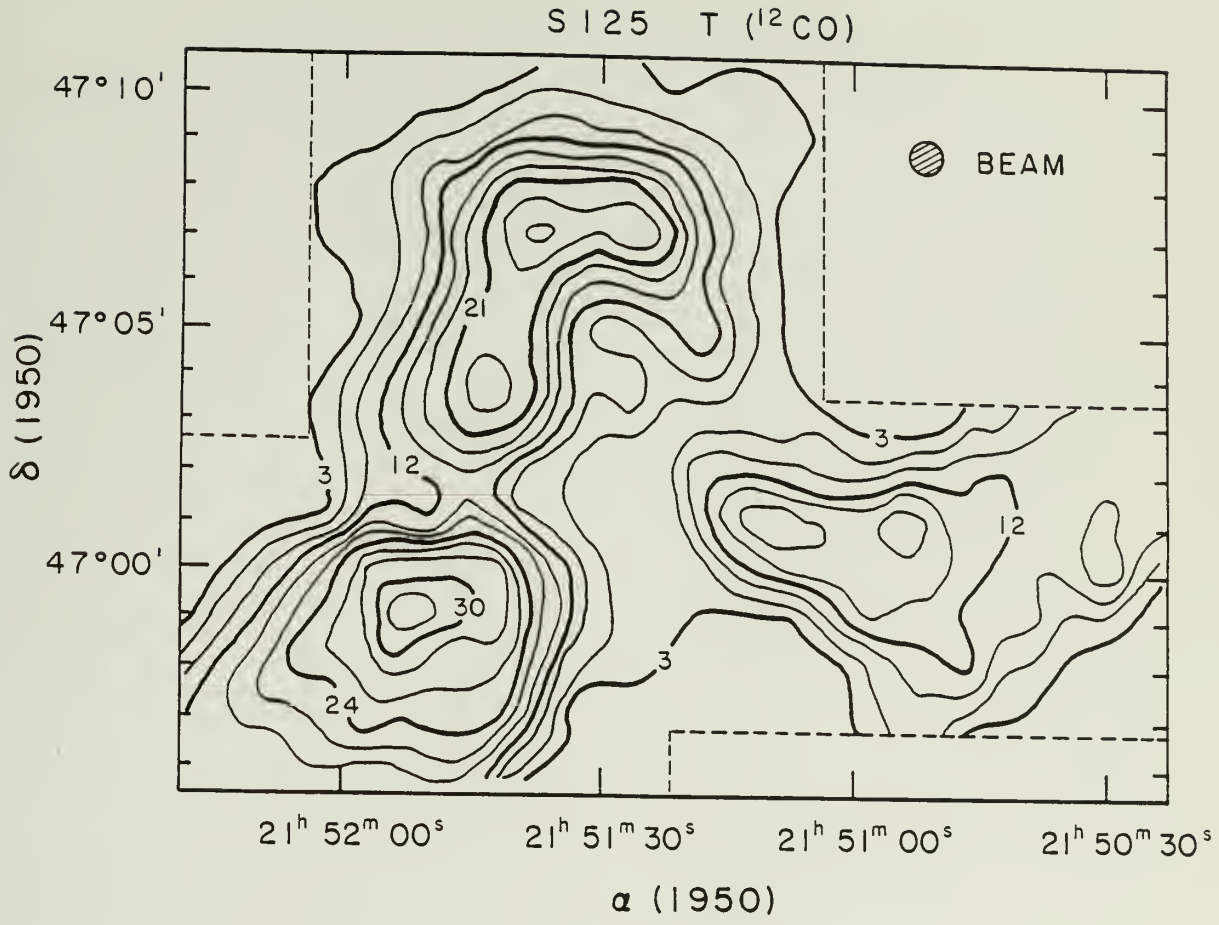

Figure 32

^{12}CO map showing the disrtibution of molecular gas in S125. The (0,0) point corresponds to $\alpha_{1950} = 21^h51^m34^s$ $\delta_{1950} = 47°01'12"$

Figure 33

Four ^{12}CO spectra obtained at the offset positions indicated by the pairs of numbers shown on the right. The top two spectra are in the direction of cloud B. The third spectrum is taken in the direction of cloud A and the bottom spectrum is in the direction of cloud C. The 21 cm atomic hydrogen central velocity and the ionized gas velocity as determined by the centroids of Hα and H142α recombination lines are shown by the dashed vertical lines. The ionized gas is streaming toward the Sun relative to the neutral gas.

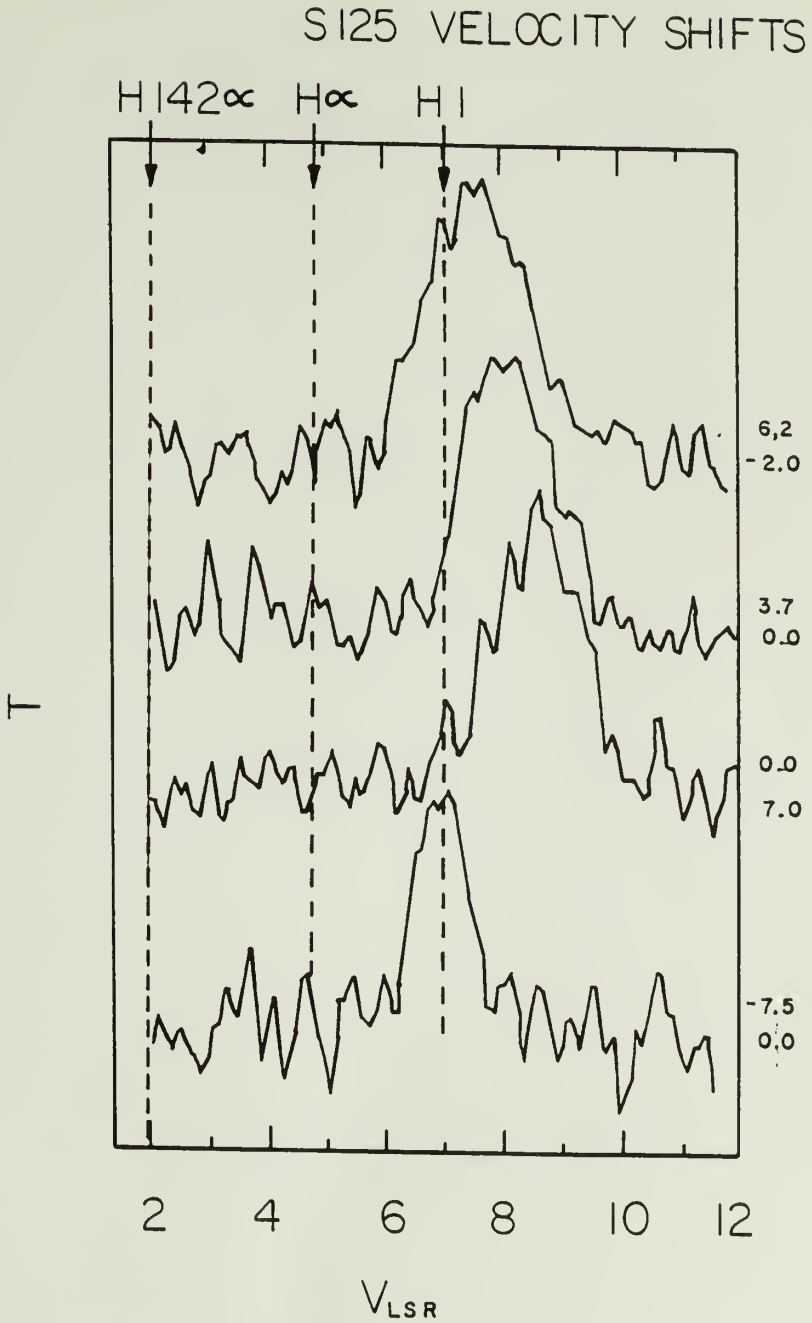
S125 VELOCITY SHIFTS
H142α
Hα
H1
6,2
-2.0
3.7
0.0
0.0
7.0
-7.5
0.0
T
2
4
6
8
10
12
VLSR

resulting ^{12}CO map (Figure 32) shows the three cloud components noted previously but with better spatial resolution.

The northern spot (cloud A) is an elongated ridge running parallel to the northern and eastern edges of the HII region with two or possibly three separate intensity maxima. The velocity of peak emission is $V_{LSR} = 8.5$ km s^{-1}. The south-eastern part of this ridge connects with the 35 °K hot spot located southeast of S125 (cloud B), which has a single well-resolved temperature maximum at $V_{LSR} = 7.8$ km s^{-1}. The velocity difference between cloud A and cloud B is illustrated in the spatial-velocity map of Figure 34 and in the spectra shown in Figure 33. Cloud B exhibits its own velocity gradient in the east-west direction amounting to $\Delta V = 0.7$ km s^{-1} pc^{-1}, with the extreme south-eastern end having the more negative velocity, since the line center is at $V_{LSR} = 6.5$ km s^{-1}. Cloud C, an elongated east-west oriented bar on the western edge of the nebula, has a 17 °K peak at $V_{LSR} = 7.0$ km s^{-1}, making this the lowest velocity hot spot. Figure 35 shows the kinematic relationship between clouds B and C. A long spatial-velocity map based on a strip taken at position angle PA = 64° and running through the free-free emission centroid at $\alpha = 21^h51^m34^s$, $\delta = 47°01'12''$ is shown in Figure 36. This position angle was chosen to pass into the dust lane that extends to the west of the HII region. The dust lane exhibits a gradient of 0.6 km s^{-1} pc^{-1} in a direction opposite to the gradient of cloud B. This strip misses cloud C entirely so the feature at 7.0 km s^{-1} is not visible.

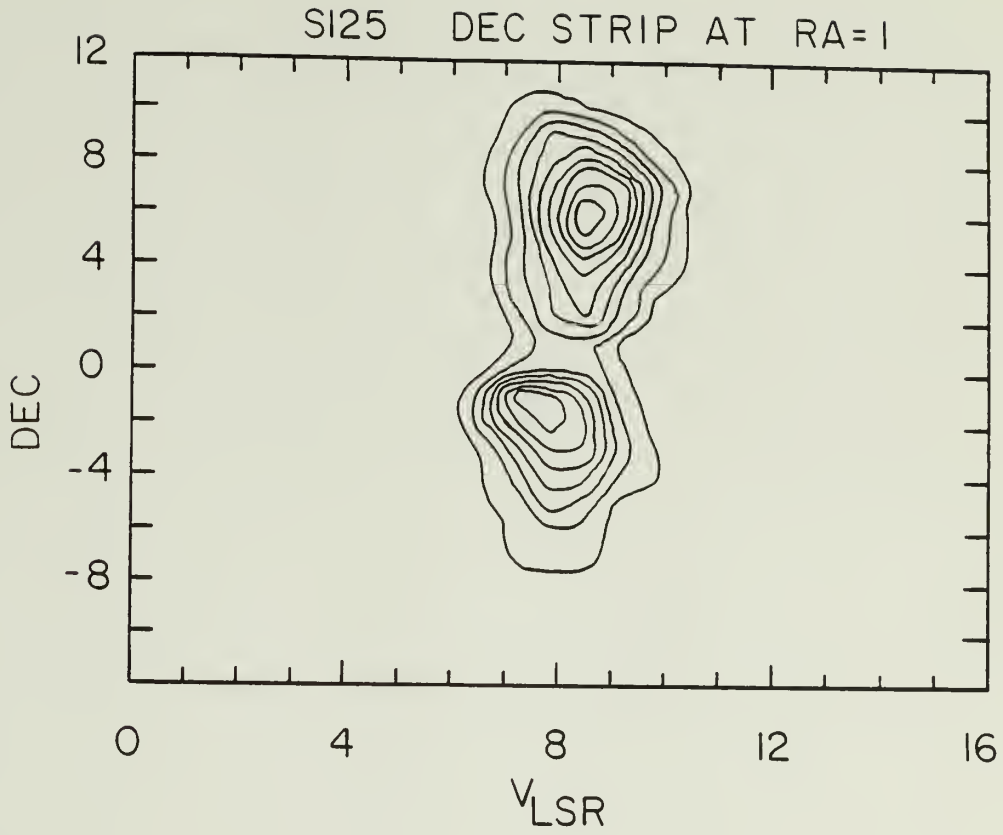

Figure 34

An RA strip ^{12}CO spatial velocity diagram constructed from spectra obtained along a north-south strip at $21^h51^m34^s$ illustrating the velocity difference between cloud A (top) and cloud B (bottom).

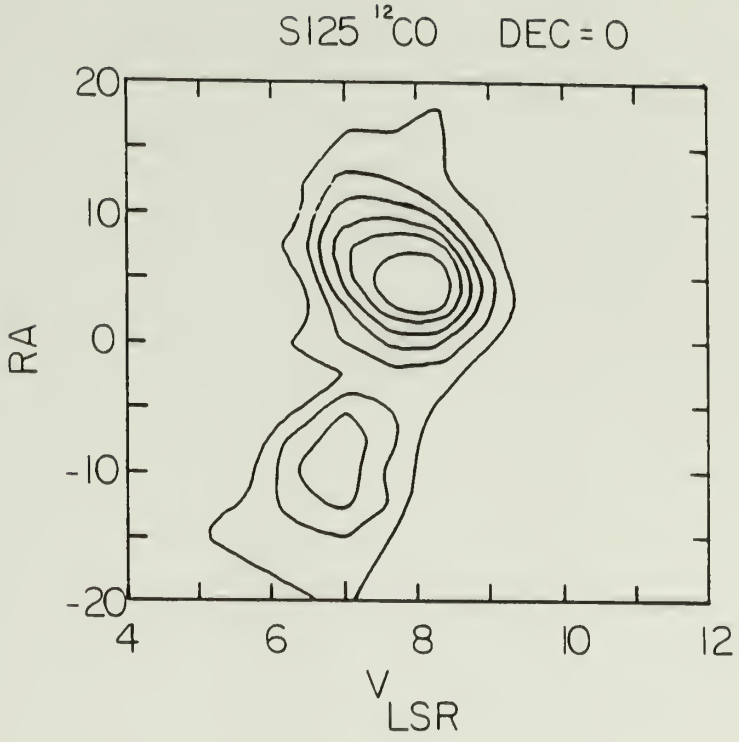

Figure 35

A spatial velocity diagram in RA showing the velocity difference between peaks B and C.

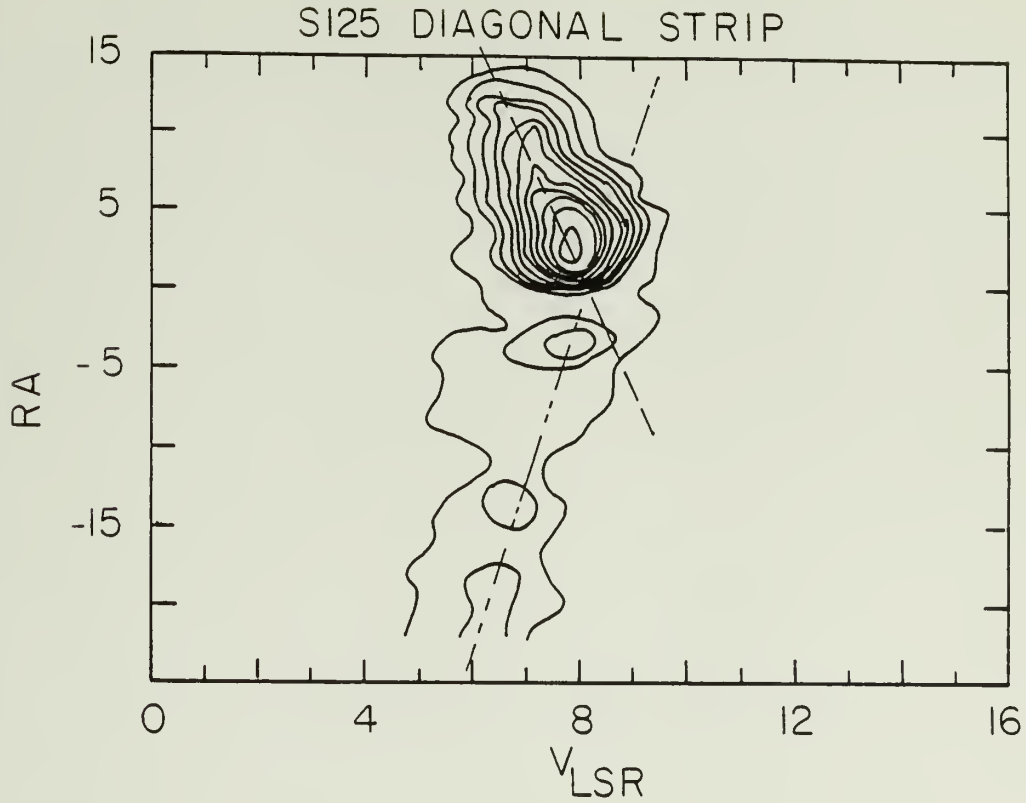

Figure 36

A spatial velocity diagram constructed from spectra running diagonaly accross the HII region from peak B to the long dust lane located to the west. The strip is at position angle PA = 64° and runs through the radio emission centroid at $\alpha = 21^h51^m34^s$ $\delta = 47°01'12''$ (the (0,0) position).

TABLE 7

S125 PARAMETERS

Ionized Gas

	α (1950)	δ (1950)	Size	S_ν	ν	$\langle n_e \rangle$ (cm^{-3})	M(HII)	Ref.
Radio	$21^h51^m30^s$	47°03'00"	5'x5'	1.6 Jy	5.0 GHz	57	7 M_o	1
Hα	"	"	6'x6'	V_{LSR} = 4.8 km s^{-1}				2
Exciting Star - BD 463474 BOV								3

CO Peaks

α (1950)	δ (1950)	V_{LSR} (km s^{-1})	ΔV (km s^{-1})	T_A (°K)
$21^h51^m37^s$	47°07'10"	8.6	2.5	28
$21^h51^m50^s$	46°59'00"	7.7 - 8.0	2.5	32
$21^h50^m54^s$	47°00'40"	7.0	1.5	16

Atomic Hydrogen Cloud	M(HI) = 670 M_o	6.9
Molecular Cloud	M(H_2) = 10^3 M_o	7.0 - 8.6
Distance	900 pc	

References:

1. Israel (1978) 2. Georgelin et al. (1973) 3. Walker (1959) 4. Riegel (1967)

The relative location of the various cloud fragments and the HII region in the line-of-sight is difficult to determine with any certainty. Since none of the clouds correlate with obscuration discernible against the face of the nebula, they are not located in front of the HII region. Strong CO emission from clouds A and B is seen in the direction of visible nebulosity, suggesting that these features are partially behind the ionized gas. No conclusions can be drawn about the relative position of cloud C.

G. S184

Two HII regions selected for detailed study are high density portions of much larger evolved complexes. Both S184 and S155 contain areas of very high obscuration in front of dense concentrations of ionized gas, as determined by aperture synthesis observations. Regions in which the high density ionized gas is directly in contact with a foreground molecular cloud provide a good opportunity to probe the dynamics of ionization/shock front systems.

The HII region S184 (NGC291) superficially resembles the North America Nebula (S117) discussed previously. It is located at a distance of 2.1 kpc (Hogg 1959) and is somewhat smaller, having an optical angular extent of 20 arcmin. Radio emission with a flux density of 22 Jy implies a mean electron density of 22 cm^{-3} (Caswell 1968). The distribution of ionized gas is non-uniform ; an elongated region of high density is situated behind the heavy dust obscuration

visible in the southwest portion of the nebula. This region was mapped at Westerbork by Israel (1978), who shows that a mean electron density of $n_e = 10^2$ cm^{-3} is found here. Although an O8 star emits sufficient UV flux to maintain ionization, the actual exciting star of the HII region is the O5.5f star HD 5005 that is the brightest member of a small Trapezium-like cluster (Georgelin 1975, Ambartsumian 1954).

An extensive HI halo surrounds S184 (Riegel 1967). The atomic cloud contains about 1.6×10^4 M_o of HI and has a pronounced hole at its center where the HII region is located.

The overall distribution of CO was mapped at low resulution by Elmegreen and Lada (1978) and Israel (1980) who find emission from two cloud fragments, one coincident with the foreground obscuration in the southwest and the other located on the eastern edge of the nebula. A line shift of about 1 km s^{-1} was reported by Elmegreen and Moran(1979) at the northern edge of the southwest fragment. This feature was interpreted by these authors as an ionization driven shock front associated with the expansion of S184. The presence of an H_2O maser near the velocity shifted component may indicate that star formation that has been triggered by the shock associated with the line shift.

1. CO

Spatial-velocity diagrams obtained during the initial survey portion of this project revealed a velocity shift at the northern edge of the cloud seen against the dense portion of the nebula. All sub-

Figure 37

The shock in S184 is illustrated by these three ^{12}CO spectra taken at the north-eastern edge of the molecular cloud. The blueshifted compontnt is emission from the shocked gas. The temperature scale has been adjusted so that each spectrum has roughly the same height in the figure. The actual peak temperatures are given below:

Spectrum:	T_A(shock)	T_A(unshifted)	α(1950)	δ(1950)
Upper	4.4	5.8	$00^h49^m42^s$	56°18'20"
Middle	5.4	7.0	$00^h49^m37^s$	56°18'20"
Lower	(3.0)	9.0	$00^h49^m32^s$	56°18'20"

Toward the west, a more modest 2 km s^{-1} line shift persists and is well correlated with with a opaque ridge of dust seen on the PSS red plate.

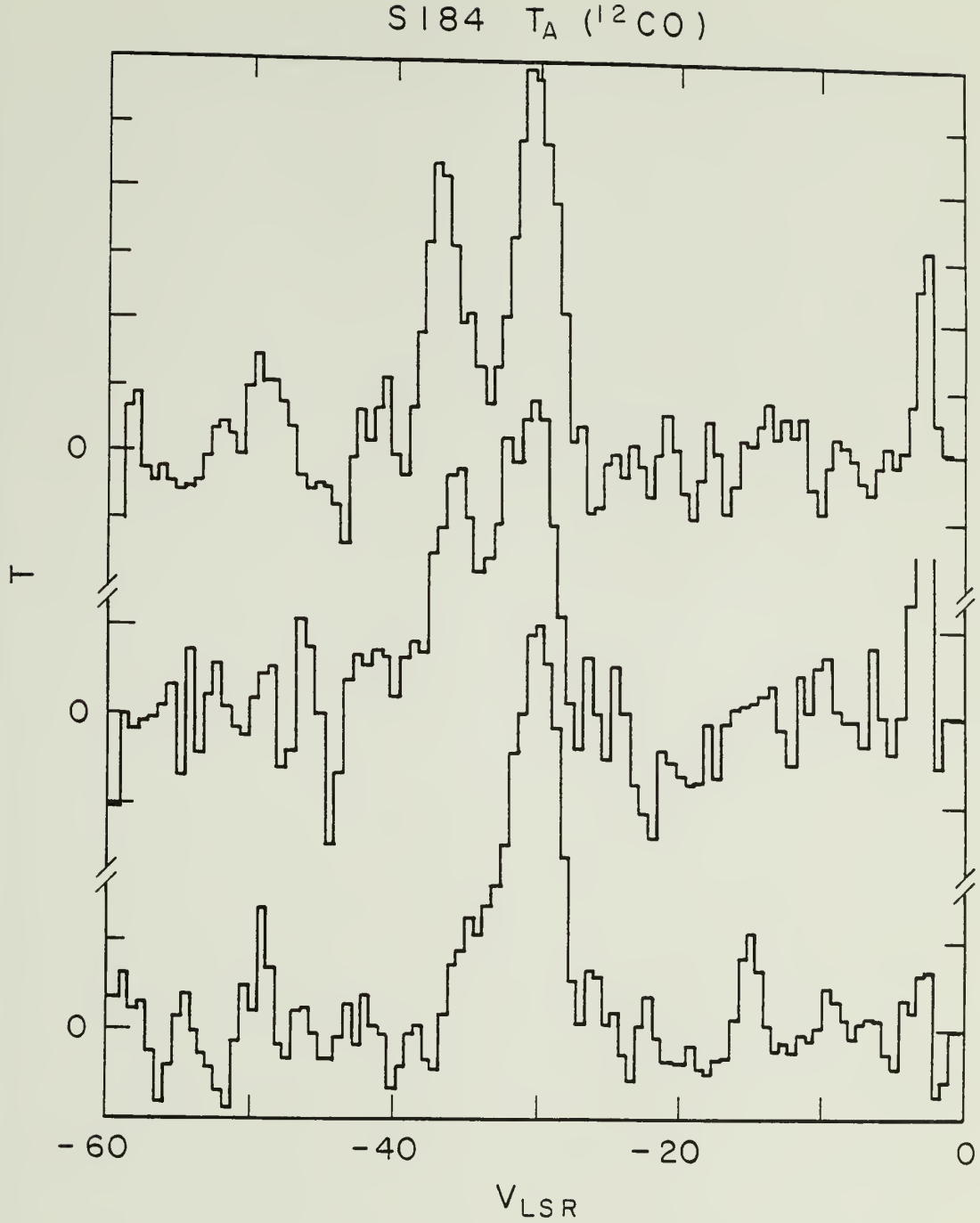
S184 T_A (^{12}CO)
T
0
0
0
-60
-40
-20
0
V_{LSR}

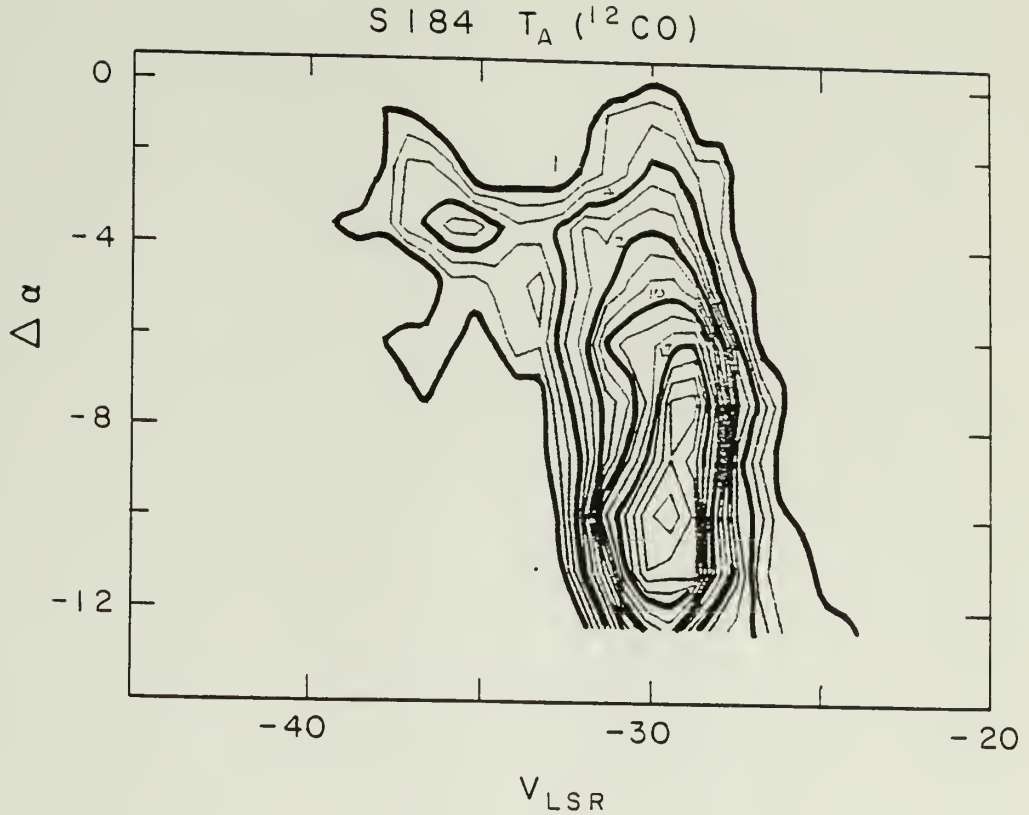

Figure 38

S184. An RA spatial-velocity diagram showing the line dislocation illustrated in the previous figure using 20 spectra at δ = 56°18'20".

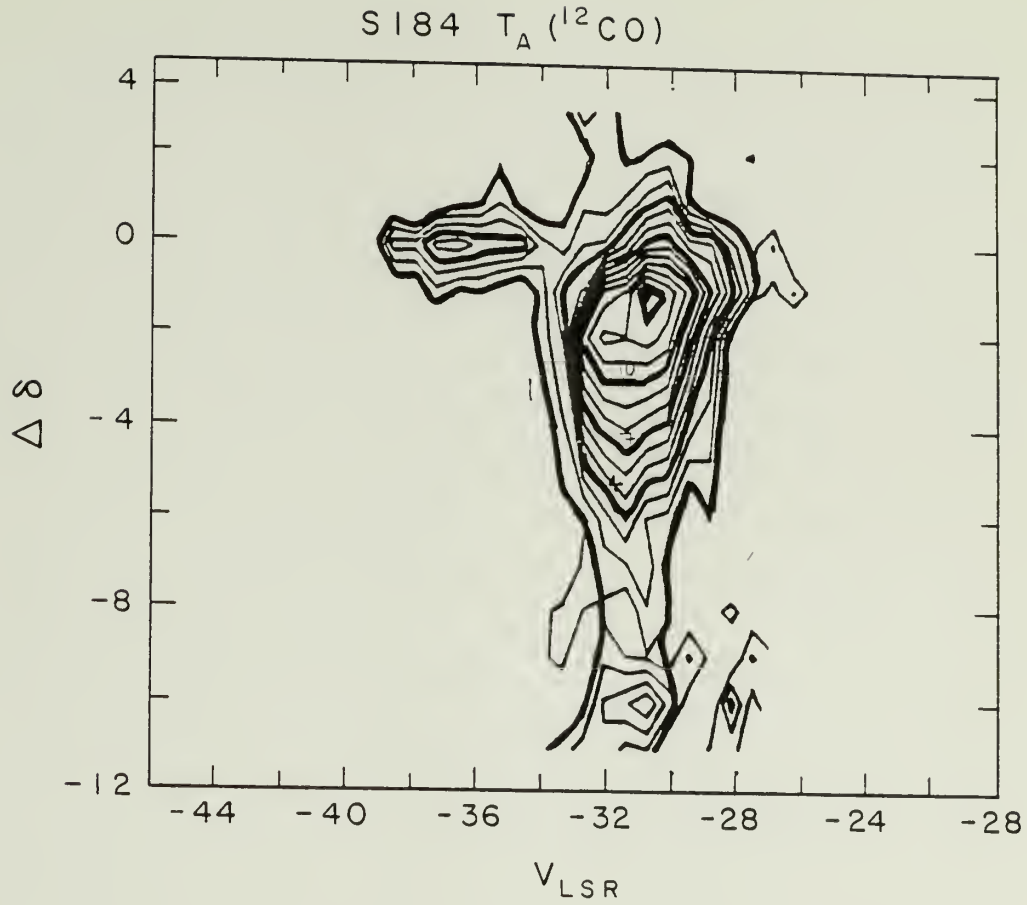

Figure 39

A Dec strip at the position of the shock taken at $\alpha = 00^h49^m42^s$.

TABLE 8

S184 PARAMETERS

Ionized Gas

	α (1950)	δ (1950)	Size	S_ν	ν (GHz)	$\langle n_e \rangle$ (cm^{-3})	M(HII)	Ref.
Envelope	$00^h50^m00^s$	56°21'00"	18'x18'	12 Jy	2.6	50	> 125 M_o	1
Ridge A	$00^h49^m25^s$	56°18'10"	3'x1'	0.25 Jy	1.4	81	3.1 M_o	2
Exciting Star - HD 5005 Spectral Type O6V								
Hα	V_{LSR} = -27.8 km s^{-1}							3
HI	V_{LSR} = -32 km s^{-1}							4
HI Mass	= 16,000 M_o							
H_2 Mass	= 2,000 M_o							5
CO Velocity	= -31 km s^{-1}							
Distance	= 900 pc							

References:

1. Churchwell and Walmsley (1973) 2. Israel (1978) 3. Georgelin et.al (1973)
4. Riegel (1967) 5. Elmegreen and Lada (1978)

sequent observing was devoted to an investigation of the spectral line dislocations seen here.

The CO data show three kinds of velocity behavior. (1) An overall velocity gradient $\Delta V = 0.3$ km s^{-1} pc^{-1} in the north-south direction with the redshift occurring in the north. (2) A component blue shifted by $\Delta V = 2$ km s^{-1} is found superimposed on the CO profiles at the northern edge of this cloud. This is the "shock wave" detected and reported by Elmegreen and Moran (1979). It can be traced over a 6'x2' region, roughly the same size and shape as the high density ionized gas shown in the Westerbork map (Israel 1978). The highest CO temperature in the S184 molecular cloud, $T_A = 15°K$, is reached in the shifted component at the position of the H_2O maser. (3) A negative velocity shift amounting to $\Delta V = 4$-6 km s^{-1} is seen in the weak CO lines that break off from the main line at the extreme northeast corner of the southwest cloud (Figures 37 to 39). The shifted feature shows a gradient of $\Delta V = 1.6$ km s^{-1} pc^{-1} with the negative velocites occurring in the east. This component appears in the direction of several thin filaments of obscuring material seen in projection against the nebula.

H. S155

S155 is the brightest portion of nebulosity associated with the Cepheus OB3 association located at a distance of 725 pc (Sargent 1979, Crawford and Barnes 1970, Blaauw et al. 1959). Several dozen OB stars in this group generate a combined Lyman continuum flux

$Q = 1.32 \times 10^{49}$ photons s^{-1} . The stars, which are spread over a 30x50 pc region, form two subgroups; the younger one located near S155 has an age of 4×10^6 yrs (Blaauw 1959).

Although most of the Ceph OB3 region contains low surface brightness ionized gas, several high density concentrations occur in the south where heavy dust obscuration is found. The most prominent one occurs at the contact surface between the ionized region and a dark tongue of dust that is seen projected against the association known as Cepheus B (Sargent 1977). In high resolution Westerbork maps (Felli et al 1979), the highest electron density clumps occur on the rear side of Ceph B where they are invisible at optical wavelengths.

The dynamic evolution of the gas in the Ceph OB3 association is reflected by the large-scale structure of the atomic hydrogen envelope surrounding this complex (Simonson and Someren-Greve 1976). The 8° diameter shell containing 5.3×10^4 M_o of HI exhibits an expansion velocity of V_{exp} = 10 km s^{-1} for a total kinetic energy of 5×10^{49} ergs.

Sargent (1977) found a large 20x60 pc fragmented molecular cloud in the southern part of the Ceph OB3 complex. No systematic velocity shifts were observed in the CO line over most of the cloud. The two hottest clumps of gas, Ceph A and Ceph B, protrude into nebulous regions of the complex and were selected for more detailed mapping in the present study.

1. CO in Cepheus B

Cepheus B contains gas that may have been accelerated in shocks associated with the ionization front in S155. The FCRAO ^{12}CO map of this region (Figure 40) shows that this molecule has narrow lines of width 2.8 km s^{-1} and a temperature of T_A = 32°K at the peak position, making this the hottest region of the Ceph OB3 molecular cloud. The high density ionized gas on the far side of the molecular cloud is located where the CO profiles are blueshifted relative to the rest of the cloud. Although most of the CO in the complex is observed at V_{LSR} = -10 to -11 km s^{-1}, the Ceph B clump is centered at V_{LSR} = -12.5 km s^{-1}. At the extreme northern edge, weak emission at V_{LSR} = -16 km s^{-1} occurs. As shown in Figures 41 and 42, the transitions between the ambient cloud velocity and the velocities observed in Ceph B occur suddenly over a 1 or 2 arcmin region in each spatial-velocity strip. A notable exception to this occurs in the extreme west, where a velocity gradient is observed to extend over many arcminutes in a north-south running spatial-velocity diagram. This strip, however, runs nearly tangent to the cloud's western edge.

The ^{13}CO observations, although not as extensive, confirm the kinematic behavior seen in the ^{12}CO data. The blueshifted component at V_{LSR} = -16 km s^{-1} at the extreme northern end of the cloud has very weak lines in this isotope, indicating low molecular column densities at this velocity. An estimate of the mass of this cloud, based on the ^{12}CO and ^{13}CO line ratios, gives a value M = 1.0×10^3 $M_\odot$. Assuming

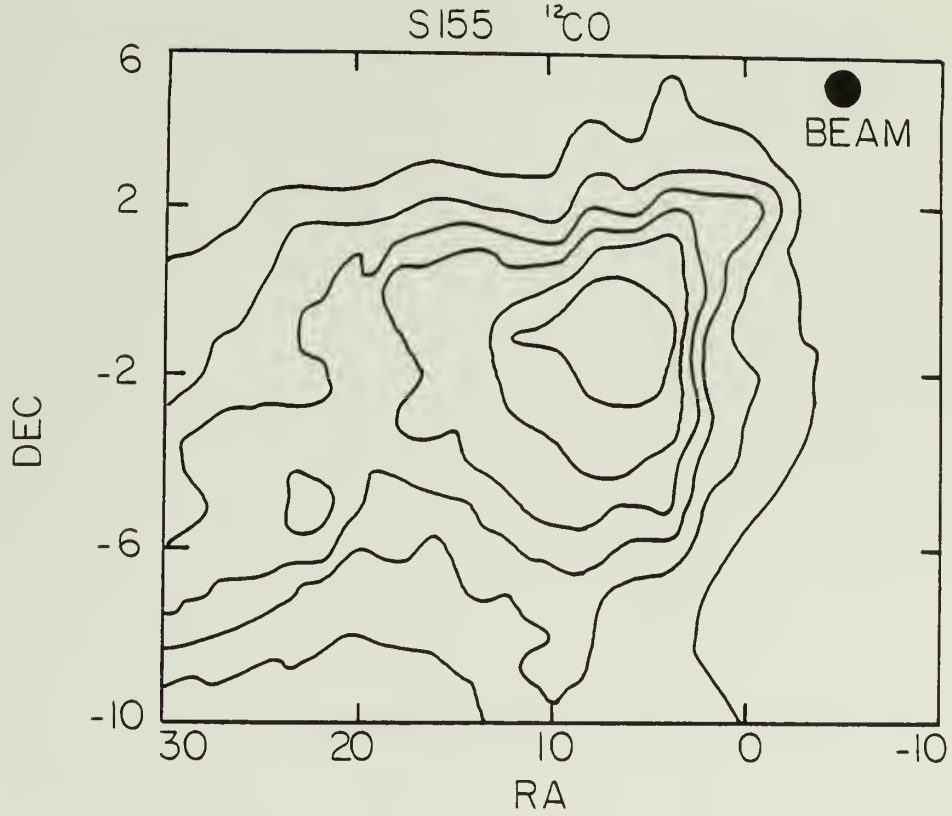

Figure 40

A ^{12}CO map of Ceph B (S155). The (0,0) reference coordinates correspond to $\alpha_{1950} = 22^h55^m00^s$ $\delta_{1950} = 62°20'00''$. Contour levels are set $T_A(^{12}CO) = 5, 10, 15, 20, 25,$ and 30 °K.

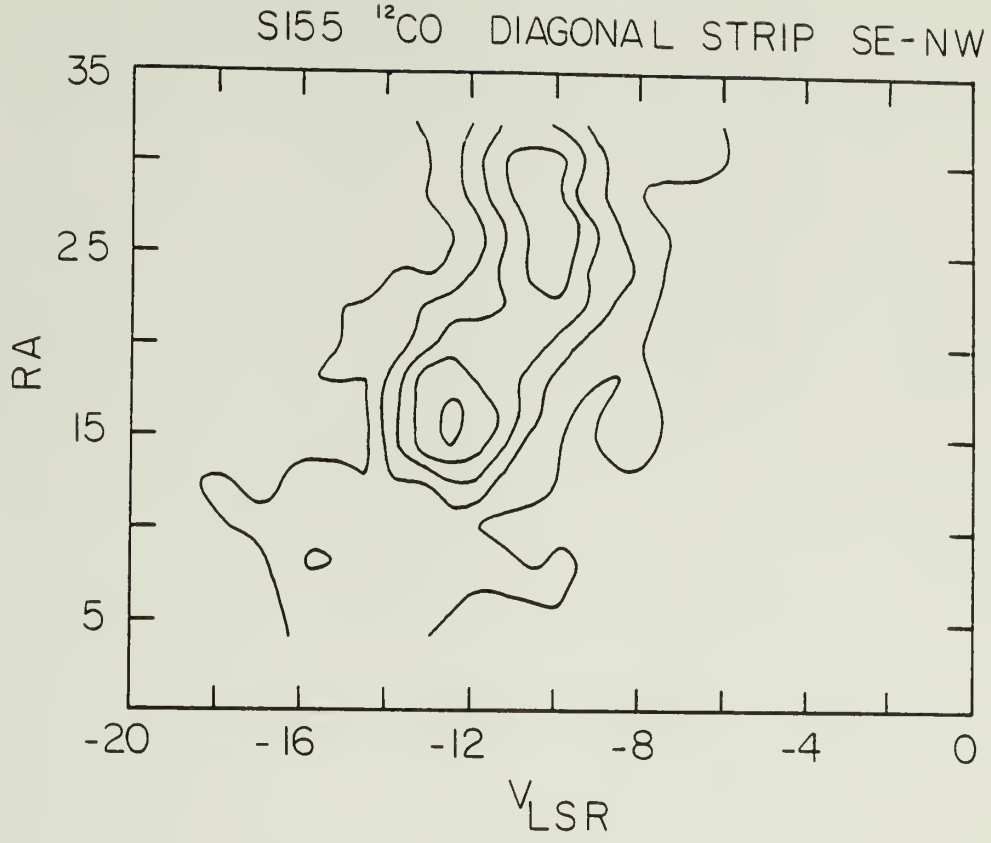

Figure 41

A ^{12}CO spatial velocity strip cutting across Ceph B from the southeast (top) to the northwest (bottom), showing the velocity transitions between a portion of the ambient cloud at V_{LSR} = -10 km s^{-1} (top), the bulk of Ceph B (middle), and the weak blueshifted line at V_{LSR} = -16 km s^{-1} (bottom). Contour levels are at $T_A(^{12}CO)$ = 5, 10, 15, 20, and 25 °K.

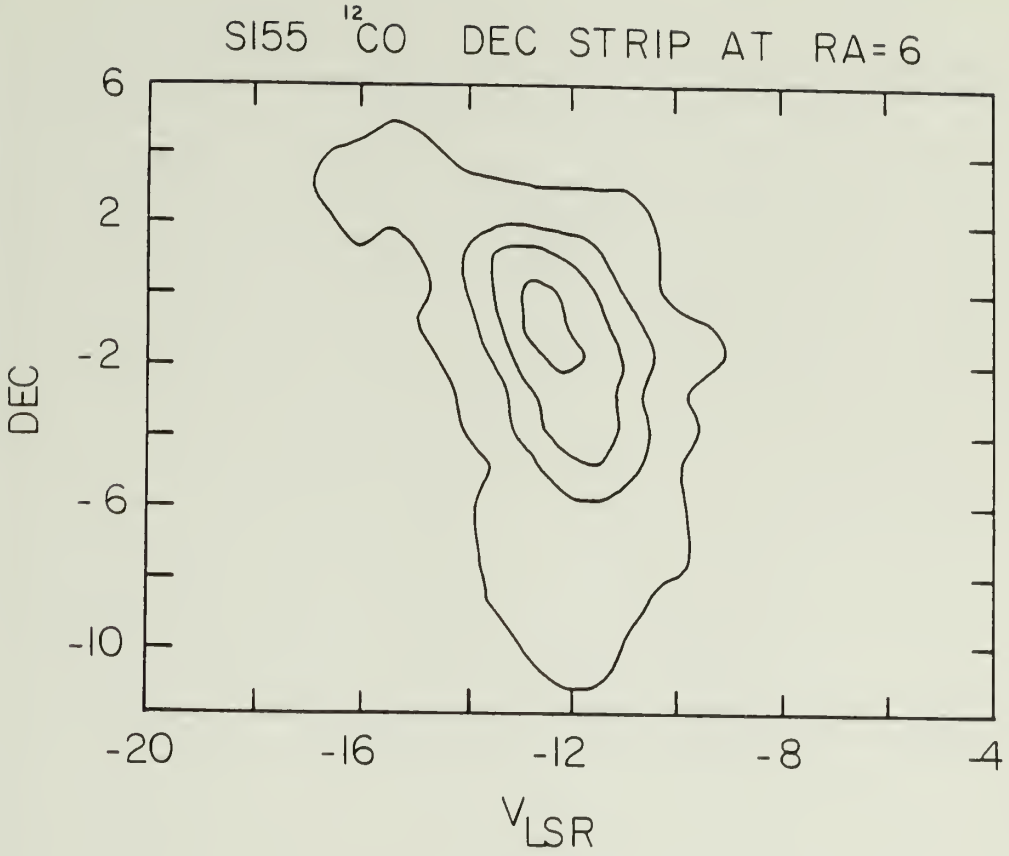

Figure 42

A ^{12}CO spatial-velocity diagram constructed from spectra running along a north-south strip close to the western edge of the Ceph B cloud. Note the emission at $V_{LSR} = -16$ km s^{-1} near the top of the figure. Most CO emission in the Ceph OB3 association is centered at $V_{LSR} = -10$ km s^{-1}. Contour levels are at $T_A(^{12}CO) = 4,8,12,16$ °K. The coordinates are refered to the (0,0) position at $\alpha_{1950} = 22^h55^m00^s$ $\delta_{1950} = 62°20'00"$

TABLE 9

S155 PARAMETERS

Ionized Gas

	α (1950)	δ (1950)	Size	S_ν	ν (GHz)	$\langle n_e \rangle$ (cm^3)	M(HII)	Ref.
Envelope	$22^h55^m00^s$	62°20'00"	22'x10'	34 Jy	0.4	30	170 M_o	1
Central Reg	$22^h55^m00^s$	62°20'00"	10'x5'	7 Jy	0.6	60	18 M_o	1
Source #9	$22^h55^m08.5^s$	62°21'36"	40"x40"	0.15 Jy	5.0	422	0.05 M_o	1

Exciting Star - HD 217086 Spectral Type O7n (and other Ceph OB3 stars)

Neutral Gas

CO Peak T_A = 32°K V_{LSR} = -12 km s^{-1} ΔV = 2.5 km s^{-1}

H_2 Mass (Ceph B only) = 1000 M_o

HI Mass (entire complex) = $5x10^4$ M_o 2

Distance = 725 pc 3

References:

1. Felli et al. (1978) 2. Simonson and Someren-Greve (1973)
3. Walker (1959)

that this mass is distributed uniformly in a spherical volume 8' in diameter, a mean density $n(H_2) = 8 \times 10^3$ cm^{-3} is computed. Two positions near the cloud center were searched for C_2H and HCN, with no lines being detected at the 1°K level, indicating a lack of high density (10^5 cm^{-3}) gas.

There is no evidence of ongoing star formation within this cloud fragment. No near-infrared counterpart of the 20 micron source CRL 3000 has ever been detected and repeated searches for H_2O maser emission have yielded negative results. In the absence of a buried heating source, the proximity of several luminous Ceph OB3 stars must play a dominant role in the energetics of this hot cloud.

1. CO in Cepheus A

A current episode of star formation seems to be occurring in the portion of the Ceph OB3 cloud known as Ceph A. The CO line here exhibits self-reversal (Sargent 1977) and broad wings at least 40 km s^{-1} in extent (Rodriguez et al 1980a). A strong H_2O maser (Blitz and Lada 1979), an infrared source and a cluster of compact HII regions (Beichmann et al. 1979), and a Herbig-Haro object (Rodriguez et al. 1980b) point to Ceph A as a vigorous site of active star formation. The FCRAO observations consist of a cross of points extending N-S and E-W, with the intersection centered on the position of broadest CO line wings. The observations show the asymmetry in the CO wings first pointed out by Rodriguez (1980a), as well as the reversal seen by Sargent (1977). Although an analysis of the energetic

phenomena taking place in the core of Ceph A is beyond the scope of this work, it is significant to point out that spectacular line broadening and velocity shifting occur in regions of very recent star formation prior to the development of normal HII regions. The magnitude and scale of the effects resulting from activity at a star forming site can easily mask the subtler line shifts and heating caused by evolving ionization fronts associated with normal HII regions. While the velocity shifts and heating in Ceph B are probably the result of interaction with nearby OB stars, the spectacular behavior seen in Ceph A probably originates from internal activity caused by a newly forming star.

C H A P T E R III

ENERGETICS OF THE MOLECULAR CLOUD BOUNDARY LAYER

A number of CO hot spots with temperatures above $T_A = 30°$ were found in the observational phase of this study. In the giant HII region complexes, hot spots are found in molecular cloud cores, usually in association with compact HII regions, or luminous infrared sources. Most of the clouds studied in this investigation are small, isolated and relatively simple, often having only one heat source. In some of these regions (such as S87), the total luminosity of the central sources is too small to heat the surrounding dust to the observed CO temperature. In others (S125, S155) buried near infrared sources are not seen at present sensitivity levels and the close proximity of the heated areas to the HII regions suggests that the gas could be heated directly by the UV flux, rather than indirectly by collisions with warm dust grains. It is argued that photoelectrons ejected from grains can heat the boundary layer molecular gas sufficiently to explain the observed hot spots in these sources.

Given the luminosity of the central source, an upper limit to the dust temperature can be obtained by balancing the heat gain from absorption of stellar radiation with radiative losses (Goldreich and Kwan 1974, Kwan and Scoville 1976). The upper limit for the dust temperature is

$$T_d(r) = 49° \, f^{-1/5} \, (2\times10^{17} \text{ cm} / r)^{2/5} \, (L / 10^5 \, L_o)^{1/5} \qquad (3)$$

where observations of Orion indicate that the value of f, the 50 micron dust emissivity, is 0.09. Detailed modeling of the IR radiative transfer indicates that beyond the distance at which most of the stellar radiation is absorbed, the actual temperature of the dust can be 50% less than the value predicted by equation (3). The gas temperature depends on the rate of energy transfer between the gas and the dust as well as on the molecular cooling rate. The coupling between gas and dust via collisions heats the gas at a rate

$$\Gamma_{gd} = 2.4\times10^{-33} \sqrt{T_g}(T_d - T_g)n_H^2 \text{ (erg s}^{-1} \text{ cm}^{-3}) \qquad (4)$$

(Goldreich and Kwan 1974, Goldsmith and Langer 1978). The gas temperature is closely coupled to the dust temperature for $n \geq 10^5$ cm^{-3}.

A. Heating in the S87 Molecular Cloud

One of the most striking features of the S87 cloud is the presence of a well resolved hot spot centered on the compact HII region, an H_2O maser, and an IR source. Since, this cloud is isolated and hot, it is well suited for analysis of the temperature profile and comparison with theories of molecular heating and cooling, in a situation typical of many star forming regions. Using a temperature of T_{87} = 17.5°K at a distance from the cloud center r_{87} = 2.4 pc, determined from the temperature profile for S87, a central source luminosity $L_{87} \geq 1.3\times10^5 \, L_o$ is required to heat the dust to the observed gas temperature. The presence of obscuration in the cloud and a lower mean

density than $n = 10^5$ cm^{-3} raises the minimum required central source luminosity considerably above this value if gas-dust collisions are responsible for heating.

The infrared observations can be used to place a limit on the actual source luminosity and test the importance of dust heating in this cloud. The spectrum of S87 IRS1 can be fit with a power law distribution in the flux density between 1.3 and 11 microns, but rocket measurements in the AFGL catalog (Smith et al 1979) indicate a flat spectrum between 11 and 20 microns. The luminosity of IRS1 between 1.3 and 20 microns is $L_{1.3-20} = 6 \times 10^3\ L_o$, assuming a distance of 2kpc, but the total luminosity depends critically on how the spectrum behaves at wavelengths longer than 20 microns. Assuming that the spectrum remains flat out to 100 microns, $L = 4.4 \times 10^4\ L_o$, comparable to the total luminosity of a B0 star on the main sequence (Allen 1973) required to excite the HII region. Unless the spectrum rises steeply between 20 and 100 microns (with a spectral index ≥ 2.5), the total luminosity of the IR source imbedded in S87 is insufficient to heat the molecular cloud to the observed temperature. Although IRS 2 may also be an imbedded source, its spectrum indicated that its contribution to the luminosity of the S87 core is negligible. The available data suggests a discrepancy between the observed central luminosity of this cloud and what is required to explain the observed temperature by gas-dust coupling. Long wavelength far infrared observations are required to clarify the source luminosity.

B. Heating of the S125 Cloud

The molecular cloud surrounding S125 contains two CO peaks with temperatures around 30°K. A 2.2 micron source has been found near the 33°K hot spot in cloud B that has a K magnitude between 7 and 8 (Elias 1978). Not enough data is available on this source to determine its nature. The temperature distribution in this hot spot, when used in equation (3) and (4) requires a source with a luminosity in excess of 4×10^3 L_o, corresponding to a B3 star on the main sequence, in order to heat the gas to the observed temperature with warm grains.

The northern hot spot does not contain a known infrared source. A compact radio source near the position of peak temperature exhibits a linear triple structure that is common in radio galaxies and is probably a background source unrelated to the cloud (Felli et al 1978). The absence of an internal energy source implies that the dust may be heated from the outside by starlight from the cluster IC 5146. In order to reach a gas temperaure of 30°K, a cluster luminosity greater than 10^5 L_o is required if the hot spot is 1 pc from the stars, equivalent to the projected distance from peak A to the central star. This luminosity requirement is at least 10 times the total luminous output of the B0 type central star in the HII region. This is a relatively sparse cluster containing mostly stars later than type A; the contribution of all the stars is at most a few times the luminosity of the most luminous member, the B0 star (Walker 1959).

The radiation field from the star cluster can heat the dust in the surrounding clouds to a temperature of about 25°K, assuming the

clouds are about 1 pc from the dominant source of luminosity. Efficient coupling between the gas and dust requires densities in excess of 10^5 cm^{-3}. Assuming that the entire 10^3 M_o of molecular gas is contained in the volume equivalent to two 1 pc diameter spheres (roughly the volume associated with the gas inside the 21°K contours of hot spots A and B), a mean density of $2x10^4$ cm^{-3} is found. At this density, the dust needs to be almost a factor of two hotter than the gas (Goldreich and Kwan 1974) increasing the luminosity requirement of the central cluster by more than an order of magnitude. If the distribution of the gas were highly clumped so that much of the beam samples very dense concentrations whose gas-dust coupling is efficient, the discrepancy between required and available luminosity is eased. As in S87, a direct measurement of the dust temperature in the far IR is essential to clarify the energetics.

C. S155

The molecular cloud Ceph B in S155 appears to be externally heated by radiation from some of the exciting stars of the Ceph OB3 association. Felli et al.(1978) argue dust in the HII region is heated to T_d = 150°K by the O7 star HD 217086. The radiation emitted by the dust peaks near 20 microns and is responsible for the infrared source CRL 3000. Dust inside the molecular cloud can be heated to T_d = 30°K by these stars. This is close, but slightly less than the gas kinetic temperature of 35°K derived from the CO measurements. As in the case of S125, the mean density of n = 10^4 cm^{-3} deduced from the

cloud mass and volume may not provide sufficient coupling between gas and the dust to explain the observed temperature by collisions with warm grains. Recent far-infrared observations by Loren et al. (1980) provide further evidence that the gas is not energized by the dust. The peak of the far infrared emission does not coincide with the CO peak. Furthermore, the measured dust temperature in the molecular cloud is not high enough to heat the gas.

D. The Photoelectric Heating of Boundary Layer Gas

The observations suggest that the gas cannot be heated just by the energy input through collisions with warm grains. Two problems arise: (1) The dust temperature seems to be less than the inferred gas kinetic temperature, and 2) the gas density may be less than 10^5 cm^{-3} required for efficient coupling. In this section another, more efficient mechanism of energy transfer that is expected to operate in the vicinity of HII regions where there is an abundant supply of UV photons beyond the Lyman limit will be explored.

The heating of interstellar clouds by electrons photoejected from grains has been discussed by a number of authors (Watson 1972, deJong 1977, Draine 1978). Here, the effect is investigated under conditions that are characteristic of the boundary layer of molecular clouds adjoining HII regions. The great potential of the photoelectric effect for heating the gas surrounding an HII region can be demonstrated by considering the energy input of a typical B0 main sequence star which has an ultraviolet luminosity of

$L_{UV} = 1.0 \times 10^3\ L_o$ between 912 and 1500 A° (Kurutz 1979, Allen 1973). Assuming a UV grain absorption length of $n_g \sigma_g = 1.5 \times 10^{-21}\ n\ cm^{-1}$ (Bohlin 1975), most of the UV is absorbed when a column density of hydrogen atoms amounting to $N = 10^{21}\ cm^{-2}$ is traversed. If a fraction Y of the absorbed UV photons result in the ejection of electrons (photoelectric yield), the net heating rate per unit volume is

$$\Gamma = L_{UV}\ Y\ \eta\ /\ 4\pi\ r_{II}^2\ d_{abs}$$

where η is the ratio of electron kinetic energy to the incident photon energy, r_{II} is the HII region radius (star is assumed to be centrally placed), and d_{abs} is the characteristic UV absorption length scale given by $d_{abs} = 10^{21}/n_H$. For Y = 0.1 and η = 0.2 the heating rate is

$$\Gamma = 6 \times 10^{-21} \left(\frac{L_{UV}}{10^3\ L_o}\right)\left(\frac{R_{II}}{10^{18}\ cm}\right)^{-2}\left(\frac{n}{10^3\ cm^{-3}}\right)\ erg\ cm^{-3}\ s^{-1}$$

Such a large heat input is clearly important to the energetics of the gas adjacent to an HII region.

The principle limitation on the efficiency of the photoelectric effect near the edge of a cloud facing an HII region results from the development of a positive charge on the grains as a result of photoejection. The value of η diminishes for a charged grain since the photoelectrons can lose a considerable fraction of their kinetic energy in climbing out of the potential well. The grain charge is

determined by the balance between photoemission and the recombination rate of electrons. In the mostly neutral medium outside an HII region, the electron density is determined by the ionization equilibrium state of metals since the contribution of the photoelectric effect to the total electron population is minimal. For a stellar radiation field of flux density F_ν which has been attenuated by geometrical dilution and dust, the equilibrium charge is determined by (Spitzer 1978)

$$n_e \left(\frac{8kT_g}{\pi m_e}\right)^{1/2} \sigma_g \left(1 + \frac{eU}{kT_g}\right) = \int_{\nu_o}^{\nu_H} \sigma_g Y \frac{F_\nu}{\langle h\nu \rangle} d\nu$$

where σ_g is the geometrical cross section of the grains, U is their electric potential, ν_o is the threshold frequency at which photons can just overcome the work function taken to be 10 ev, and ν_H is the frequency of the Lyman limit. The heating rate due to photoelectron ejection is given by

$$\Gamma_{PE} = \langle n_d \sigma_d \rangle \, h n_H Y \frac{F_\nu}{\langle h\nu \rangle} \left(\nu_H - \nu_U\right)^2$$

where $n_H = n(H)+2n(H_2)$ and ν_U is the cutoff frequency due to grain charge. For a B0 star 10^{18} cm away from the HII region boundary, the heating rate is $\Gamma_{PE} = 1.0 \times 10^{-20}$ erg cm^{-3} at the edge of the molecular cloud of density $n = 10^3$ cm^{-3}. Deep inside the cloud the pho-

toelectric heating rate drops exponentially due to the extinction of stellar flux.

E. The Boundary Layer Energetics Model

In order to evaluate the significance of photoelectric heating in the boundary layer, the abundance as well as the column density of the observed species (e.g. CO) in the heated layer must be computed. A simple numerical model of the energetics of the boundary layer gas has been constructed in order to investigate the importance of the photoelectric effect in producing hot molecular gas. The radiation responsible for photoejecting electrons can dissociate the molecular constituents of the cloud, strongly depleting species such as CO which is both an important cooling agent as well as the most readily observed probe of the temperatrue structure. A simple chemical scheme is used to calculate the relative abundance of C, C+, and CO at various points in the molecular cloud (Figure 43 and Table 10). In this scheme, CO is destroyed by charge exchange with He+ or by photodestruction. CO is made in turn by a series of reactions whose rate depends on the abundance of molecular hydrogen; these are sumarized by a single equivalent reaction in which H_2 reacts with C+ to generate CO. To complete the cycle involving carbon, electronic recombination of C+ is included.

In order to determine the chemical state of this system, the density of H_2, the electron abundance n_e, and the abundance of ionized helium must be known. Helium can not be photoionized outside an HII

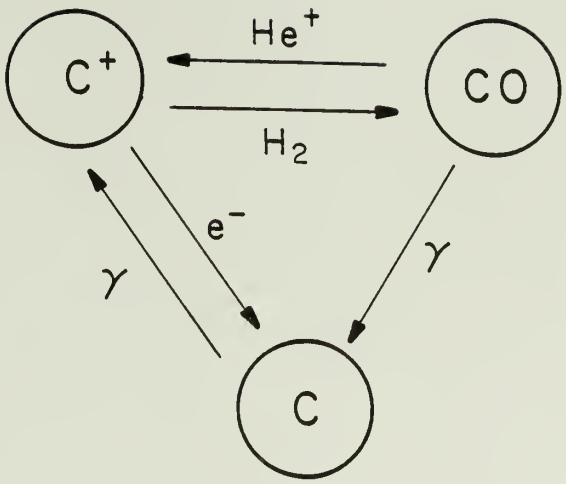

Figure 43

Schematic diagram showing the reactions used to compute the CO abundance in a molecular cloud boudary layer.

TABLE 10

EQUATIONS USED TO COMPUTE THE CO ABUNDANCE IN THE BOUNDARY LAYER GAS

CHEMISTRY

1) $\partial[CO]/\partial t = k_1[C+][H_2] - k_2[CO][He+] - k_3[CO]$

2) $\partial[C+]/\partial t = k_2[CO][He+] + k_4[C] - k_1[C+][H_2] - k_5[C+][n_e^-]$

3) $\partial[C]/\partial t = k_3[CO] + k_5[C+][n_e^-] - k_4[C]$

4) $\partial[He+]/\partial t = k_6[He] - k_7[He+][n_e^-] - k_2[He+][CO]$

5) $[CO] + [C+] + [C] = 2x10^{-4}([H] + 2[H_2])$

6) $[n_e^-] = [C+] + [He+]$

7) $[He] + [He+] = 0.1([H] + 2[H_2])$

$k_1 = 2.0x10^{-16}$

$k_2 = 1.6x10^{-9}$

$k_3 = 5.0x10^{-12}(1.125x10^4/r_{18}^2) \exp(-3.0\ A_V)$

$k_4 = 1.3x10^{-10}(1.125x10^4/r_{18}^2) \exp(-2.4\ A_V)$

$k_5 = 4.4x10^{-12}(T/300)^{-0.61}$

$k_6 = 6.5x10^{-18}$

$k_7 = 4.5x10^{-12}(T/300)^{-0.67}$

TABLE 11

HEATING AND COOLING FUNCTIONS

		HEATING	
1)	Cosmic rays	$\Gamma_{CR} = 6.4\times10^{-28}\ n_p$	1
2)	Warm dust	$\Gamma_{dust} = 2.4\times10^{-33}\ n_p^2(T_d - T_g)\sqrt{T_g}$	2
3)	Photoelectric heating	$\Gamma_{PE} = \langle n\sigma\rangle n_p Y F_\nu h(\nu_H - \nu_o)^2/2\langle h\nu\rangle + C_3((T_d - C_4)\sqrt{T_g} + C_4 T_d/\sqrt{T} - T^{1.5})$ $C_3 = 1.5\langle n\sigma\rangle k n_e n_p (8kT_g/\pi m_e)$ $C_4 = \pi eU/4k$	
		COOLING	
1)	C+ cooling	$\Lambda_{C+} = 7.9\times10^{-27} n_p n_{C+} \exp(-92/T) + (7.9\times10^{-20}/\sqrt{T}) n_e n_{C+} \exp(-92/T)$	4
2)	Si cooling	$\Lambda_{Si} = (1.9\times10^{-18}/\sqrt{T}) n_e n_{Si} \exp(-413/T) + (7.4\times10^{-23}) n_p n_{Si} \exp(-413/T)$	4
3)	Iron cooling	$\Lambda_{Fe} = ((1.1\times10^{-18}/\sqrt{T}) n_e n_{Fe} + 1.1\times10^{-22} n_p n_{Fe}) \exp(-554/T) + 1.35 \exp(-961/T))$	4
4)	H_2 cooling	$\Lambda_{H_2} = 6.0\times10^{-27} n_p n_{H_2} \exp(-509/T)$	3
5)	Molecular (CO) cooling	$\Lambda_{CO} = 6.0\times10^{-27} n_{H_2} n_{CO}\ T^{1.2}$ if $n_{H_2} n_{CO} < 100$ $\Lambda_{CO} = 3.7\times10^{-27}\ T^{3.1}$ if $n_{H_2} n_{CO} > 100$	5

References: 1) Rate corresponds to a primary ionization rate $\xi = 10^{-17}$ cm^{-3} s^{-1}. 2) Glassgold and Langer (1974) 3) Spitzer (1978) 4) Dalgarno and McCray (1972) 5) Goldsmith and Langer (1978)

region since it has a larger ionization potential than hydrogen; thus He+ is formed by cosmic ray ionization and destroyed by electron recombination. The electron abundance is determined by the ionization equilibrium of the most abundant low ionization potential metals. Since carbon is believed to fill this role, the degree of ionization of this species is calcualted at each point in the cloud; the abundance of C+ then effectively determines the electron density. Molecular hydrogen is formed on grain surfaces and destroyed by UV photons in the band 912 A° to 1050 A° (deJong 1980). Dissociation occurs via the Lyman and Werner bands which can saturate at hydrogen column densities of order 10^{14} cm^{-2}, making H_2 self-shielding. The H_2 abundance is calculated in the boundary layer of a molecular cloud with the algorithm presented by deJong (1980) which takes into account the self-shielding of the dissociative transitions as well as the dust opacity.

The rate at which the UV radiation field is attenuated in traversing the boundary layer is computed from

$$F(r) = (F_o/r^2)\ e^{-3.0\alpha N_{tot}(r)}$$

where F_o is the radiation field at the outer boundary of the HII region (it is assumed that the HII region is devoid of dust so that only geometrical factors dilute the radiation field inside), α is the column density of protons giving rise to 1 mag of visual extinction (Bohlin 1975), N_{tot} is the column density of protons between the HII region boundary and the point in question, r is measured from the

star. The factor of 3.0 in the exponent includes the combined effects of absorption and scattering. Although the absorption at 1,000 A° is probably 5 to 6 times what it is in the visual V band, high grain albedos (Flannery et al. 1980) cause multiple scattering of the photons before absorption, permitting deeper penetration of the radiation field into the cloud than might otherwise be expected on the basis of the extinction curve alone.

In addition to the UV continuum, a large amount of energy can be transfered out from the HII region in the Lyman α line of atomic hydrogen. For every ionizing photon emitted by the star, a Lyman α photon, that eventually leaves the HII region, is generated during recombination. Just outside the Stromgren radius, where most of the gas is atomic, the mean free path of an Lα photon becomes very short ($\lambda < 10^{15}$ cm for $n = 10^3$ cm^{-3}). Resonant scattering will result in a random walk transport of the Lα photons into the neutral gas. The effective path length traversed by any particular photon is considerably greater than the line of sight distance; dust attenuates the Lα radiation field within a distance of $30\lambda < 3x10^{16}$ cm (at $n= 10^3$ cm^{-3}) corresponding a hydrogen column density of only $3x10^{19}$. These photons may be an important energy source for the atomic portion of the boundary layer, but do not penetrate far enough to effect the the molecular part and so will be ignored in this calculation.

For the results presented to illustrate the model, a B0 spectral type star is assumed to excite a spherically symmetric HII region

10^{18}cm in radius. At the HII region boundary, the radiation field, evaluated from the model atmospheres of Kurutz (1979), has a strength $F_o = 4.5x10^{-15}(r/10^{18}cm)^{-2}$ erg cm^{-2} s^{-1} Hz^{-1} at λ = 1000 Å which is about 10^4 times stronger than the UV field at a typical location in the ISM (Habing 1968, Black and Dalgarno 1977).

The balance between heating and cooling must be treated simultaneously with the chemistry since the gas temperature and the relative abundance of various coolants such as C+ and CO are coupled. The heating and cooling mechanisms included in the model are sumarized in table 11. Cosmic ray ionization provides input that gives reasonable temperatures in well shielded portions of the cloud. The heating resulting from gas-dust coupling assumes the maximum limit given by equation (3) and (4) and becomes important for high densities. The photoelectric heating rate is given by equation (5) above augmented by an extra term that takes into account the increase in gas-dust coupling due to the increase in the cross section experienced by ions colliding with charged grains.

In the molecular portion of the boundary layer, cooling by molecular rotational transitions, especially those of CO are dominant (Goldsmith and Langer 1978). Two functional forms are used for the CO cooling terms given in table 11. The first form, applicable for $n_{CO}n_H < 100$ cm^{-6} corresponds to the situation where the cooling transitions are optically thin; the second form, used when $n_{CO}n_H > 100$ cm^{-6}, applies when the cooling transitions are thick and thermalized.

Cooling by fine structure transitions of metals, especially C+, can be important in the UV rich portion of the boundary layer. In regions where the temperature exceeds 100°K, cooling by Si+, Fe+, and H_2 becomes important (Dalgarno and McCray 1972). Cooling functions for the fine structure transitions in metals contain two terms; the first represents electron impact excitation and depends on the electron density, the second is due to neutral impact excitation, depending on the number of neutrals $n = n_H + n_{H_2}$.

Models are constructed by specifying the molecular cloud density, and the HII region parameters, including the flux of UV photons emitted by the central star beyond the Lyman edge. The time dependent chemical equilibrium equations given in Table 10 along with the thermal balance rate equation

$$dT/dt = (2/3)(\sum\Gamma - \sum\Lambda) \; / \; n_p k$$

are evolved forward in time from a set of specified initial conditions using the Gear method. For the calculations presented here, the HII region parameters are held fixed so that hydrodynamic effects such as the expansion of the ionized gas and the presence of shock waves in the boundary layer are not accounted for.

Figure 44 shows a thermal model of the boundary layer neutral gas surrounding a spherical HII region whose properties roughly match the observed parameters of S87. The molecular cloud is chosen to have a uniform proton density of $n_H = 10^4$ cm^{-3}. The HII region boundary is

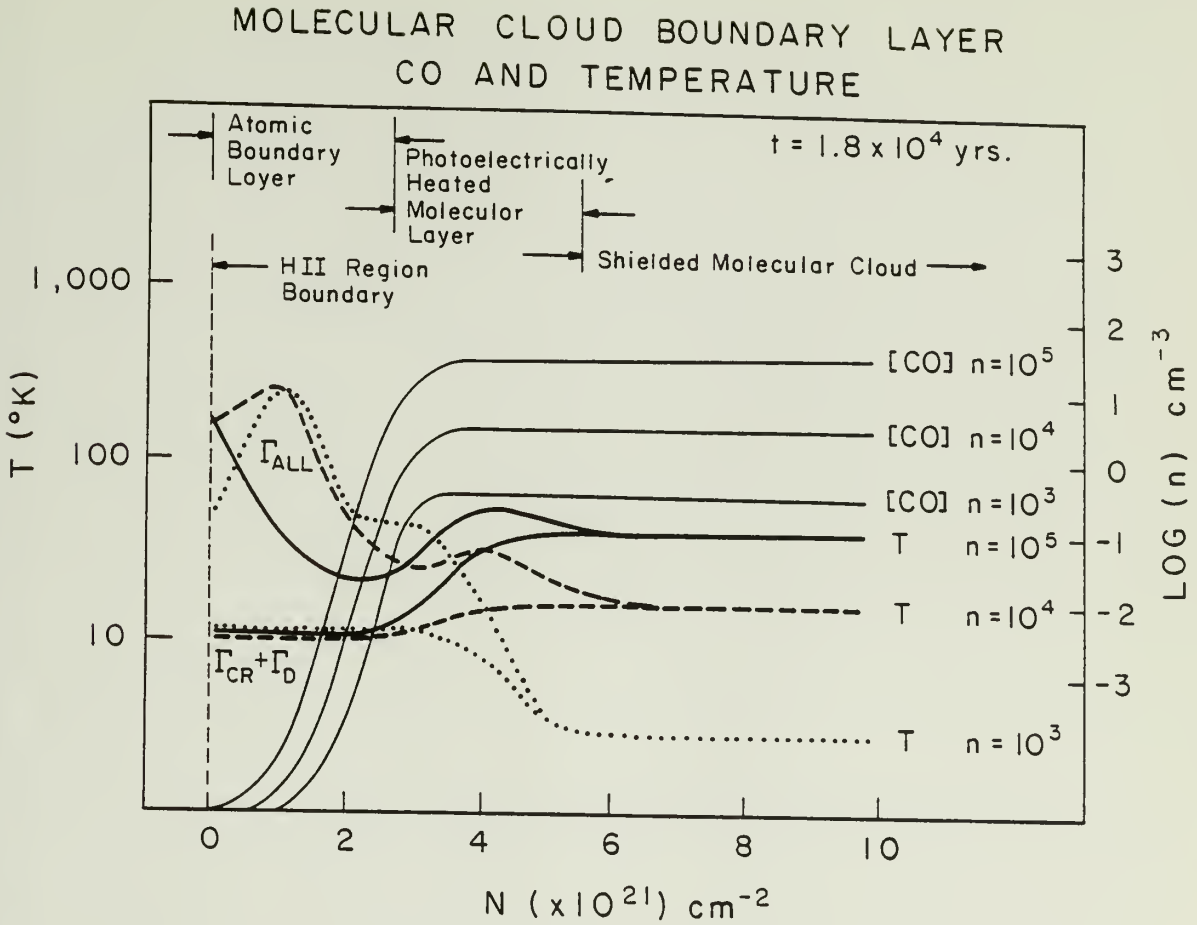

Figure 44

The molecular cloud boundary layer heating model computed for a B0 star emittin 10^{48} photons s^{-1}. Three sets of curves are shown, each corresponding to a molecular cloud proton density of 10^3, 10^4, or 10^5. The CO abundance and temperature, T, are shown. For the curves labeled $\Gamma_{CR} + \Gamma_D$, only cosmic ray and dust heating are included. The curve labeled Γ_{ALL} includes photoelectric heating.

located 10^{18} cm from the B0 exciting star which generates a radiation field 10^4 stronger than the Habing field at the ionization front. The H_2 and CO abundances become large at a distance of 1.3×10^{18} cm from the star, a point at which the dust associated with a column density of 3×10^{21} protons has attenuated the radiation field to about 10 times the standard interstellar value. Three separate temperature profiles are shown; T_{CR} is the gas temperature if only cosmic rays are allowed to heat the cloud, $T_{CR+dust}$ includes heating by warm dust, and T_{all} contains the photoelectric effect. In this model a peak temperature of 300°K is reached in the atomic boundary layer at roughly 1.1 pc from the star.

The time dependent calculations were checked for accuracy by letting them evolve until a steady state was reached. These results were then checked by solving the equations in the steady state by an iterative method. The steady state reached by time evolution of the equations agrees to beter than one percent with the direct steady state computations.

F. Detectability of Photoelectrically Heated CO

The photoelectrically heated molecular boundary layer has a thickness corresponding to a column density of about 10^{21} protons. The extent to which this layer contributes to an observable CO profile depends on the line optical depth which is given by

$$\tau_{CO} = 1.93 \times 10^{-19} \frac{N_H}{T_R \Delta V} \{ 1 - \exp(- \frac{5.5}{T_{1-0}}) \}$$

where the line width is to be given in km s^{-1}. Under the assumption that the excitation and rotation temperatures are the same ($T_R = T_{1-0} = T_{gas}$) and using a value typical of the photoelectrically heated molecular boundary layer as indicated in Figure 44, namely $T_{gas} = 30°K$, a column density $N(H) = 2 \times 10^{21}$ cm^{-2}, and a linewidth $\Delta V = 2$ km s^{-1} the optical depth is

$$\tau_{CO} = 1.07 \left(\frac{N(H)}{2 \times 10^{21} \text{ cm}^{-2}}\right)\left(\frac{\Delta V}{2 \text{ km s}^{-1}}\right) \left(\frac{T}{30°K}\right)\left(\frac{\xi}{0.167}\right)$$

where ξ is the term in brackets in the previous equation, evaluated for T=30°K. The observed CO line peak temperature in this layer is

$$T_A = T_{1-0} \left(1 - e^{-\tau} \right)$$

which gives $T_A = 19°K$ for the example treated. For $T_g = 40°K$, $T_{1-0} = 18°K$.

The above argument assumes that the viewing geometry places the observer in a direction orthogonal to the heated slab, yielding a minimum column density. A more likely location of the observer would place him 60° from the slab normal in which case the observed column densitiy increases by a factor of 2 due to projection effects. For

$T_g = 40°K$ this results in $\tau_{1-0} = 1.2$ and $T_A = 27°K$, in close agreement with the peak line temperatures seen in S87, S125, and S155.

The relatively low optical depth of the photoelectrically heated layer implies that it appears hotter when seen edge on. This suggests that the hottest gas may be seen near the projected edge of the HII region. It is interesting to note that this is precisely the situation in S125 and S106, the two complexes in which the ionized gas is well resolved and localized. The three highest temperature peaks in the North American and Pelican nebulae are also found at the projected edge of the HII region where the photoelectrically heated slab is probably oriented in the line of sight, presenting a large optical depth.

C H A P T E R IV

THE DYNAMICS OF THE INTERACTION BETWEEN HII REGIONS AND CLOUDS

When a massive star is born, the dissociation and subsequent ionization of the surrounding neutral gas by Lyman continuum radiation creates a hot ($T(H_{II}) \simeq 10^4$ °K), high pressure bubble within an otherwise cool ($T(H_2) \simeq 10 - 100$ °K) molecular cloud. The pressure rises in the HII region by a factor $P(H_{II})/P(H_2) \sim 4T(H_{II})/T(H_2) = 2\times10^2$ to 4×10^3. This pressure imbalance is the dominant factor influencing the dynamics of the interstellar medium in the vicinity of recent massive star formation activity. The resulting flow patterns can be strongly influenced by the geometry of the initial density distribution of neutral gas surrounding the growing nebula.

The observed morphology and dynamics of the gas in two of the youngest HII regions studied here, S87 and S106, indicate that even in the early stages of evolution, the Stromgren sphere approximation is not an appropriate description. Both regions exhibit biconical structure in the ionized gas indicating that the equatorial plane may be shielded by dust, possibly in a circumstellar disk. Dense neutral material close to the exciting star could be a source of freshly ionized gas feeding the outflow of the HII region; the injected gas effectively competes for Lyman continuum photons that would otherwise ionize gas near the outer Stromgren radius. The influx of this material can limit the growth of the HII region and alter the evolu-

tion of the nebula from what is predicted by spherically symmetric models.

The CO observations of older HII regions S117, S125, S184, and S155 show fragmentation of the molecular cloud at the periphery of these regions. The expanding shell detected in the molecular gas around S117 clearly indicates that the evolving HII region has burst the molecular cloud leaving much of the gas in a swept-up post-shock layer. Models for these older HII regions must consider the large density variations encountered by the growing nebula as the ionized cavity reaches the cloud surface. Depressurization of the nebula and the ablation of freshly ionized gas from the molecular cloud can result in an organized streaming of the plasma.

In this chapter, the development of HII regions in the above two situations will be considered. In the first case, the exciting star is buried in the center of a disk of dense gas; a configuration that may be common in the early stages of HII region evolution. In the second case, the developing Stromgren sphere is allowed to burst through the cloud boundary into the intercloud medium as is observed to occur in several older regions.

A. HII Regions Containing Disks

1. Inintial Conditions

Many molecular clouds contain reflection nebulae and HII regions having biconical structure, possibly due to the existence of

disks surrounding newly formed stars (Calvet and Cohen 1978). The young stars in LkHα 208, S106, and S87 are highly reddened; they appear to be surrounded by very opaque material lying in the line of sight that permits the escape of radiation preferentially along the axis of the nebulae. When this axis lies in the plane of the sky, the illumination pattern exhibits a two lobed structure, giving rise to observable biconical nebulae (Kandel and Sibille 1978). The mm observations of the nearest biconical HII region S106 show the presence of a ridge of dense molecular gas in the direction orthogonal to the biconical symmetry axis. This ridge may be a large scale extension of the disk responsible for the biconical structure of the ionized gas.

A disk configuration is a natural consequence of the conservation of angular momentum in a dissipative, collapsing system (Black and Bodenheimer 1975, Bodenheimer and Black 1978, Woodward 1978). Numerous molecular clouds exhibit velocity gradients in mm-wavelength emission lines suggestive of overall rotation (Field 1978). If such a cloud is unstable to gravitational collapse, it will settle into the disk configuration within a few collapse times. Transport of angular momentum in the disk by viscous forces is likely to be slower than the initial collapse, so the disk is quasi-stable. A massive star born at the center of such a system will find itself surrounded by matter flattened into the equatorial plane. Magnetic fields can also lead to the formation of flattened matter distributions. A cloud containing a plane parallel field will tend to collapse preferentially along the

field lines since ions and electrons in the gas resist streaming across field lines. A disk structure supported by magnetic pressure rather than rotation results.

As an idealized initial configuration, a disk of uniform proton density n_d is assumed to be buried in a molecular cloud of uniform density n_o such that $n_d >> n_o$. A massive star emitting a Lyman continuum flux of Q photons s^{-1} is assumed to turn-on at the disk center. In this section, we present a simple, semi-quantitative discussion of the evolution of disk constrained HII regions; a more elaborate hydrodynamical treatment will be undertaken in the near future.

An HII region containing a disk is similar in some respects to nebulae containing other kinds of internal neutral gas. The dynamics of bright rims and elephant trunks has been addressed by Pottasch (1958) who shows that the observed ionized gas density profiles can be understood in terms of divergent flow of recently ionized plasma from the neutral region. Dyson (1968) has constructed models of spherical globules immersed in an HII region, showing that ablated gas can resupply the expanding HII region with plasma, keeping it at a high electron density. Compression of the globule by the high pressure ionized gas can lead to very dense neutral gas concentrations ($n > 10^6$ cm^{-3}) and possible gravitational collapse.

To illustrate some of the differences between normal Stromgren spheres and HII regions containing disks, the ionization structure that develops under the assumption of instantaneous stellar turn on is

discussed first. More stable, "quasi-static" configurations are mentioned afterward. The essential points that emerge in the discussion are: 1) Disks can lead to biconical HII regions. 2) Ionization of matter close to the star can result in the development of high densities and large density gradients which fall off with distance from the star. Supersonic outflow can develop in response to pressure gradients, which at a sufficient density, can trap the ionization front close to the star.

2. Initial Ionization and the Retreat of Ionization Fronts

The disk is assumed to be very thin so that most of the Lyman continuum flux of the star is used in ionizing the molecular cloud, resulting in the rapid outward propagation of an R-type ionization front until the initial Stromgren radius given by

$$R_o = (3Q/4\pi\alpha_B\, n_o^2)^{1/3}$$

in the molecular cloud is reached. Photons emitted in the equatorial direction defined by the disk plane will generate an R-type front that propagates into the much denser medium of the disk and eventually reaches a Stromgren radius given by

$$R_d = (3Q/4\pi\alpha_B\, n_d^2)^{1/3}$$

Initial ionization is complete in roughly a recombination time scale

$$\tau = (\alpha_B n_o)^{-1} = 120\ [n_o / 10^3\ cm^{-3}] \quad yrs$$

From this time on the system evolves in a fundamentally different way than the uniform density Stromgren sphere model. In a Stromgren sphere, newly ionized gas streams into the HII region at the ionization front located at a distance R_o from the star. In the disk case, two new sources of gas are available to supply plasma to the ionized cavity. Gas can be ablated and ionized from the inner disk edge at R_d by direct illumination from the star, and gas can be ablated from the disk face by the diffuse radiation field emitted in the nebula as a consequence of recombinations to the ground state. These two sources of gas effectively prevent any ionizing photons from reaching the outer I-front at R_o established during initial ionization since the mean density of the ionized gas has increased. As gas recombines in the outer regions of the nebula, the I front becomes a recombination front moving back into the Stromgren cavity.

In the following discussion, the gas contributed by the ionization front being driven into the disk by direct illumination is ignored. This is a good approximation since the disk is assumed thin and the total number of photons directly intercepted by it will be a small fraction of Q. Furthermore, dust absorption within a real disk will be large in the plane and is likely to compete for UV photons.

The total production rate for diffuse photons in the initially ionized cavity of uniform density is

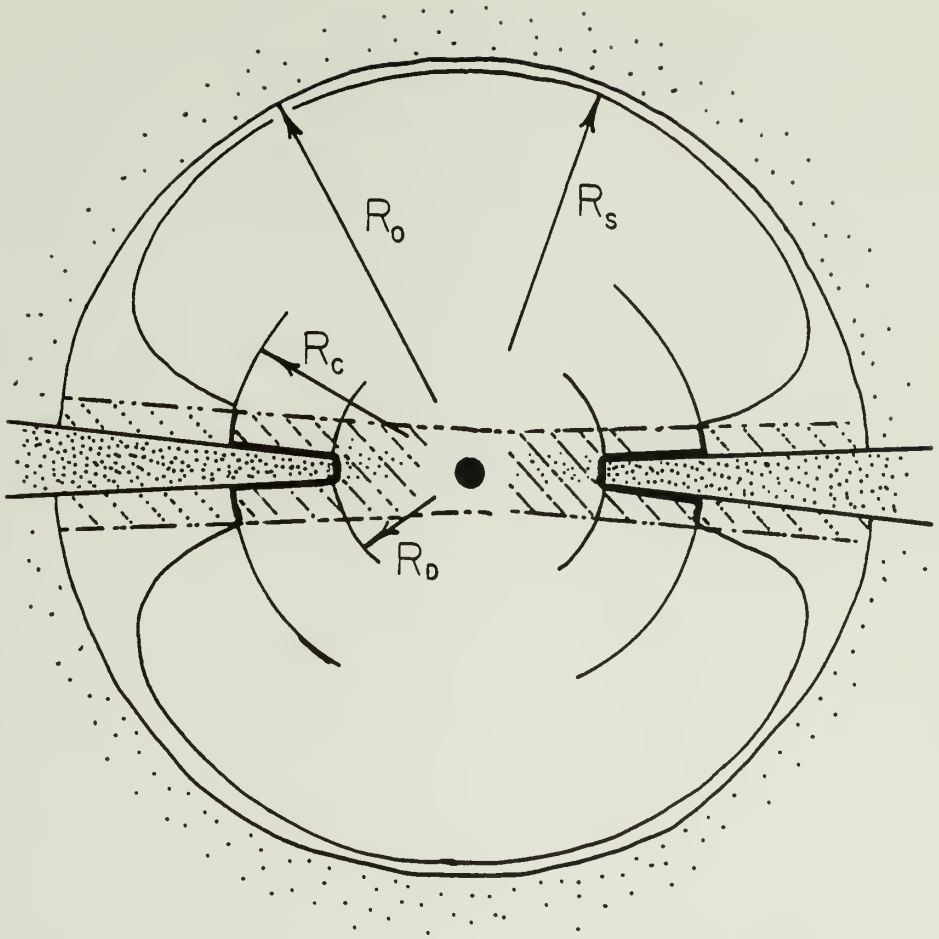

Figure 45

Schematic diagram of a disk constrained HII region. The hatched region is the high density corona rising from the disk. Various symbols used in the text are indicated. R_D = Disk Stromgren Radius , R_C = Coronal Stromgren Radius, R_o = Initial Stromgren Radius , R_s = the equilibrium position of the ionization front.

$$Q_d = (4\pi/3)R_o^3 \, n_e n_p \alpha_1$$

where α_1 is the recombination rate directly into the 1^2S ground state of hydrogen ($\alpha_1 = 1.58\text{x}10^{-13}$ cm^{-3} s^{-1} for $T_{II} = 10^4$ °K). In terms of the recombination rate to all other levels $\alpha_B = 2.60\text{x}10^{-13}$ cm^{-3} s^{-1}, the diffuse radiation field contains

$$Q_d = \left(\frac{\alpha_1}{\alpha_1 + \alpha_B}\right) Q = \gamma Q = 0.378\ Q$$

photons per second. The "on the spot" approximation generally used in treating the diffuse radiation field in Stromgren spheres cannot be used here. Since the mean free path of ionizing photons is only slightly less than the Stromgren radius, photons emitted in the direction of the disk have a high probability of encountering it before causing an ionization in the HII region. These secondary photons shine on the two faces of the disk causing ionization of neutral material. The average ionizing radiation flux incident on the disk face, assuming a spherical HII region, is

$$F_d \simeq \frac{Q_d}{A(HII)} = \frac{\gamma\ Q}{4\pi R_o^2 + 2\pi r_d^2} \simeq \frac{Q}{18\pi R_o^2}$$

for a disk radius $r_d = R_o$ where A(HII) is the total surface area of all the ionization fronts. The density n_c of ionized gas in the coro-

na just above the disk depends on its exhaust velocity V_{ex} from the disk surface. A slab of gas with a sharp density drop will expand in the direction of lower density. Under isothermal conditions, the leading edge expands with a velocity many times the sound speed until it forms a shock where it encounters the lower density gas. The bulk of material, however, is accelerated to near the sound speed (Landau and Lifshitz 1959). Since the disk density is much greater than the initial density of the HII region, its recently ionized face will behave in a manner similar to this slab. (Compression of the disk will occur as discussed below, until pressure balance between it and the HII region is reached, supporting recently ionized gas.) Although this exhaust velocity depends on both the density and pressure gradient above the disk, under isothermal conditions a good approximation is to let $V_{ex} = C_{II} = 10$ km s^{-1}. With this approximation, the coronal electron density is

$$n_c = \frac{F_d}{V_{ex}} = \frac{\gamma\ Q}{6\pi R_o^2 C_{II}}$$

$$= \frac{(4\pi/3)^{2/3} Q^{1/3} \alpha_B^{2/3} n_e^{4/3}}{18\pi C_{II}}$$

For $n_e = n_o = 10^3$ cm^{-3} and $Q = 10^{48}$ photons s^{-1} the disk corona has a density $n_c = 2 \times 10^4$ cm^{-3}. (If the initial disk density is less than or equal to this coronal density, the diffuse radiation will cause the rapid propagation of an I-front into the disk.)

The high electron density corona rising from the disk can be divided into two zones: 1) An inner zone whose ionization is maintained by direct illumination from the star and 2) the outer zone which is illuminated only by diffuse radiation from recombinations occuring in the nebular gas. The boundary between the two zones occurs at the coronal Stromgren radius

$$R_c = (3Q/4\pi n_c^2 \alpha_T)^{1/3}$$

the distance to which stellar photons can penetrate at the coronal density n_c. Direct stellar illumination generates a large ionized fraction in the inner zone, resulting in a long mean free path for UV photons. Here, the diffuse radiation field can ablate the disk efficiently. The outer zone is illuminated by diffuse photons only. As the initial dense layer of ionized gas forms above the disk, recombinations result in the absorption of ionizing photons. A shielding layer develops, decreasing the ablation rate. All ablation from the disk occurs at radii less than R_c where a shielding layer is prevented from forming by direct illumination of the corona by stellar photons.

The position of the I-front in a two component stratified HII region can be determined from the condition that all stellar Lyman continuum photons are just used up by recombining gas between the star and the front. A plane-parallel layer of coronal gas (density n_c) is assumed to have risen to a height Z above and below the disk face. The position of the I-front as measured from the star is given in terms of the angle θ above the disk plane by

$$R_s = R_c \quad \text{.....} \quad \theta < \theta_{crit}$$

$$R_s = R_o \left\{ 1 - \frac{Z^3}{R_o^3 \sin^3\theta} \left(\frac{n_c^2 - n_o^2}{n_o^2} \right) \right\}^{1/3} \quad \theta > \theta_{crit}$$

with $\theta_{crit} = \sin^{-1}(Z/R_o)$

The shape of the I-front as given by this expression has the hourglass form typifying biconical nebulae.

The front described above retreats rapidly toward the star. As the coronal gas rises above the disk, the higher recombination rate within the denser gas increases the flux of diffuse photons incident on the disk. The simple state of the HII region described above can only persist for 10^3 to 10^4 yrs. Within this time, the scale height of the corona Z will reach a height R_c, preventing ionizing photons from reaching beyond a distance R_c from the star. The ionization structure at this stage has become complicated and a proper analysis would require following the time dependent transfer of ionizing radiation in a complex geometry. The highest electron densities are expected to develop directly over the disk close to its inner edge. This gas streams away from the disk as new material is ionized to replace it. The rapid ionization of the disk by the diffuse radiation field can result in a maximum mass loss rate of

$$dM/dt = 2\pi R_d^2 m_p F_d = Q_d m_p/3 = \gamma Q m_p/3$$

$$= 3\times10^{-3}\left(\frac{Q}{10^{48}\ \text{photons s}^{-1}}\right) M_o\ \text{yr}^{-1}$$

The lifetime of the disk depends on its total initial mass; for the 100 M_o disk observed in S106 even the maximum mass loss rate implies a disk lifetime of at least 3×10^4 yrs. Presumably, the inner part of the disk is destroyed first, allowing the size of the ionized cavity to expand gradually.

An approximate mass loss rate for S106 in its current state of evolution can be estimated if it is assumed that about 10% of the disk corona intercepts UV radiation from the star (This is estimated from the thickness of the high electron density rims seen at the northern edge of the S. lobe relative to the overall HII region diameter). The current ablation rate is then roughly $(1/10)\gamma Q m_H = 8\times10^{-4}\ M_o\ \text{yr}^{-1}$. At this rate, the total mass of the HII region ($\sim 10\ M_o$) can be generated in a few x 10^4 yrs.

3. "Quasi-Static" Configurations

The retreating ionization fronts discussed in the previous section continue to evolve until the inner edge of the disk is surrounded by a dense annulus of plasma which acts as the dominant source of ionized gas for the entire HII region. Ionizing stellar radiation emitted in the direction of the disk cannot propagate far due to absorption in the dense coronal gas. Toward the poles the gas density

is likely to drop, allowing the penetration of the radiation into the lobes of the biconical nebula.

Hydrodynamic models by Bodenheimer et al. (1980) include a simulation of a star buried at the center of a slab, a situation similar to what is being considered here. Although the diffuse radiation field is treated using the "on the spot" approximation, several aspects of their computations provide valuable insight into the nature of the streaming gas. In the region between the inner disk boundary at R_d and the star, plasma can flow radially inward toward the star before being accelerated by pressure forces into the biconical lobes. This calculation shows that both above and below the disk, at distances greater than R_d from the star, the plasma enters a region of nearly spherical outflow. At distances several times R_d, flow velocities up to $V_{ex} = 3C_{II}$ are encountered. The evolution of the region is controlled by the transfer of ionizing radiation through the dense corona, and the resulting ablation rate experienced by the disk. Since considerable mass can be tied up in the disk, the evolution of the region can take place over much longer time scales than the sound crossing time for the nebula, hence the term "quasi-static" can be applied to this stage.

4. Approximation of Isothermal Divergent Flow

At a distance greater than the inner coronal radius (as measured from the star) the pressure of the dense gas ablating from

the disk causes the ionized gas flow to diverge. The greatest ablation rate is found at the inner edge of the disk where direct illumination from the star as well as the diffuse radiation field is most intense. Ablation in the outer disk is minimal since direct photons are prevented from reaching this zone by dense intervening plasma. This configurution generates the highest pressures near the HII region center and radially decreasing pressure gradient resulting in the divergence of streamlines. The temperature of the gas is controlled by ionizations, recombinations, and by collisionally excited line radiation of metals. In HII regions, a typical heating or cooling rate is given by $\Gamma \sim 3 \times 10^{-24}\ n_e^2$ erg cm^{-3} s^{-1} (Osterbrock 1974). The cooling due to expansion is characterized by a rate $\Lambda \sim 1 \times 10^{-23}\ (n_e\ /\ \tau_{17})$ erg cm^{-3} s^{-1} where $\tau_{17} = 10^{11}$ sec is the expansion time scale for a sonic flow over a 10^{17} cm region. For electron densities above $n_e \sim 100$ cm^{-3}, the heating and cooling due to ionization, recombination, and line radiation dominate and will hold the temperature fixed close to 10^4 °K hence the flow can be considered isothermal.

The hydrodynamic equations for a spherically divergent isothermal flow can be solved for the density and velocity as a function of position (Landau and Lifshitz 1959) giving

$$\frac{R}{R_c} = \left(\frac{C_{II}}{V}\right)^{1/2} \exp\left(\frac{v^2 - C_{II}^2}{4C_{II}^2}\right)$$

$$\frac{\rho_{II}}{\rho_c} = \exp\left(\frac{C_{II}^2 - v^2}{2C_{II}^2}\right)$$

If at $R = R_c$ the gas is flowing at the sound speed C_{II}, a flow velocity $3 < v/C_{II} < 4$ is reached for $4 < R/R_c < 21$. Once steady state flow is established, highly supersonic expansion velocities are generated in the ionized gas of an internally supplied HII region. The assumption of perfect spherical symmetry can be relaxed since for any divergent isothermal flow the velocity is given in terms of the density change by

$$v = \sqrt{2}\, C_{II} \left(\ln (n_i/n)\right)^{1/2}$$

where n_i is the density at $R = R_i$ and n is the density at which V is being determined.

For a spherical wind with Q_i ionizing photons streaming through an inner boundary at R_i, the position of the I-front at R_s is given by

$$\frac{R_i}{R_s} = 1 - \frac{4\pi Q_i R_i}{\alpha_B}\left(\frac{m_H V_{ex}}{dM/dt}\right)^2$$

where V_{ex} is the wind outflow velocity, assumed to be constant and strictly radial. For mass loss rates $dM/dt < (dM/dt)_{crit}$ where

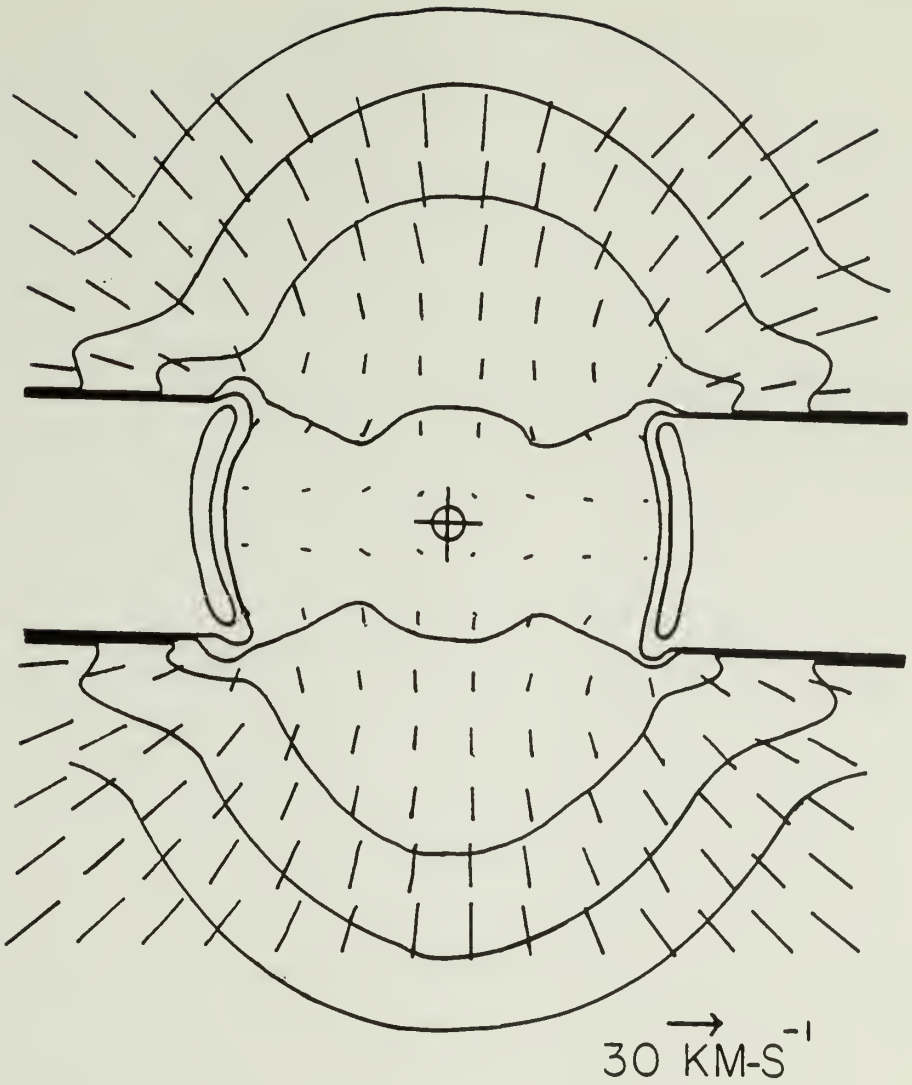

Figure 46

Hydrodynamics of an HII region generated by a star imbedded in a dense slab, taken from Bodenheimer et al. (1979). This calculation treats the diffuse radiation field using the "on the spot" approximation so that the face of the slab remains unilluminated and does not act as a source of plasma. The figure illustrates the quasi-spherical divergence of the flow outside the slab that results from the steep density gradient in the HII region.

$$(dM/dt)_{crit} = m_H V_{ex} \left(4\pi Q_i R_i / \alpha_B \right)^{1/2}$$

$$= 5.8 \times 10^{-6} \left(\frac{Q_i}{10^{48}} \right)^{1/2} \left(\frac{R_i}{10^{15}\,cm} \right)^{1/2} \left(\frac{V_{ex}}{10\,km\ s^{-1}} \right)$$

$$M_o\ yr^{-1}$$

the I-front can move out to infinity, or to a distance where the flow encounters the ambient cloud and a compressed shock can trap the front. On the other hand, for $dM/dt > (dM/dt)_{crit}$, the I-front is trapped close to the inner boundary of the flow at R_i. A recombining outflowing wind with a velocity up to about 4 times larger than the sound speed in the ionized gas results. If more than a few percent of the available flux of ionizing photons is being used to ionize material close to the star and inject it into the HII region at the sound speed, the mass loss rate is greater than the critical value required for trapping of the ionization front. Nontrapping of the I-front in certain directions (such as the poles) can result from strong deviations from spherical geometry, or the destruction of a large part of the the inner disk. A disk with a large inner hole will have less plasma ejected into its polar regions, so ionizing photons will be able to propagate farther than indicated by strict spherical symmetry. A smaller fraction of ionizing photons are intercepted by the disk or the coronal gas directly above it, implying a diminished ablation rate. In S106, the large extent of the HII region ($R_{II} \sim 0.1$-0.2 pc) indicates that the ionization fronts in this nebula are not trapped

within the wind flow from the disk face. The immediate vicinity of the star (at $r < 10^{17}$ cm) may be devoid of neutral material, alowing the escape of photons into the ionized lobes.

5. Gas Flow at the Outer Ionization front

The velocity of expansion of the ionized gas at the outer boundary of a normal Stromgren sphere is

$$v_i = V_i/2 = C_{II}/\sqrt{\beta} \sim C_{II}/2$$

with

$$\beta = 4\rho_I / \rho_{II} - 1$$

Gas flows from the compressed post-shock layer through the ionization front into the HII region. When an internal source of gas supplies the HII region, the number of photons available at the outer I-front is diminished, decreasing the flow of gas through the I-front. Reduction of the influx of newly ionized gas into the HII region at its outer boundary allows faster expansion of the nebula. In the normal Stromgren sphere case, freshly ionized gas generates back-pressure in the HII region that prevents plasma at its outer edge from expanding faster that $v_i \sim C_{II}/2$. As the flux of ionizing photons drops, this back pressure diminishes, allowing v_i to approach C_{II}.

When the expansion velocity of gas at the outer I-front has reached C_{II}, no gas streams across the front and it becomes a contact discontinuity. If mass loss at the disk face is increased further,

the distance to which ionizing photons can penetrate diminishes and the front becomes a recombination boundary. Gas flows from the HII region into a region where it is shielded. When the retreat of the front becomes supersonic, the shock at the terminal point of the flow from the HII region becomes detatched from the I-front. The cooling layer of recombining gas between the two fronts may be detectable in the 21 cm line. This is the situation encountered in an outflowing wind when the I-front is trapped close to the wind source. It is tempting to speculate that the CO hole seen in the S106 map to the north and south of the biconical nebula is filled with recombined gas ejected from the HII region. In this case, the total amount of gas ionized during the lifetime of the nebula may be considerably greater than the currently observed nebular mass.

6. Consequences and Speculations

Observations of the nearby biconical HII region S106 indicate the presence of highly supersonic ionized gas flows. High resolution spectroscopy of the optical emission lines (Maucherat 1975, Deharveng and Maucherat 1978) show that velocity differences up to 70 km s^{-1} are present. In terms of spherical outflow models in which both the approaching and the receeding gas is seen, this velocity difference implies flow velocities between $3C_{II}$ and $4C_{II}$ in the HII region. This flow velocity is readily explained by expansion of isothermal gas generated in a dense region close to the exciting star as is the case in a disk constrained HII region.

Determinations of the electron densities from the intensity ratio of [SII] λ 6717 and λ 6731 yields values as high as n_e = $4x10^4$ cm^{-3} in parts of S106. Both radio maps and photographs taken through narrow bandpass filters centered on emission lines show the highest electron densities lie close to the central star while farther out in the nebula the densities decrease. Such a pattern is consistant with the injection of gas from the disk face close to the star. Radial diminution of the density and the observed high velocities, are the consequence of a disk like distribution of neutral gas.

Ionization and ablation of disk material can generate high velocity, biconically symmetric neutral outflow of gas if the wind densities are sufficient to trap the I-fronts. Trapped I-fronts are likely to be associated with realtively high mass loss rates of order 10^{-3} M_o yr^{-1} . The flow contains mainly recombining hydrogen but some CO and other molecules may also be present. Molecules can either form within the flow if it has sufficient density, or they may be swept up from the adjacent disk or other neutral condensations that may be encountered. High velocity molecular outflows have now been observed in several molecular cloud cores where recent star formation is thought to have taken place. The line wings in Orion (Kwan and Scoville 1976, Zuckerman et al. 1976), GL961 (Blitz 1978), Ceph A (Rodriguez et al. 1980, and this thesis), and GL490 (Lada 1980) extend over a 40 to 80 km s^{-1} range. A dense disk in the immediate vicinity of an early type star can be a source of momentum to power an

outflow with roughly the observed parameters. The high ablation rate from the disk ($\sim 10^{-3}$ M_o yr^{-1}), generated by UV photons, is sufficient to trap the I-front close to the star. The outflow energy is derived from the efficient conversion of thermal energy into radial expansion made possibly by the continual injection of fresh disk material.

The second possible mechanism which warrants further investigastion involves the compression generated by the pinched waist of a biconical nebula. Pressure forces in the constricted waist of a biconical HII region may work to compress neutral gas in the equatorial plane, generating the outer part of the disk. An initial density enhancement giving rise to a biconical nebula can be greatly amplified by the compressive forces resulting from ionization and heating above the symmetry axis. Figure 47 shows the situation in which an initial density distribution generates a negative curvature in the ionization fronts defined by the condition of ionization equilibrium. Gas will be compressed into a plane whenever the I-front has negative curvature since the force vectors will tend to pinch the gas in the equatorial plane. Compression will stop when pressure equilibrium is reached; this occurs when the neutral gas is about 10^3 times the density of the ionized gas causing the compression. For S106 this implies that densities of about 10^6 cm^{-3} can be reached in the disk gas trapped between the two lobes of ionized gas. Hence, the density contrast between cloud and disk assumed in the model seems reasonable and may have been self-generated by the early evolution of the nebula.

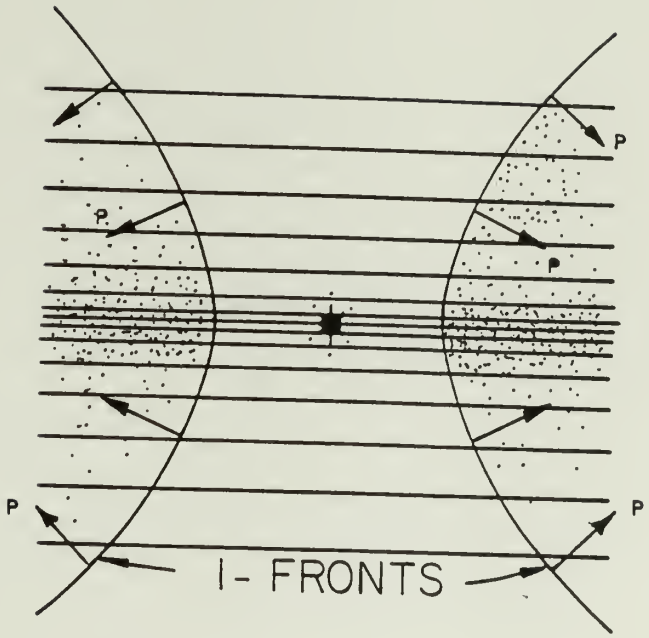

COMPRESSIVE FORCES AT A CONCAVE I-FRONT

Figure 47

Schematic diagram illustrating the pinching effect of the ionized gas pressure when the ionization front is concave. This can result from a steep initial density gradient in the z-direction.

Observations of molecules that probe this density regime are desirable. If several tens of solar masses of gas are effected by the pinch, the compression factor of 10^2 - 10^3 may make the gas gravitationally unstable and cause star or planet formation.

A. The Late Stages of Evolution of an HII Region in an Inhomogeneous Medium

Observations of S125, S117, S184, and S155 show that these older HII region have grown to a size comparable to the molecular clouds in which they were born. In these regions, large areas of nebulosity are visible with little foreground obscuration, indicating that in the direction of the Sun, molecular gas is absent. An HII region born in a high density environment has to evolve through a large density gradient when evolving through the boundary of the parent cloud.

The kinematics of the molecular gas surrounding some of these complexes exhibit outflow from the centroid of the HII region. Evidence of dispersing gas is seen in S125, parts of S184 and S155, but is most spectacular in the case of S117 where an expanding molecular shell is seen. In this section, the evolution of an HII region after it bursts through the surface of its parent molecular cloud is considered.

1. A Model for the Expanding Shell Surrounding S117

A useful constraint on mechanisms which might account for the expanding shell near the Pelican nebula is provided by the total momentum found in the flow. This momentum is

$$P_{obs} = 6 \times 10^{43} \left(\frac{M_{shell}}{6 \times 10^{4}\ M_{o}} \right) \left(\frac{V_{exp}}{5\ km/s} \right) \quad gr\ cm\ s^{-1}$$

Possible sources of this momentum are radiation pressure on dust (Lasker 1966, Mathews 1969), momentum transport by a stellar wind (Castor et al. 1975, Weaver et al. 1978), thermal pressure of the hot HII region (Mathews and O'Dell 1969, Spitzer 1968), and the rocket effect as the expanding shell is ionized and hot gas leaves its back surface (Oort and Spitzer 1955, Kahn 1954).

Supernovae may contribute significantly to the total energy and momentum of the ISM (Woltjer 1972), however, there is no evidence for an SNR associated with W80. The SNR G84.2 - 0.8 (Mathews et al.1977) is located in the direction of the dust lane that separates the North America Nebula from the Pelican but the Σ - D relationship implies that it is at a distance of 7 kpc. Furthermore, it has been shown by Lada et al. (1978) that if a supernova occurs within an HII region, the overall evolution of the region is relatively unaffected by the impulsive input of energy and momentum; the steady input of ionizing photons dominates the dynamics over the age of the nebula.

The momentum transfer from a stellar wind is given by

$$P_{wind} = 2\times10^{42} \left(\frac{dM/dt}{10^{-5}\ M_o yr^{-1}}\right) \left(\frac{V_w}{10^3 km\ s^{-1}}\right) \left(\frac{t}{10^6\ yrs}\right) \frac{\Omega}{4\pi}\ gr\ cm\ s^{-1}$$

where V_w is the wind velocity and Ω is the solid angle of the shell as seen from the exciting stars. Even in the unlikely event that 10 M_o is shed in the wind, the total momentum transfer is still a factor of 10 less than what is observed. Morever the radio f-f maps and the optical emission are centrally peaked rather than cavitated as expected if a wind had been present (Dyson 1973, Castor et al. 1975). Similarily if all of the stellar radiation of the stars contained in the HII region is absorbed by dust in the boundary layer gas (and reradiated by it isotropically), the maximum momentum transfered to the shell by radiation pressure is

$$P_{rad} = 2\times10^{42} \left(\frac{L}{10^6\ L_o}\right) \left(\frac{t}{10^6 yrs}\right) \frac{\Omega}{4\pi}\ gr\ cm\ s^{-1}$$

Finally, we consider the dynamical effects of the hot ionized gas on the surrounding medium. The gas pressure of the HII region exerts a force on the surrounding medium given by

$$F_{gas} = 4\pi\mu_{II}R_{II}^{2}n_{II}kT_{II}$$

where $\mu_{II} = 2.1$ takes account of a 10% helium abundance, R_{II} is the radius of the HII region and T_{II} is its temperature. The proton density is given by

$$n_{II} = n_o\ (R_o\ /\ R_{II})^{3/2}$$

where n_o and R_o are the initial proton density and Stromgren radius of the HII region. The momentum transfered to the surrounding gas is roughly

$$P_{gas} = 3.9\text{x}10^{43}\ \left(\frac{R_{II}}{20\ pc}\right)\left(\frac{n_{II}}{9\ cm^{-3}}\right)\left(\frac{T_{II}}{10^{4}\,^{\circ}K}\right)\left(\frac{t}{10^{6}yrs}\right)\ gr\ cm\ s^{-1}$$

where the current values for the W80 complex are used.

As discussed above, W80 is situated at one extremity of a giant molecular cloud. As the HII region evolved, it burst through the nearest boundary of the molecular cloud, causing depressurization of the ionized region and establishment of a gas flow. This streaming will tend to decrease the ionized gas density between the star and ionization fronts at the HII region cloud interface and thus increase the flux of unused ionizing photons arriving at the front. In this situation, there will be a high rate of removal of gas off the back edge of the cloud and into the ionized region. Such expulsion of material from the neutral shell, selectively in one direction, genera-

tes a driving force, the rocket effet (Oort and Spitzer 1954). An estimate of the rocket force is obtained by assuming that 50% of the stellar photons can be used to dissociate and ionize fresh neutral gas and this gas then flows off of the back of the cloud at 10 km s^{-1}, the speed of sound in the HII region. This maximum rate of momentum transfer from the rocket effect, acting over the 2×10^6 yr lifetime of an HII region is $P_{rocket} = 5 \times 10^{45}$ gr cm s^{-1}. The great potential of this effect to disperse the neutral gas surrounding evolving HII regions is clear.

2. Dynamics of the Molecular Boundary Layer Surrounding HII Regions

Recent work on the relationship between HII regions and molecular clouds indicate that star formation may occur near the surface of molecular clouds (Liszt 1973, Wilson et al. 1974, Blair et al. 1975). Whether the observed HII regions actually formed at the boundary of the original cloud or have simply worked their way to the surface along a path of least resistance (i.e. low column density) is unclear. Nevertheless, as an HII region expands, it eventually reaches a boundary of the molecular cloud where the resulting density asymmetrty of the ambient medium gives rise to depressurization of the ionized bubble and streaming of hot gas away from the cloud surface. The transition from a radially symmetric expanding Stromgren sphere to a streaming surface HII region, density bounded away from the cloud and ionization bounded toward the cloud must be considered in evaluating the effect of the evolving HII region on the boundary layer of the

molecular cloud. It is crucial to follow the depressurization of the HII gas since if the HII region cannot evacuate, the efficiency of the rocket effect is reduced.

A realistic but simplified model for the evolution of an HII region is shown in figure 48. An exciting star emitting Q ionizing photons per second turns on at a distance Δx from the surface of a molecular cloud of uniform density ρ_I. A numerical simulation of the early stages of development of the HII region, including the initial effect of the depressurization of the expanding ionized cavity was conducted by Tenorio-Tagle (1978) and Bodenheimer et al. (1979).

As long as the equilibrium Stromgren radius R_s is less than Δx the evolution of the ionized region initially follows the conventional evolution of a Stromgren sphere. Since star formation seems to occur in high density cores ($n(H_2) \geq 10^4$ cm^{-3}) where the initial value of $R_s \ll 1$ pc, we will assume for the purpose of discussion that initially $R_s < \Delta x$. The theory for the evolution of HII regions in this phase is well developed (e.g. Spitzer 1968), so we cite only the relevant results. During this early period a weak D type ionization front forms, with a shock wave moving ahead, compressing and accelerating the ambient medium. The velocity of the gas in the post shock layer in the frame with the ambient cloud at rest is given by

Figure 48

Schematic evolution of an HII region in a molecular cloud. The W80 complex appears to be in stage (f) which occurs about 3×10^6 yrs after the formation of OB stars.

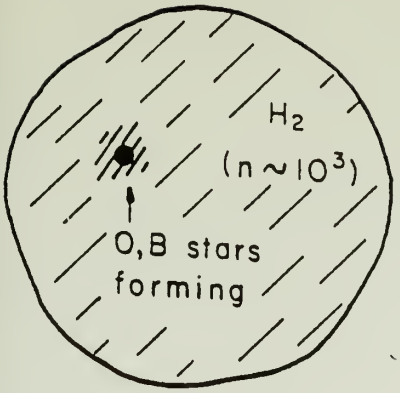
H_2
$(n \sim 10^3)$
O,B stars
forming

(a)

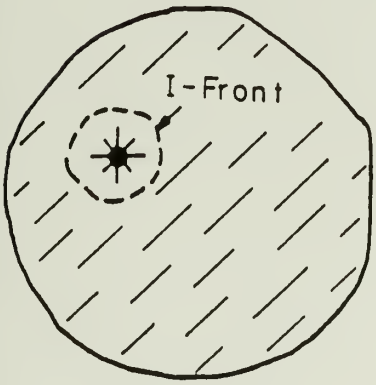
I-Front

(b)

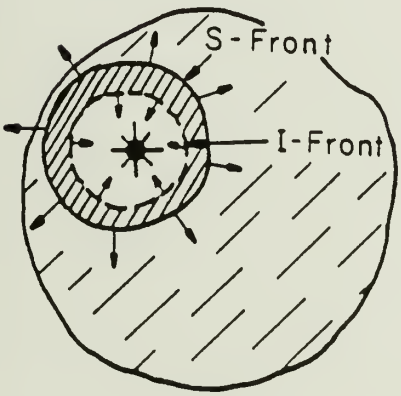
S-Front
I-Front

(c)

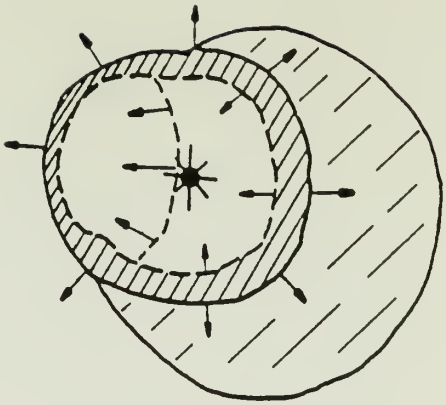

(d)

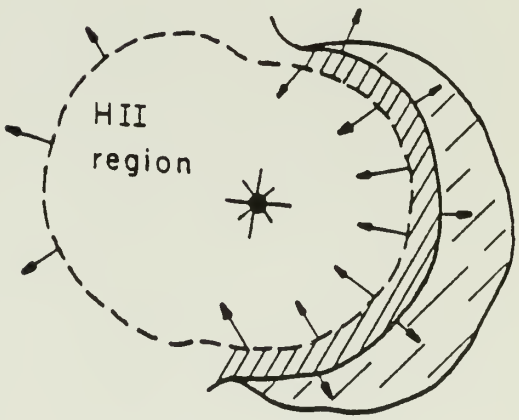
HII
region

(e)

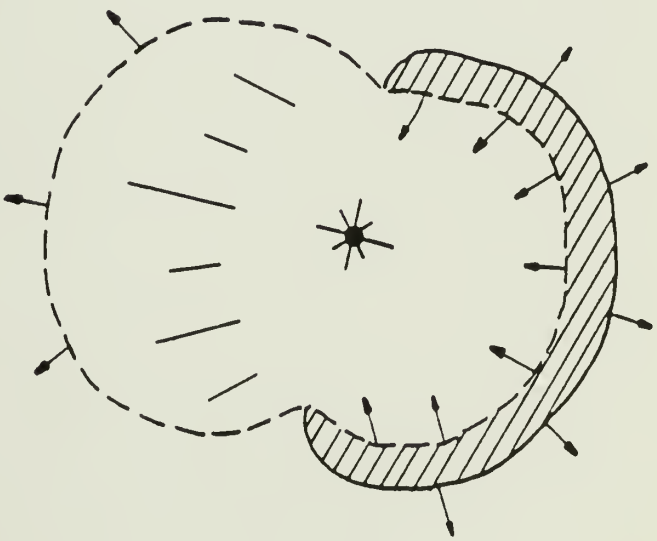

(f)

$$V_2 = V_s \left(1 - \left(\frac{C(H_2)}{V_s}\right)^2 \right)$$

where

$$V_s = C_{II} \left(\frac{R_o}{R}\right)^{3/4}$$

is the shock velocity and C_{II} = 10 km s^{-1}, the sound speed in the ionized gas, $C(H_2)$ = 0.3 km s^{-1} is the sound speed in the molecular gas, R_o is the initial Stromgren radius and R is the radius of the HII region. For the Pelican nebula , the initial Stromgren radius would be 2 pc for an ambient density of 500 cm^{-3} and Q = $5x10^{49}$ s^{-1}. Since the present region radius is 20 pc, the predicted velocities of both the shock front and shocked H_2 gas would be about 1.8 km s^{-1}. It is clear that the Pelican nebula cannot be in this stage of evolution because the observed expansion velocities are substantially larger and the optical appearance shows the HII region is unconstrained by neutral gas over at least half its circumference.

The details of the HII region depressurization as it bursts the surface of the cloud are likely to be complex and dependent on the precise manner of the cloud density fall off at its edge. The great pressure disequilibrium that exists between the intercloud medium (ICM) and the post shock gas will result in the conversion of the

shock into a rarefaction wave that propagates back into the HII region. Ionized gas will stream away from the cloud into the low pressure ICM. Since the rarefaction wave propagates into the HII region at roughly the speed of sound C_{II}, depressurization will be complete in about

$$\tau = \frac{2\Delta x}{C_{II}} = 1.9 \times 10^5 \left(\frac{\Delta x}{\text{pc}}\right) \left(\frac{C_{II}}{10 \text{ km s}^{-1}}\right)^{-1} \text{ yrs}$$

The "nozzle" through which the gas escapes is likely to grow considerably during this period so as to minimize any back-pressure effects. Once the rarefaction wave has entered the region between the exciting star and the ionization front, the decrease in the density of the HII region implies a corresponding increase in the flux of ionizing photons available at the boundary of the HII region. The dynamic character of the evolving HII region changes from a uniformly expanding Stromgren sphere to a state in which the ionized gas constantly streams away from the ionization front, leaving the initial Stromgren cavity through a break into the ICM.

The situation closely resembles the conditions treated by Kahn (1954) and Oort (1954) when they considered the dynamics of cloud acceleration by the rocket effect. The rate at which gas becomes ionized at the I-front (the ablation rate), depends on the available flux of Lyman photons. Since this depends on the density of ionized gas between between the exciting star and the I-front, n_{II}, the abla-

tion rate is self-regulating; a large UV flux increases ablation, resulting in an increase of n_{II} and thus the UV absorption rate. The incident ionizing flux is given by

$$F_{inc} = \frac{Q}{4\pi R^2}\left(1 - \frac{R^3}{R_s^3} \right) = \frac{Q}{4\pi R^2} - \frac{n_{II}^2 \alpha R}{3}$$

where R_s is the Stromgren radius at the present HII region boundary. The flux of protons flowing away from the ionization front at an exhaust velocity V_{ex} ($\cong C_{II}$) is $n_{II}V_{ex}$ and this rate must equal F_{inc}. Therefore

$$n_{II} = - \frac{3V_{ex}}{2\alpha_R} + \left(\left(\frac{3V_{ex}}{2\alpha_R} \right) + \frac{3Q}{4\pi\alpha R^3} \right)^{1/2}$$

For parameters appropriate to the Pelican nebula ($V_{ex} \cong 10$ km s^{-1}) $Q = 5 \times 10^{49}$ s^{-1}, and R = 20 pc, the dominant term is the last and thus

$$n_{II} \cong \left(\frac{3Q}{4\pi\alpha R^3} \right)^{1/2}$$

Since this density is precisely the same as that found for a normal Stromgren sphere ionization bounded all around, we conclude that the puncturing of the HII region does not change the HII region density between the star and the cloud. But since material is constantly lost

to the ICM, the rate of ionization of fresh matter is much greater than before depressurization. After depressurization, the velocity of the flow away from the I-front is roughly $V_{ex} = C_{II}$. This results in a slight increase in the pressure exerted by the HII region on the surrounding neutral cloud. The pressure change is always less than a factor of two.

The shock initially driven by the expanding HII region remains unaltered in structure and follows the same propagation velocity dependence on the radius as in the case of the simple Stromgren sphere. The velocity of propagation of the I-front, however, changes due to the increased ablation rate. The difference between the I-front and the shock front velocities, $\Delta V = V_s - V_i$ is

$$\Delta V_{rocket} = \frac{1}{n_2} \left(n_o V_s - \frac{n_{II} C_{II}}{2} \right)$$

where the exhaust velocity $V_{ex} = C_{II}$ is assumed. For comparison in the case of the Stromgren sphere one finds

$$\Delta V_{Stromgren} \cong \frac{1}{n_2} \left(n_o V_s - \frac{n_{II} V_s}{2} \right)$$

For the regime of interest $V_s < C_{II}$, hence $\Delta V_{rocket} < \Delta V_{Stromgren}$ and the I-front now moves at a velocity closer to the shock velocity.

Eventually the shock front will run through the entire molecular cloud reaching the far side away from the HII region. Looking toward the center of the S117 HII region, we seldom see CO at the rest velocity of the nebula or at a velocity of the bulk of the giant molecular cloud to the southwest. We interpret this as an indication that in the vicinity of the Pelican nebula, the shock has traveled the full line of sight linear extent of the cloud. Once this happens the rocket effect can accelerate the shell according to the equation

$$-\frac{dM}{dt} V_{ex} = M \frac{dV}{dt} V_{shell}$$

Integration yields

$$V_{shell} = C_{II} \ln \left(\frac{M_o}{M} \right) + V_2$$

with M_o being the shell mass at the start of rocket acceleration. Assuming that the velocity of the shell when the shock reaches the backside of the cloud is V_2 = 1 to 2 km s^{-1} as appears reasonable from the foregoing discussion, the shell mass must have decreassed just 35% to account for acceleration to the presently observed 5 km s^{-1} expansion velocity . Since the estimated mass presently found for the Pelican molecular shell is 3 - 6×10^4 M_o, the required total ablation of 2×10^4 M_o is consistant with the mass estimates for the W80 HII region of 1.8×10^4 M_o (Wendeker 1968).

The results of numerical calculations for an evolving HII region and associated neutral gas shell are shown in Figure 49. Calculations were started at the time the HII region reaches its initial Stromgren radius and carried to beyond the present epoch for the Pelican nebula. Three clouds of different initial density are treated. The curves show the time dependence for the shell velocity, the shell mass per unit solid angle as seen from a central star, and dM/dt for the shell. Critical times are noted when the HII region starts to depressurize and when the initial shock reaches the back side of the cloud. The minimum in the gas velocity occurs just as the shock reaches the back side of the cloud.

3. Discussion

The above discusson has implicitly assumed that molecular clouds can be modeled as a uniform density gas with $n(H_2) \sim 500$ cm^{-3} imbedded in an intercloud medium with a much lower density $n_{ICM} \sim 1$ cm^{-3}. The boundary between the ICM and the cloud is taken to be a sharp density discontinuity. Under these conditions, three well defined phases of evolution of an HII region can be identified: 1) The expansion of the Stromgren sphere in a uniform density medium. 2) Depressurization of the Stromgren sphere once the weak ionization front reaches the nearest cloud boundary. At this stage a gas flow is established, evacuating the ionized cavity with a consequent increase in the ablation rate at the I fronts at the HII-H_2 interface. 3) Once the shocks penetrating the H_2 gas reach the far boundary of the cloud,

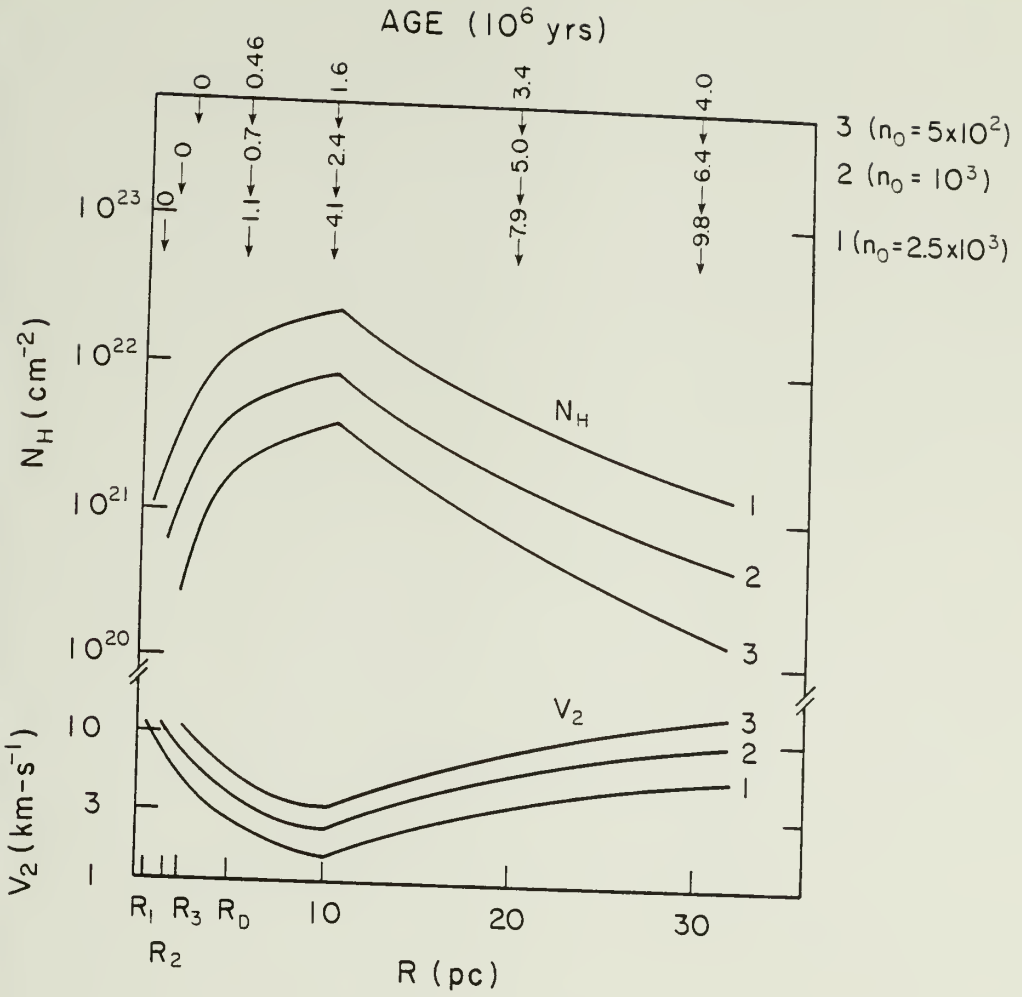

Figure 49

The model calculations of the evolution of the post shock layer showing the column density N_H of hydrogen (assumed to be molecular), and the velocity of this gas V_2 as a function of the radial position of the shock relative to the exciting star. The flux of ionizing photons is taken to be $Q = 5x10^{49}$ photons s^{-1}. The age of the region as a function of shock position is shown at the top. Calculations are for three molecular cloud densities; $n_o = 500$ cm^{-3}, $n_o = 10^3$ cm^{-3}, and $n_o = 2.5x10^3$ cm^{-3}; R_1, R_2, and R_3 correspond to the initial Stromgren radii at the three densities; R_D is the distance from the exciting star at which depressurization occurs.

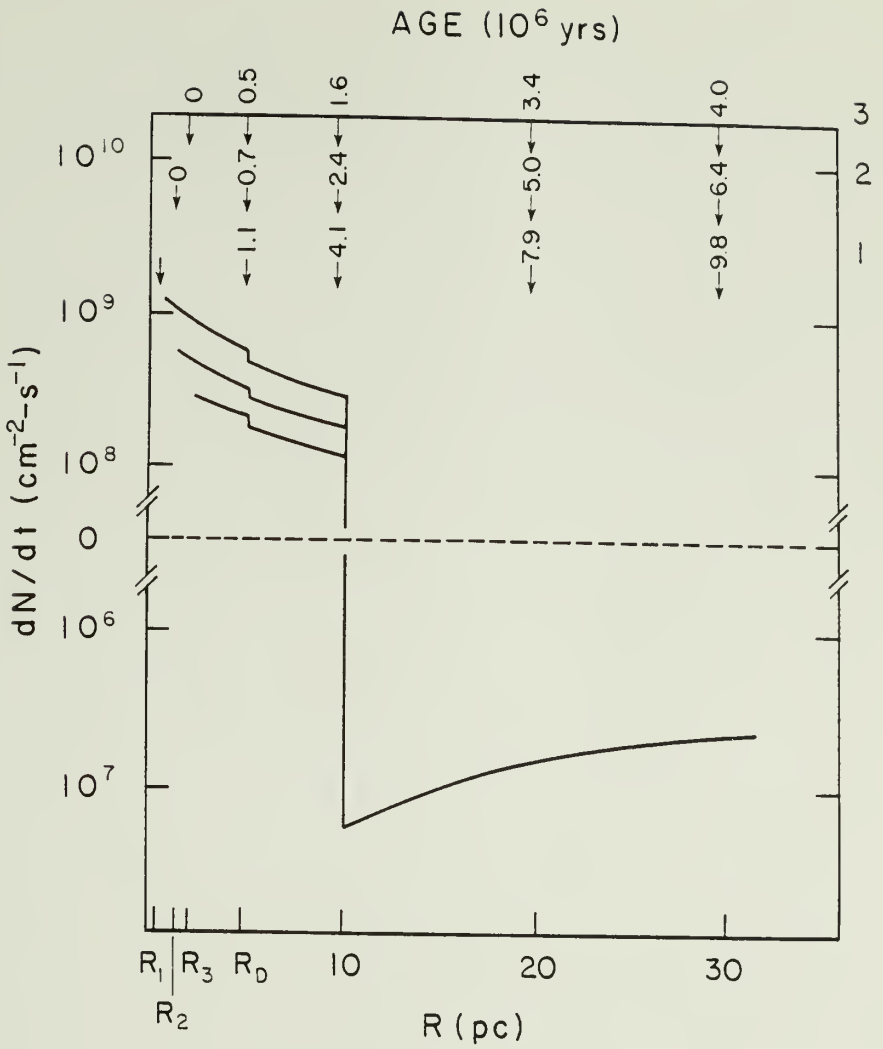

Figure 50

Net mass accumulation rate for the post shock layer, taken to be the difference between accretion at the shock front and ablation at the ionization front.

mass accumulation by the post shock layer ceases. The rocket effect can now take full effect and accelerate the remaining molecular shell. This scenario is illustrated in Figure 50. Even if a weak D-type front has not formed prior to depressurization, the general picture outlined above holds.

In the context of this model, W80 is in the third stage of its evolution. The observed 5 km s^{-1} shock velocity can be obtained only by acceleration of the post shock gas; if the shock were accumulating material from the ambient medium, either a very low ambient cloud density or unrealistically large values of Q would be required. The observations reveal very little ambient undisturbed gas, especially near the Pelican nebula.

The 5 km s^{-1} shock velocity observed could be obtained without invoking the rocket effect if the average H_2 cloud density were $\leq$ 40 cm^{-3}. Unfortunately the density of the original molecular cloud is unobservable; the gas in the molecular shell has been shock compressed and its space density is a poor indicator of the parameters of the original cloud. The column density in the shell, however, does reflect the dynamic history and the initial ambient cloud space density. The observed value of $N(H_2) \cong 8 \times 10^{21}$ cm^{-2} at a distance of 20 pc from the expansion center implies a minimum value for the average space density of $n(H_2) > 120$ cm^{-3}. When allowance is made for the removal of gas from the shell by ablation into the depressurized streaming HII region, this number is increased by at least a factor of

2 since the mass of the ionized gas is comparable to the mass of the molecular shell. If the original molecular cloud was smaller than the current 20 pc radius of the shell, the mean density of the original cloud is increased even more. We thus conclude that the mean ambient space density of the original molecular cloud is constrained by the observed column density N to have a value $n(H_2) \geq 500$ cm^{-3}.

Molecular line observations do not place stringent constraints on the density transition between cloud and the ICM. The cloud boundary may be ill defined with a gradual decrease in the density with increasing distance from the cloud center. In one extreme, the cloud can be modeled with a smoothly varying density law such as a power law

$$n(R) = n_o \left(R/R_o \right)^{-\alpha}$$

The outer extensions of the cloud where the density is much lower than $n \simeq 500$ cm^{-1} would be difficult to observe due to insufficient excitation of observable transitions. Under these conditions, the three evolutionary stages become blurred. An HII region developping in an asymmetric location will begin to develop gas streaming almost immediately. The shock velocity depends on R as

$$V_s = C_{II} \left(\frac{2}{R_o}\right)^{1/2} \left(\frac{3Q}{4\pi\alpha}\right)^{1/4} \left(R_o \right)^{-\alpha/2} R^{(2\alpha-3)/4}$$

for $R >> (R_o - \Delta x)$.

For $\alpha > 1.5$ a weak D type front never develops! For $\alpha < 1.5$ the shock velocity always decreases in time; although the HII region develops with gas streaming, it doesn't depressurize in the earlier sense; the shock never breaks through a cloud boundary. It continually decelerates until its becomes a subsonic disturbance; mass accumulation ultimatley dominates the rocket effect and halts the post-shock layer.

Realistic cloud models probably lie between the two extremes; e.g. possess soft boundaries. Acceleration results when the rocket pressure exceeds the ram pressure of the shock. In applying such an intermediate model to W80 it is not strictly possible to rule out ram pressure confinement of the molecular shell by a low density ($n \simeq 40$ cm^{-3}) layer that is undetectable in ^{12}CO. However, such gas located at over 20 pc from the initial center of expansion of the HII region would require that an extensive low density halo exist around the original cloud; a feature for which there is no observational evidence. Hence in the intermediate "soft boundary" model, the molecular shell appears to be in the accelerating phase.

Extensive low mass star formation has occured within the molecular clouds associated with this complex, as indicated by the presence of a large number of Ae, Be, and T-Tauri stars (Herbig 1958, Cohen and Kuhi 1979). Whether these stars were formed before the birth of the HII region and unveiled by the expansion of the molecular shell, or formed as a consequence of the expanding shock wave asso-

ciated with the shell formation could in principle be decided on the basis of their kinematic behavior. If the stars were formed in an expanding shocked shell, they should posses velocities characteristic of the shell. If they were formed prior to the formation of the HII region, the star velocities should reflect only their random velocities rather than the expansion of the molecular shell. Since the molecular shell has passed beyond the extent of the original molecular cloud, the presence of young stars near its current position would be consistent with the expansion of the stellar system in phase with the shell. There is an obvious concentration of such stars near the Pelican I-front next to the CO hot spot and "bulge". The appearance of these stars on the HII region side of the shell gas is consistent with the recent episode of cloud acceleration by the rocket effect.

The kinematic age of W80 is 3 - 8×10^6 yrs (see Figure 50) while most of the pre-main sequence stars studied by Cohen and Kuhi (1979) are younger than 3×10^6 yrs. Presumably many of these stars were born in the moving shell of molecular gas, indicating that low mass star formation has occured since the formation of the molecular shell.

The Pelican hot spot contains an infrared source IRS4 whose near IR broad band spectrum is shown in Figure 31. This object does not posess a spectrum characterizing it as proto-stellar; the H-J and J-K color indices, when plotted in a color-color diagram (see Snell 1979), indicate a normal star suffering large extinction. The coincidence of position between the peak CO temperature and IRS4 is better

than an arcminute, indicating a probable physical association between the star and the hot spot. The luminosity of this star is too small to heat the grains to 27°K and therefore the indirect process of heating through collisions with warm dust grains is insufficient. This may be yet an other example of a cloud region heated photoelectrically. IRS4 must be later than spectral type B1 or B2 since no f-f emission is reported from its location. If this star formed within the cloud in which it sits, it would provide evidence for the formation of intermediate mass stars. There is no evidence for the occurance of high mass star formation anywhere in the cloud. Evidently OB star formation has ceased in this complex.

The apparent thickness of the shell, determined to be about $\Delta R \simeq 3$ pc, is larger by about an order of magnitude than what is expected from simple isothermal shock theory. From consideration of mass conservation, the fractional shell thickness ought to be

$$\frac{\Delta R}{R} \cong \frac{1}{3} \frac{(n_o - 1/2 n_{II})}{(n_2 - n_o)} \cong 0.1 \text{ pc}$$

Turbulence must play an important role in thickening the post shock layer. In the most quiescent parts of the shell, CO line widths are about 1.5 to 2 km s^{-1}, highly supersonic. If the shell is in its rocket phase and being accelerated , a turbulent cell can drift a distance from the back of the shell characterized by a scale height

$$h = \frac{[\Delta V]^2}{2g}$$

where g is the acceleration experienced by the shell and ΔV is the turbulent velocity dispersion. For the Pelican $g \simeq 2 \times 10^{-9}$ cm s^{-2} giving a value of $h \simeq 3$ pc. Thus the observed shell thickness is consistent with 2 km s^{-1} turbulence and acceleration by the rocket effect.

So far, the effect of gravity has been neglected. The total mass of the W80 complex (sum of the ionized gas mass of M(HII) = 2×10^4 M_o and the molecular shell mass of 6×10^4 M_o) is $M = 8 \times 10^4 M_o$ so at the position of the shell, 20 pc from the nebula center, the escape velocity is about 6 km s^{-1}. Since the shell expansion velocity of 5 km s^{-1} is close to the escape velocity, gravitation may play an important role in the evolution of the W80 complex. Molecular clouds form stars at a rate orders of magnitude slower than the free-fall time; they must be quasi stable against collapse. Neglect of gravity may be partially compensated by neglect of positive pressure forces which prevent rapid gravitational collapse. Gravity opposes the expansion of the HII region, but so long as the ionized gas pressure exceeds the gravitational pressure, expansion will prevail. The mass of W80 gives rise to a gravitational acceleration of about 3×10^{-9} cm s^{-2} at the position of the molecular shell. In order to generate an outward acceleration of 2×10^{-9} gm s^{-2}, the rocket effect must be increased by

a factor of two over what was used in the computations. This can be accomplished by modestly increasing the UV luminosity of the exciting stars inside W80.

4. S125 Kinematics

The molecular cloud surrounding S125 shows evidence of dynamic interaction with the ionized gas. The overall CO distribution exhibits a shell-like structure with a hole at the position of the HII region. Although the systematic velocity field detected around S117 is not seen in this source, the $\Delta V = 2$ km s^{-1} velocity shifts seen in the three cloud fragments comprising shell can be interpreted in terms of expansion away from the HII region. The principal uncertainty in such a model comes from our inability to pinpoint the relative positions of the cloud fragments and the HII region in the line of sight.

The largest positive velocities seen in S125 arise in parts of the cloud lying behind the nebula. The Hα line profile, centered at $V_{lsr} = 4.8$ km s^{-1}(Georgelin et al. 1973) and shifted 3-4 km s^{-1} to the blue relative to the CO velocity, indicates that the ionized gas is streaming away from the molecular cloud toward the observer. The reaction force can push cloud fragment A (see Figure 32) away in the line of sight. Fragments B and C which lie close to the apparent edge of the nebula would posses velocity vectors oriented orthogonal to the line of sight. The expansion velocity of the periphereal clouds in S125 is about 1 km s^{-1}. With the above expansion velocity, the dynamic expansion time for S125 is about 1×10^6 yrs, less than the estimated age for the star cluster of 3×10^6 yrs (Walker 1959).

Gravity, must play an important role in controling the motion of the cloud fragemts since the total mass of the region is about 1.5×10^3 M_o (assuming 600 M_o for the H_2 mass, 700 M_o for the HI mass, and about 200 M_o for the cluster mass). At a distance of 2 pc from the HII region center, the escape velocity is 2.5 km s^{-1} which is comparable to the velocity dispersion of the molecular gas as judged from the line widths. It appears that both the HI cloud and the CO fragments are bound to the complex, while the ionized gas can escape.

5. The S184 and S155 Velocity Fields

In two clouds, S184 and S155, a CO feature shifted to negative velocities with respect to the bulk of the cloud is found to coincide with the position of the highest electron density ionized gas. The blueshifted component can be modeled as a disturbed neutral layer pushed toward the observer by the background HII region. These negative velocity features may be the best known examples of gas that has passed through a shock driven by an expanding ionization front.

The expected velocity and density of such a disturbed layer follows from pressure balance across the ionization-driven shock front that preceeds the layer into the cloud. In terms of the ambient cloud proton density n_o and the electron density in the HII region n_{II} , the disturbed layer has a velocity

$$V_2 \simeq V_s = C_{II}\left(\frac{2n_{II}}{n_o}\right)^{1/2}$$

and a density

$$n_2 = n_o \left(\frac{V_s}{C}\right)^2$$

where the shock is assumed to be isothermal with a sound speed $C \simeq 0.3$ km s^{-1}. The column density of swept up gas between the shock and ionization fronts is roughly $N = n_o R/3$ where R is the total distance traversed by the shock front since it started accumulating mass. This estimate is good so long as $C \ll V_s \ll C_{II}$. Expulsion of gas in an asymmetric HII region can increase the erosion of the post shock layer, decreasing the column density of gas. On the other hand, evolution of the shock through an initially denser cloud core out of which the exciting stars were born, results in a greater accumulated mass. The parameters of the observed velocity shifts in S184 and S155 are within the range expected for a post-shock layer. Since no direct measure of the ambient cloud or post-shock density is available, a detailed comparison with shock models is not possible. The qualitative features of the shifted gas, however, do fit the shock interpretation.

The distribution of the doppler shifted gas correlated well with the distribution of dense plasma. In both S184 and S155 the

greatest velocity shifts arise in front of high electron density concentrations in the HII region, where the foreground extinction is low. At the northern edge of the S155 molecular cloud and at the eastern edge of the S184 cloud, shifts of $\Delta V \simeq 5$ km s^{-1} are seen. The small extinctions amounting to $A_V \simeq 1 - 2$ mag. here indicate a low column density consistant with a small space density required to give a large shock speed. Towards the opaque, presumably denser, regions of the cloud the line shifts are more modest, amounting to only 1 - 2 km s^{-1} in the CO line. In S155, a peak temperature of $T_A = 33$ °K is reached in the shifted component at the position of the highest electron density. Similarily in S184, the hottest temperature of $T_A = 16$ °K is seen in front of the f-f peak at the shifted velocity.

Gas in a moving post shock layer can be detected only if the column density is sufficient to trap the advancing dissociation wave between the ionization front and the shock front. This only occurs after the post shock layer has swept up a column density of several x 10^{21} cm^{-2} protons. Thus shocked gas should be detectable only around the older HII regions (as is observed to be the case). The high velocities encountered in the Pelican and S184 can occur only if the ambient cloud density into which the shock is moving is very low, or the layer has been accelerated (by the rocket effect).

C H A P T E R V

INTERPRETATION AND DISCUSSION

In the preceeding chapters, observations of 6 HII regions and their associated molecular clouds were presented. The energetics of the molecular cloud boundary layer adjacent to an HII region was discussed in Chapter III. The behavior of an HII region developing inside an extended disk of neutral gas, as in S106, and the nature of the expanding shell surrounding S117 were discussed in Chapter IV. In this section, the observations and theoretical interpretations are summerized for all six sources. These results have implications for theories of the evolution and destruction of molecular clouds in our galaxy.

The observations have revealed three kinds of phenomona: (1) The boundary layer molecular gas, in some HII regions, exhibits higher temperatures than can be explained by heating caused by warm dust. This discrepancy may be solved by invoking photoelectric heating of the cloud surface. The photoemitting UV radiation can penetrate the cloud to a sufficient depth to give an observable degree of excitation of the CO molecule. (2) Evidence for a massive circumstellar disk is found in one region (S106). The disk dominates the dynamics and evolution of the ionized gas. (3) In older HII regions, shock fronts are observable as doppler shifted line components. Under some conditions, the rocket effect can accelerate the post-shock layer to the escape velocity from the complex.

A. The Sources

1. S87

This region exhibits many of the signposts usually associated with regions of active star formation. Within the obsevational errors, the compact HII region, IR source, H_2O maser, and molecular peak coincide. The luminosity of the B0 central star exciting the HII region is too small to heat the surrounding dust to a temperature capable of exciting the CO. Since no other sources with sufficient luminosity are observed in the cloud, the gas may be heated photoelectrically. The IR photometry indicates extinction greater than 15 mag in the direction of IRS1 and IRS2 suggesting that the stars as well as the HII region are still buried in the cloud.

2. S106

This nearby biconical HII region exhibits evidence of a large 100 M_o circumstellar molecular disk surrounding a newly formed star and constraining the development of its HII region. The disk is seen in the mm-data as an elongated ridge of molecular emission oriented orthogonal to the axis of symmetry of the HII region. The inner part of the disk is responsible for the biconical optical appearance of the nebula. The relative extinction of the two lobes of ionized gas as well as their velocity fields suggests that the axis of symmetry is tilted so that the southern lobe is closer to the Sun. Two molecular hot spots, one of which contains an H_2O maser are found in the CO

ridge indicating the possible growth of condensations. A model for an HII region developing inside a disk evolves differently from a normal Stromgren sphere. Ablation of gas from the disk results in the formation of a divergent flow or wind which can slow down the expansion of the outer ionization fronts. The density and pressure gradients resulting from the divergence of the isothermal flow can account for the supersonic velocities observed in the optical lines from this source. In denser, more compact disk constrained HII regions, the ionization front may be trapped close to the star, resulting in the formation of massive high velocity neutral flow driven by ionization, acceleration, and subsequent recombination of ablated disk material. The large extent of the S106 HII region suggests that much of the disk close to the star has been dipersed.

3. S117

This is a large, evolved HII region which has an expanding molecular shell surrounding the HII region. The expansion velocity of 5 km s^{-1} coupled with the absence of stationary gas (relative to the HII region) suggests that the shell is the accelerated remnant of a post-shock layer that has been pushed by the HII region by the rocket effect.

4. S125

This is an evolved, low excitation HII region posessing a fragmented molecular cloud. Two of the 3 hot spots possess high CO

temperatures and no known internal energy sources. Significant photoelectric heating of the boundary layer by the cluster radiation field may be occuring. The velocity shifts seen in this cloud may be the result of HII region expansion.

It is interesting to note that S125 is at the tip of a 20 pc molecular filament extending toward the galactic plane. A number of other star forming regions such as ρ Oph, NGC 7023, and S222 are found at the high latitude ends of filamentary molecular clouds. The velocity gradient of the S125 filament, averaged over its length amounts to 0.2 km s^{-1} pc^{-1}, roughly what can be produced by gravitational acceleration in the field of the galaxy (Spitzer 1978). Orthogonal to the plane, the z-component of the gravitational force (g_z = $-2x10^{-11}$ [z/pc] cm s^{-2}) gives rise to harmonic motion. Relative to S125 (z = 86 pc), the tip of the filament (z = 66 pc) attains a velocity of about 4.3 km s^{-1} due to differential acceleration. Gravitational field of the plane gives rise to an average velocity gradient of 0.22 km s^{-1} pc^{-1} over the length of the filament. If S125 is stationary and supported at its location in a magnetic well (Muschovias 1974, Spitzer 1978), neutral gas that has decoupled from the B-field would drip toward the plane with just the observed velocity. Projection effects caused by the relative orientation of the gas stream and the observers line of sight could introduce some error into this simple model.

5. S184

This source has a blueshifted CO component which fits the parameters expected of an ionization driven shock front. The highest electron density plasma in the nebula lies directly at the back of the molecular cloud where its pressure is expected to push the neutral gas toward the observer.

6. S155

The geometry of Ceph B is similar to S184. The CO profiles exhibit blueshifts whose position corelates well with the density of background ionized gas. At the cloud edge where the extinction and the amount of molecular gas is small, the CO line is shifted by as much as 6 km s^{-1} relative to the rest of the molecular cloud associated with Ceph OB3. The entire cloud fragment, Ceph B, has been accelerated to at least 2 km s^{-1}. Ceph B, like the hot spots in S125 appears to be externally heated, possibly by the photoelectric effect.

B. Destruction of Molecular Clouds by HII Regions

Giant molecular clouds can be destroyed in several ways; by conversion of gas into stars; by dissociation of H_2 into HI; by ionization and formation of HII regions; and by dispersal of the cloud into smaller cloudlets. The relative importance of these processes can be assessed by observation of evolved HII regions and associated molecular clouds. A number of such regions were studied in this thesis. A particularly clear example of cloud disruption is found in the case of S117, the Norh American and Pelican Nebulae.

The expanding shell surrounding S117 has been modeled as the last phase in the evolution of the post-shock layer associated with the expansion of the HII region. Once OB stars are born inside a molecular cloud the expansion of the high pressure HII gas sweeps up material behind a weak D-type shock front. Eventually the HII bubble reaches the nearest edge of the molecular cloud and bursts. Once the resulting rarefaction wave has reached the ionization front at the inner edge of the HII cavity, a streaming HII region is established which continues to push the shock front further into the cloud. Eventually the shock runs through the back of the cloud and accretion by the post shock layer ends. After this the rocket effect can accelerate the shocked gas layer. Model calculations for a homogeneous molecular cloud indicate that the current stage of evolution is reached between 3 to 6 million years after the onset of OB star formation. The ionizing flux of 5×10^{49} photons s^{-1} has ionized about $2 \times 10^{4} M_{o}$ of the original molecular cloud material. About $3\text{-}6 \times 10^{4}$ M_{o} of gas has been accelerated by the rocket effect to the escape velocity and will probably survive an episode of OB star formation as molecular cloud fragments.

The various cloud destruction mechanisms can be compared in a general way. Estimates of the star formation rate indicate that the conversion of gas into stars proceeds at a rate 1 to 5 M_{o} yr^{-1} in the entire galaxy (Mezger 1978, Scoville and Hersch 1979) corresponding to a mean rate of 330 to 1,700 M_{o} in 10^{6} yrs per cloud assuming a galactic population of 3,000 clouds (Solomon, Sanders, and Scoville 1980).

If the total amount of mass in molecular clouds is 2×10^9 M_o then between 50 and 250 M_o of gas are converted into stars for each 10^5 M_o of gas every million years. Dissociation, ionization, and dispersal are likely to occur only after an episode of OB star formation and the creation of an HII region. The damage caused by the evolution of an HII region (Lada, Blitz, and Elmegreen 1978) is greater than the effect of supernovae and stellar wind. The conversion of H_2 into HI is followed by ionization when gas flows through the ionization front at the HII region boundary. The conversion rate is controlled by the expansion of the HII region since the available flux of ionizing photons depends on the recombination rate in the ionized gas. From the equations governing the size of an HII region as a function of time and the Stromgren condition it follows that

$$\frac{dM}{dt} = 1.1 \times 10^{-9} \frac{Q^{2/3}}{n_o^{1/3}} \left(1 + 200 \frac{n_o^{2/3}}{Q^{1/3}} t \right)^{-1/7} \quad \text{gm s}^{-1}$$

where equality holds for a Stromgren sphere. For an HII region that has burst out of the molecular cloud and is density bounded on one side dM/dt can be 2 or 3 times greater since removal of ionized gas from the region between the star and the molecular cloud increases the flux of photons available at the I-front. For an O5 star ($Q = 5 \times 10^{49}$ photons s^{-1}) and a cloud of uniform density $n_o = 500$ cm^{-3}, $dM/dt \geq 2 \times 10^3$ M_o Myr^{-1}. Thus in 6 million years, the age of S117, the amount of gas destroyed by ionization is 1.2×10^4 M_o, close to the

observed ionized gas mass, and far in excess of the amount converted directly into stars.

A crude estimate of the conversion rate of H_2 into HII on a galactic scale can be made on the basis of the total ionization rate in the galaxy (Smith et al. 1978, Mezger 1978). Assuming that the flux of Lyman continuum photons responsible for ionization of all galactic HII regions is $Q = 4.7 \times 10^{52}$ s^{-1} (corresponding to 16% of all OB stars in the galaxy) the conversion rate for the galaxy is $dM/dt \simeq 2 - 6$ M_o yr^{-1}, (for $n_o = 500$ cm^{-3}) comparable to the mean star formation rate. For lower initial densities, the conversion rate increases. The mean rate at which gas is accelerated and dispersed is more difficult to estimate. In the case of the Pelican, the mass of the expanding shell is only slightly greater than the total mass of ionized gas, implying a mean disruption rate comparable to the ionization rate. Conversion of gas into the ionized state, and disruption appear to be the dominant modes of molecular cloud dispersal once OB star formation has occured. The total destruction rate of giant molecular clouds in the galaxy is the sum of the star formation rate, the H_2 - HII conversion rate, and the dispersal rate. This sum has a value around 3 to 20 M_o yr^{-1} implying a survival time scale of 10^8 yrs. for the giant molecular clouds in the galaxy.

A P P E N D I X I

THE SURVEY

The initial source list for this project included 50 objects selected from the list of Sharpless (1959) HII regions observed in the radio continuum by Felli and Churchwell (1972) with the 300 ft NRAO radio telescope. Although most of the selected sources were well isolated and strong, some weaker extended ones were included as well. Secondary selection was based on visual inspection of the Palomar Sky Survey. A number of sources not included on the basis of the radio data were entered into the list if the optical image indicated a morphology that would provide a good opportunity to probe the interaction between an HII region and the surrounding clouds. The availability of high resolution aperture synthesis maps from Westerbork prompted the inclusion of a number of sources, since this data gives a clearer picture of the distribution of the ionized gas. Although the final list (Table 12) was not intended to be representative of all nearby HII regions, it does represent a great diversity in morphology, excitation, and age.

Table 12 contains three lists; List 1 contains regions selected for the CO survey; List 2 contains sources that were studied in some detail and will be briefly mentioned in this appendix; List 3 gives the sources discussed in detail in Chapter 2.

Table 13 gives the survey results for those regions not investigated in detail. Column 1,2, and 3 give the source

TABLE 12

SOURCE LIST

List 1			List 2	List 3
S172	S53	S112	S252	S87
S173	S54	NGC 7129	S255	S106
S183	S62	S127	LkHα 208	S125
βCas	S64	S128	LkHα 101	S117
S187	S66	S151		S184
S188	S69	S152		S155
S206	S76	S132		
NGC 1333	S86	S135		
S228	S99	S141		
S235	S90	S142		
S261	S93	S146		
S36	S104	S168		
S46	DR15	S156		
S49	S105	S159		

TABLE 13

SURVEY SUMMARY

Source	α_{1950}	δ_{1950}	$\Delta\alpha$ (arcmin)	$\Delta\delta$ (arcmin)	V_{LSR} (km s^{-1})	ΔV (km s^{-1})	T_A (°K)	# spectra	Comments
S172	00 12 00	65 58 47	0	0	(-20,20)	-	<3	9	
S173	00 18 32	61 26 55	0	0	(-20,20)	-	<3	5	
S183	00 51 13	65 27 53	0	0	(-20,20)	-	<3	3	
β Cas	00 08 49	58 37 00	0	0	-0.5	1.5	8	5	
			0	3	0.0	1.0	8		
			0	-3	0.0	2.5	8		
S187	01 19 42	61 34 51	0	0	-14.8	3.0	22.5	9	
			0	-5	-14.5	3.0	18		
			0	-10	-14.5	2.5	12		
S188	01 27 17	58 13 42	0	0	-18	5.0	1.2	9	See below
S206	03 59 36	51 11 30	0	0	(-20,20)	-	<3	9	
NGC1333	03 26 00	31 06 18	0	0	10.0	3.0	12	3	

S228	05 10 00	37 23 30	0	0	-6.5	3.0	7.0	10
S235	05 37 36	35 48 52	0	0	-20.0	3.0	24	20
			0	-5	-17.0	2.0	20	
			3.7	0	-20.0	3.0	28	
			-3.7	0	-21.0	2.0	15	
			7.5	0	-19.0	4.0	20	
			-7.5	0	-20.0	1.0	14	
			30	0	-20.0	1.0	8	
S261	06 02 06	18 42 00	0	0	0.0	2.0	15	2
S36	16 03 16	00 30 00	0	0	2.0	2.0	9	8
			-7.5	0	2.0	1.0	9	
			7.5	0	2.0	1.0	10	
			0	7.5	2.0	1.5	11	
			0	15	2.0	2.0	7	
S46	18 03 10	-14 13 18	0	0	(-20,20)	-	<3	11
S49	18 16 07	-13 51 54	0	0	(10,50)	-	<4	6
			0	10	20.0	3.0	12	
			0	15	25.0	3.0	6	

S53	18 22 08	-13 16 00	0	0	50.0	20.0	10	5
S54	18 15 07	-11 51 54	0	0	(-10,30)	-	<3	9
			0	10	29.7	2.0	8	
			0	5	28.0	3.0	7	
S62	18 25 04	-04 08 12	0	0	(0,40)	-	<6	16
			2	14	13.0	3.0	15	
			0	20	12.0	1.5	12	
			7	14	12.0	2.0	10	
S64	18 28 52	-02 08 07	0	0	1.5	1.5	6	7
			0	10	1.0	1.5	5	
S66	18 45 00	-02 05 00	0	0	(-20,20)	-	<3	9
S69	18 41 54	00 22 45	0	0	(-20,20)	-	<3	3
S76	18 53 47	07 51 12	0	0	34.0	3.0	5	5
S86	19 41 26	23 16 17	0	0	(-20,20)	-	<3	14
S99	19 59 49	33 21 40	0	0	-24.0	4.0	6	12
			-7.5	0	-23.0	1.0	7	
			-15	0	-22.0	3.0	6	
			7.5	0	-23.0	3.0	10	

			0	5.0	-23.0	3.0	10		
S90	19 47 15	26 39 27	0	0	20.0	4.0	23	16	See below
			0	5	23.0	4.0	23		
			0	-5	19.0	1.0	6		
			5	0	19.0	3.0	20		
			-4	0	21.0	3.0	10		
S93	19 52 58	27 03 31	0	0	22.0	3.0	11	9	
			0	3	22.0	4.0	20		
			0	5	22.0	3.0	12		
			3	0	22.0	3.0	10		
			-3	0	22.0	2.0	6		
S104	20 16 04	36 36 00	4.7	0	0.0	4.0	12	5	
DR15	20 30 40	40 05 48	0	0	2.0	8.0	16	5	
S105	20 10 17	38 10 57	0	0	-3.5	1.0	6	5	See Below
			0	10	-3.5	1.0	6		
			-22.5	0	-3.5	1.0	5		
S112	20 32 09	45 27 41	0	0	-3.0	2.0	7	30	See Below
			-5	0	-3.0	3.5	15		

			10	0	-2.5	1.5	8	
			0	10	-1.5	4.0	9	
			0	-5	-2.0	5.0	8	
NGC7129	21 42 00	65 52 05	0	0	-10.0	2.0	16	13
			-5	0	-10.0	2.0	8	
			5	0	-10.0	2.0	9	
			0	2	-10.0	2.5	13	
			0	-2	-10.0	3.0	10	
S127	21 27 02	54 22 32	0	0	(-20,20)	-	<3	5
S128	21 30 34	55 39 04	0	0	8.5	1.0	7	16
			7.5	0	3.5	2.0	6	
			-7.5	0	9.5	2.0	8	
			0	2.5	7.5	1.0	8	
			0	-2.5	7.5	1.0	10	
S151	23 00 45	56 49 28	0	0	(-20,20)	-	<3	9
S152	22 56 39	58 31 17	0	0	(-50)	3.0	5	4
S132	22 17 42	55 53 20	0	0	(-50)	3.0	5	5
S135	22 20 16	58 27 54	0	0	-20.0	1.0	8	6

			0	5	-20.0	1.0	6	
			0	-5	-20.0	1.0	6	
S141	22 26 55	61 18 34	0	0	(-20,20)	-	<3	3
S142	22 45 32	57 47 09	0	0	(-20,20)	-	<3	3
S146	22 47 34	59 38 05	0	0	-49.0	6.0	10	3
S168	23 50 29	60 10 26	0	-4	-40.0	1.0	5	5
S156	23 03 05	59 58 48	0	0	-50.7	4.8	20	5
S159	23 13 11	60 50 20	0	0	-56.0	5.0	16	10

identification and the 1950 coordinates corresponding to ($\Delta\alpha = 0$, $\Delta\delta = 0$). Columns 4 & 5 give the offsets from the given R.A. and Dec in units of equatorial arcminutes (e.g. 1 minute of R.A. = 15' - no correction for foreshortening due to Declination being applied). Column 6 gives the velocities of detected lines. Since the intent of the survey was to identify nearby sources, the 1/4 MHz filterbank available in Spring 1978 was usually centered on $V_{LSR} = 0$; thus, for some sources there is no information outside the range (-20,20) km s^{-1} (this is indicated by the velocity range in parenthesis). Column 7 gives the detected line-widths. Column 8 gives calbrated (see Appendix 2) peak ^{12}CO antenna temperatures. Column 9 gives the total number of positions observed in each source. Not all observed spectra are tabulated; only representative spectra at well spaced positions are indicated if positive detections were made.

A. Comments on Individual Sources

1. S188

This object is a bright, red filamentary nebula that has a morphology similar to some supernova remnants. Radio observations, however, show a thermal spectrum (Israel and Felli 1978) and rule out the SNR interpretation. Comparison of the radio map with the PSS image suggests little foreground obscuration. The principle problem with this nebula is that no early type stars capable of exciting the nebulosity have been found.

During the survey, a weak but broad CO line was detected just outside the arc of nebulosity in S188. A similar line was found by Israel (1980). Since the line is weaker than 1°K, the line is probably thin, so the amount of gas is insufficient to hide an early type star capable of providing excitation to the nebula. The large linewidth of 10 km s^{-1} is unusual for such a weak line. A speculative suggestion is that S188 is a collisionally excited nebula at the interface between a low density cloud whose presence is indicated by the CO and a high velocity outflow, possibly from a stellar wind. The broad CO line may be formed in shocked cloud material under conditions similar to the broad CO feature seen at the periphery of the IC443 supernova remnant (DeNoyer 1979). Optical spectroscopy of the nebulosity to test the collisional excitation hypothesis as well as more extensive and sensitive mm wavelength observations should be carried out.

2. S105

This source, also known as NGC6888, is the stellar wind bubble generated by the WN6 star HD 122163 (Smith 1968, Crampton 1971). The excitation of the optical nebula is caused by collisions at the shock where the wind flow encounters ambient gas. Weak and narrow ^{12}CO emission is seen from the vicinity of this object. Unfortunately, it is impossible to determine the relative position of the CO emitting gas and the nebulosity. If the CO line is formed in the immediate vicinity of the bubble, the narow line width indicates that it has not

yet been affected by the disturbance caused by S105. Absence of broad CO emission indicates that: 1) There is no molecular gas in the vicinity of the bubble, or:(2) Molecular gas is mostly dissociated in the fast shock associated with the growing shell, or:(3) Even if CO is swept up and survives, it is too thin or beam diluted to generate an observable line.

3. S90

CO data on this source shows a strong velocity gradient consistent with cloud rotation. The gradient amounts to 0.7 km s^{-1} $arcmin^{-1}$ in R.A. and 0.4 km s^{-1} $arcmin^{-1}$ in Dec. At a kinematic distance of 2 kpc determined for this source, this implies a shear of about 1.4 km s^{-1} pc^{-1} with an angular momentum rotation vector oriented at position angle PA = 120°. Thus, if the shear is interpreted as rotation, its orientation is parallel to galactic rotation.

The molecular cloud lies to the SE of the associated optical nebulosity, in the same direction as the obscuration discernible on the PSS plates. Gas in the northern portion of the cloud (seen superimposed against the nebula) is redshifted relative to the center of mass; the cloud is moving toward the HII region. The ionized gas velocity of V_{LSR} = 22.5 km s^{-1} (Georgelin et al. 1973) as determined by Hα observations indicates that the nebula may be participating in the overall cloud rotation.

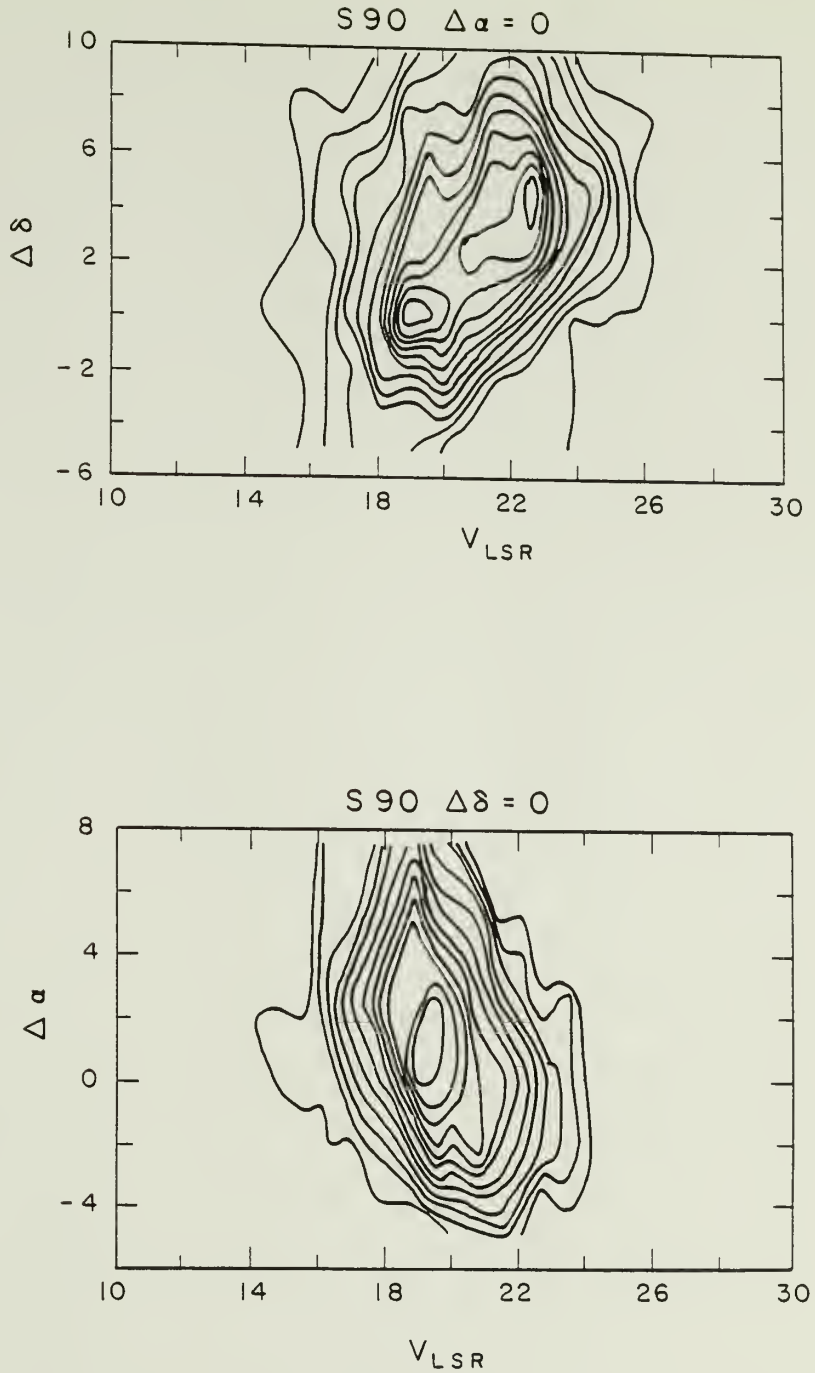

Figure 51

S90 east-west and north-south spatial velocity diagrams refered to the (0,0) position of $\alpha = 19^h47^m15^s$ and $\delta = 26°39'27''$.

4. S112

This cloud shows evidence of CO line broadening at the periphery of the HII region. The effect is shown in Figure 52 which presents a Dec. strip at $\Delta\alpha = 0$ through the HII region. The line becomes broadened at $\Delta\delta$ where the peak line temperature is reached. The isolated peak appears to be part of a more extended unrelated cloud seen in this direction.

5. LkHα 208

This object is a symmetric biconical nebula 2' in diameter located at the edge of a small molecular cloud that extends north-south for about a degree. Since the cloud is clearly outlined against the background of stars, its distance is considerably less than either S255 or S252 seen on the same PSS plate. A value of D = 1 kpc will be adopted (Good et al. 1980, Calvet and Cohen 1978, Cohen 1973). Although the nebula is not an HII region (most of its light is seen by reflection), it will be briefly discussed because of the possible presence of an edge on circumstellar disk that is responsible for the biconical structure. The CO mapping of the dust lane in the vicinity of LkHα 208 reveals a mild peaking of the temperature at the position of the nebula where T_A = 12 °K with the FCRAO dish.

A lunar occultation of LkHα 208, observed on April 19, 1980, revealed an abrupt jump in the CO intensity at the position of the central star (Good et al. 1980). The deconvolution of the half-

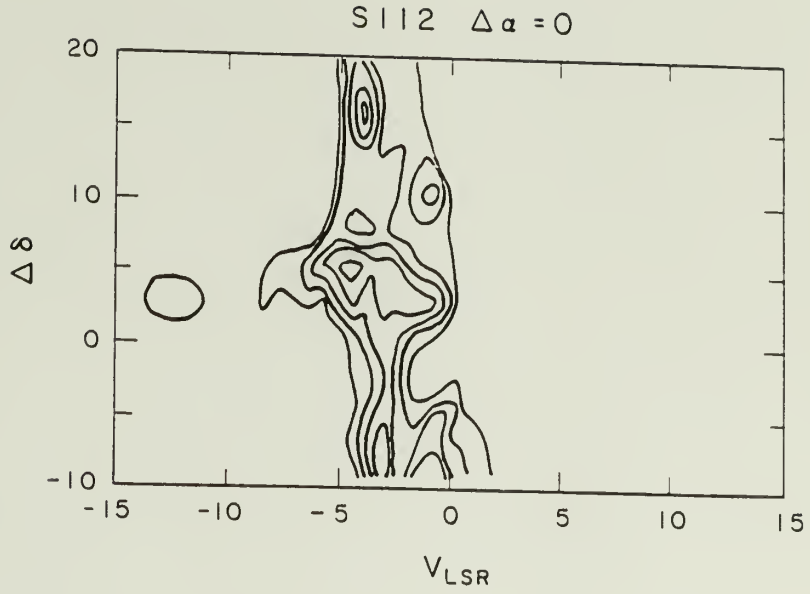

Figure 52

S112. A north-south SV diagram referenced to $\alpha = 20^h32^m09^s$ $\delta = 45°27'41"$. The increased line width at the center of the figure correlates with the edge of the ionized region.

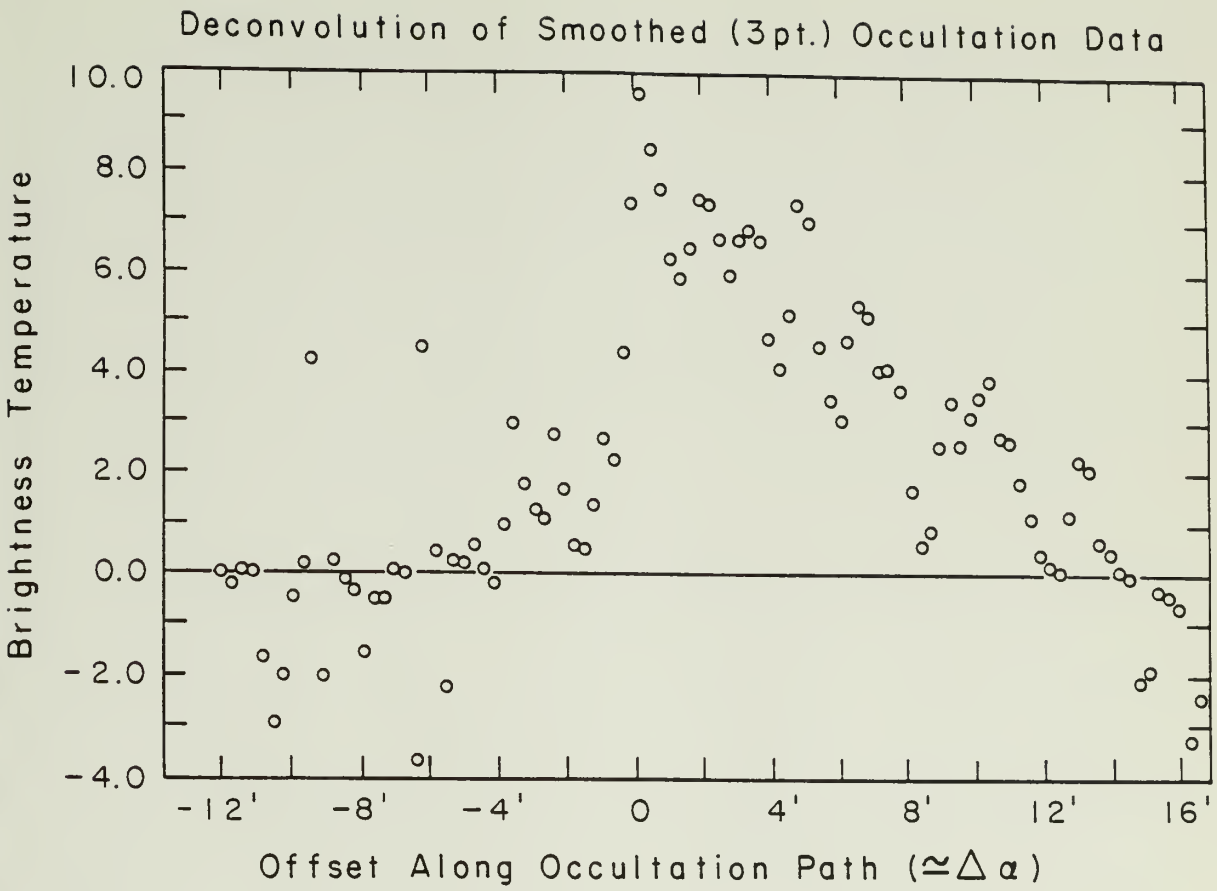

Figure 53

The integrated CO brightness distribution along the occultation path obtained by deconvolving the half gaussian telescope beam from the occultation data. The hottest point coincides with LkHα 208. Note the abrupt cloud edge seen at the position of the star. Low level CO emission is detectable to about $\Delta\alpha = -6'$ to the west.

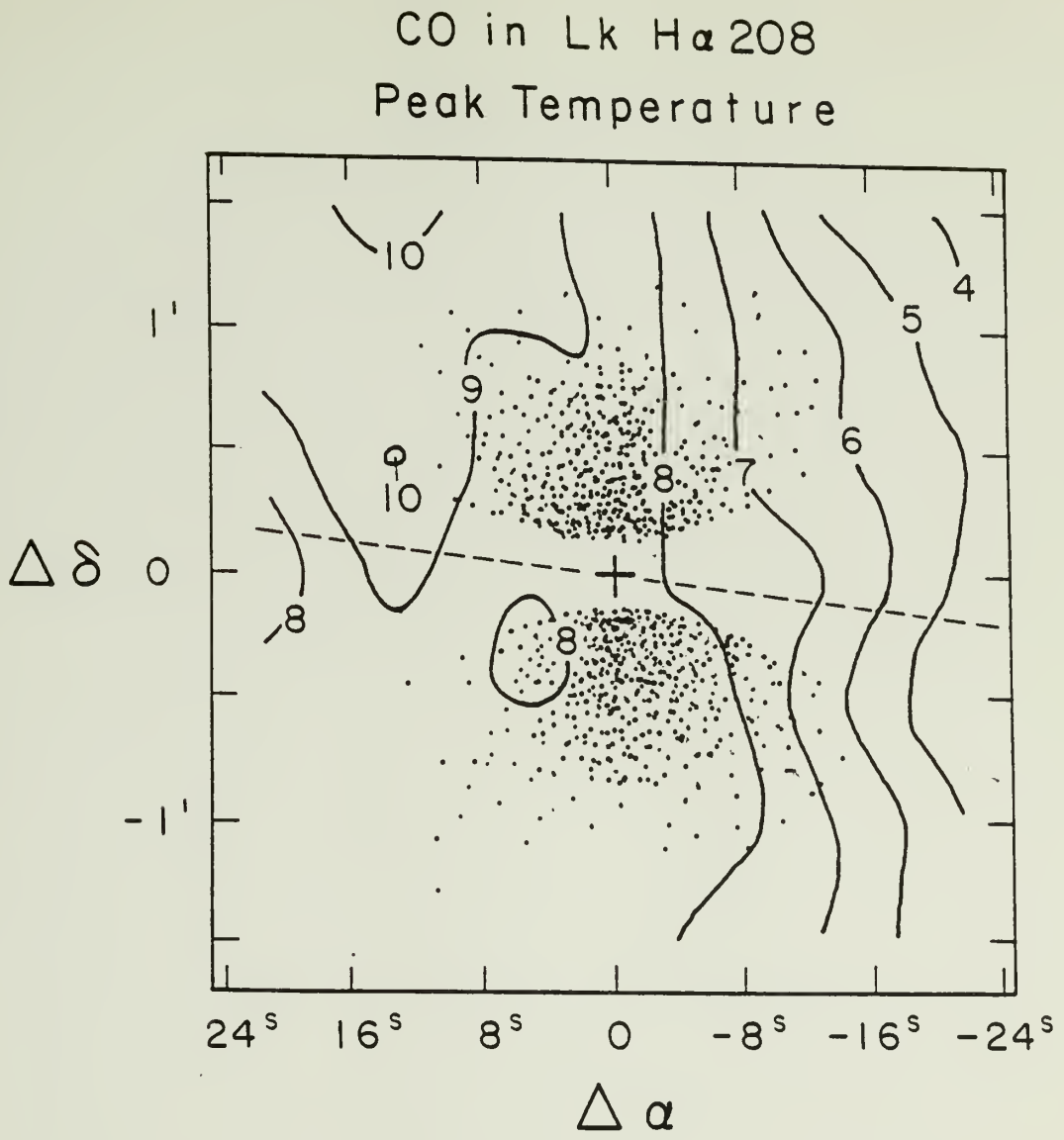

Figure 54

A ^{12}CO map showing a 3' region centered LkHα 208 (+). The shading (dots) illustrate the orientation and size of the biconical nebula seen on the PSS blue plate. The dotted line shows the direction of motion of the Moon during the 1980 occultation.

gaussian telescope beam from the data results in the intensity distribution along the occultation path shown in Figure 53. The spatial resolution of the data for this east-west strip, set by the sampling rate and the motion of the moon, was 17.5 arc-seconds, almost three times better than provided by normal single dish measurements. If the enhanced temperature seen in the data results from an elongated source 17 " wide and 44" (corresponding to the primary beam which determines the resolution orthogonal to the moon's path) long in the north-south direction, a temperature of T_A = 29 °K is implied for the strip as compared to T_A = 11°K for the ambient cloud. If the compact source is round with a 17" diameter, it would have to have a temperature of 40 °K in order to explain the occultation data.

The luminosity of the central star in LkHα 208 is not well determined due to a lack of far infrared measurements. Near infrared observations indicate a flat spectrum out to 20 microns (Cohen 1973). At a distance of 1 kpc, the derived luminosity of the central star below 20μ is about 90 L_o, considerably larger than expected for its spectral type, F0V (Calvet and Cohen 1978). This discrepancy has been ascribed to the pre-main sequence character of this object. If the spectrum continues to be flat out to 100μ, then the luminosity could be as high as 500 L_o. Assuming this upper value for the luminosity, dust at a distance of 1×10^{17} cm (corresponding to 1/2 the projected 17" beam at 1 kpc) from the star can be heated to a temperature of 35°K. Far infrared measurements of the central star and a determination of the neutral gas density in LkHα 208 are required in order to determine

the relative importance of dust and photoelectric heating in this source.

No evidence for a circumstellar disk in LkHα 208 has been found in the CO data. There is no evidence of an east-west oriented ridge, or velocity gradient as may be expected from the orientation of the shadowed region in the nebula. If a disk is present, it must be smaller than the beam size or lost, due to low contrast, against the emission of the larger cold cloud.

The ^{12}CO profiles exhibit a redshifted wing that does not appear in the ^{13}CO spectrum. The wing is detectable over an extended region to the south of LkHα 208 and is not seen in the direction of the dark cloud. The wing may represent gas that has been perturbed by the star, perhaps by a stellar wind.

6. S252

This is an old, low density, extended HII region ionized by the O6.5V star HD42088, located at a distance of about 2 kpc. Strong CO emission is found to be associated with three compact HII regions peaks A, C, and E (Felli et al. 1978). Partial mapping shows that all three hot spots are compact with a size of the same order as the 44" beam. A bright rim in the western part of the nebula (feature F in Felli et al. 1978) is assoiated with slightly enhanced CO temperatures and 1 to 2 km s^{-1} line broaddening. This region was mapped at Texas by Lada et al. (1978).

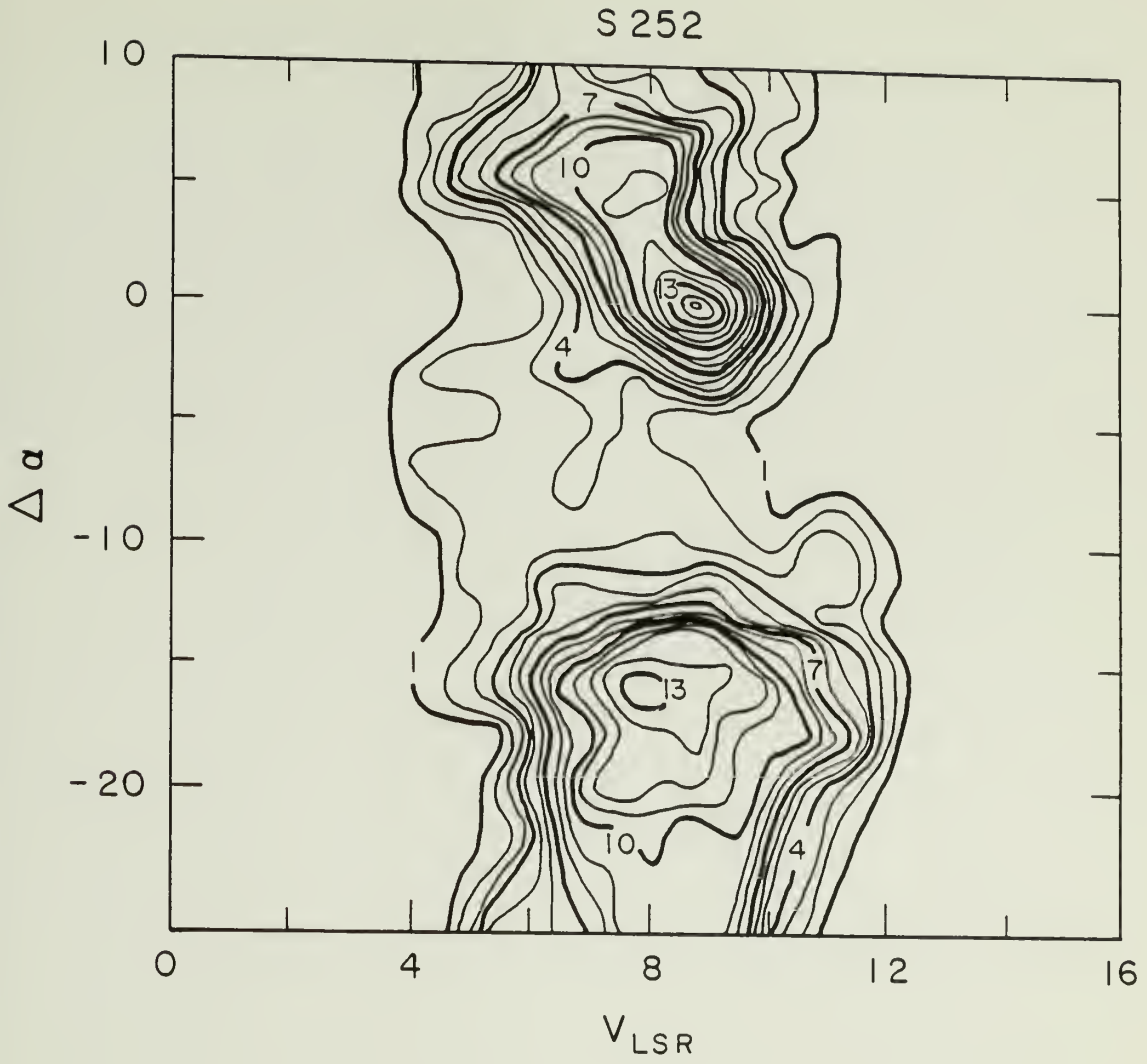

Figure 55

S252 showing an east-west spatial velocity diagram illustrating the temperature and line width enhancement encountered at the edge of the HII region. The upper hot spot is associated with the compact HII region S252 E. Reference coordinates are at $\alpha = 06^h06^m54^s$ $\delta = 10°30'55"$.

TABLE 14

S252 CO SOURCES

Source	α_{1950}	δ_{1950}	$T_A(^{12}CO)$
S252 A	06 05 33	20 39 50	22
S252 B	06 06 02	20 39 11	6
S252 C	06 06 23	20 40 07	18
S252 E	06 06 54	10 30 55	24
S252 F	06 06 11	20 29 02	18

7. S255

The S255 complex lies at the periphery of an extended extremely evolved supernova remnant, the Origem Loop (Berkhuijsen 1974). During the survey phase of this project, a 2°x2° region containing the radio continuum feature was observed in CO. Several molecular clouds, including the ones associated with S255, LKHα208, and an unnamed nebulasity 1.5° to the North-East of S255 were found. The S255 cloud was mapped by Evans et al. (1978) who discussed the energetics of the gas. It is difficult to draw any conclusions about a possible relationship between the SNR and the regions of star formation found associated with S255, LkHα208, and S261. The ages of the older HII regions are around 10^6 yrs. the same as the age found for the SNR. A 50 % error in the age determination of either the HII regions or the SNR could reverse any postulated cause and effect relationship.

During 1978-79 the hot spot in S255 was occulted by the Moon (Schloerb and Scoville 1979). Several R.A. strips cutting East-West across the cloud were observed in preparation for this occultation (Figure 56). The resulting spatial velocity diagram shows velocity shifts amounting to several km s^{-1}, just the amount expected for the relative motion between the ambient cloud and the ionization front driven post shock layer. The velocity shifts occur in discrete jumps whose position often coincides with the boundary of one of the HII regions in this complex. Since the shifts show a correlation with the distribution of ionized gas, and are of the right magnitude, it is

Figure 56

An S255 RA strip running east-west at the Declination of S255IRS The positions of the various HII regions encountered along this strip are shown at the left.

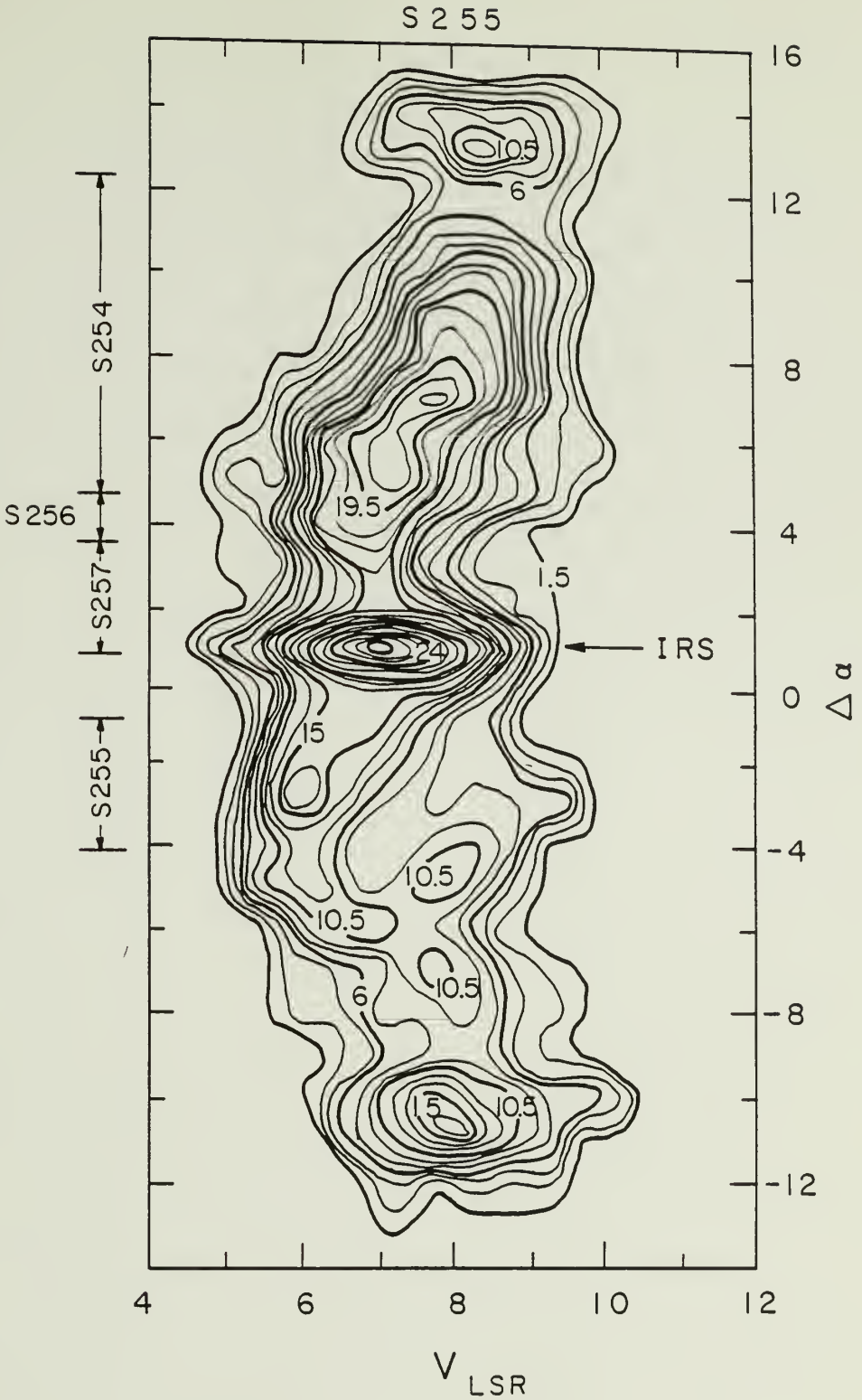
S 2 5 5
16
12
8
4
0
-4
-8
-12
Δ α
10.5
6
19.5
1.5
24
IRS
15
10.5
10.5
6
10.5
15
10.5
S254
S256
S257
S255
4
6
8
10
12
V LSR

reasonable to suggest that this is one more example of the dynamic consequence of the interaction between an HII region and the surrounding molecular gas.

8. LkHα 101 (S222)

This HII region is located in the center of a region of heavy obscuration just outside the California Nebula, NGC1499, that is excited by the runaway star ζ Per. A compact HII region (Brown et al 1976), indicates that the exciting star, LkHα101, is probably of spectral type B0. Near infrared observations have led Thompson et al. (1977) to conclude that the star is surrounded by a circumstellar or pre-planetary disk. CO observations by Knapp et al. (1976) indicate self-reversal in the molecular cloud.

The CO observations reported here consist of 150 ^{12}CO spectra of the central 16 arcminutes of the cloud. The cloud exhibiits complicated profiles (Figures 41 and 42) including several regions where multiple peaks in ^{12}CO are evident. (Lack of ^{13}CO spectra prevents further interpretation.) The contour map of the central region (Figure 57) shows several hot spots and complicated structure. The velocity field is complicated with no apparent systematic behavior. Figure 58 illustrates the kinematics along an East-West strip running through the central position. Further observations will be conducted in the near future in an attempt to understand the dynamics of these complicated region.

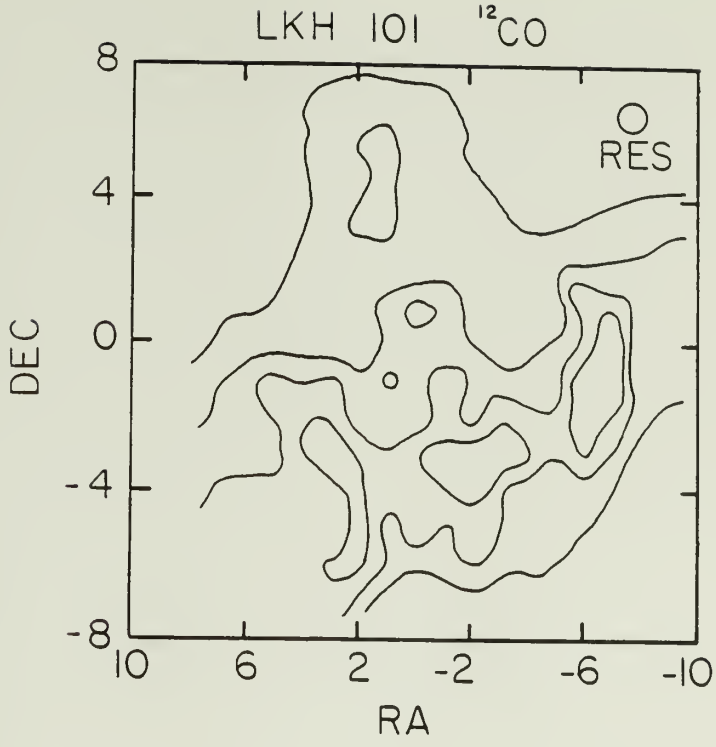

Figure 57

A ^{12}CO map of LkHα 101 (S222) centered on the reference position corresponding to $\alpha_{1950} = 04^h27^m00^s$ $\delta_{1950} = 35°10'12"$. Contour levels are at 4, 8, 12, and 16 °K.

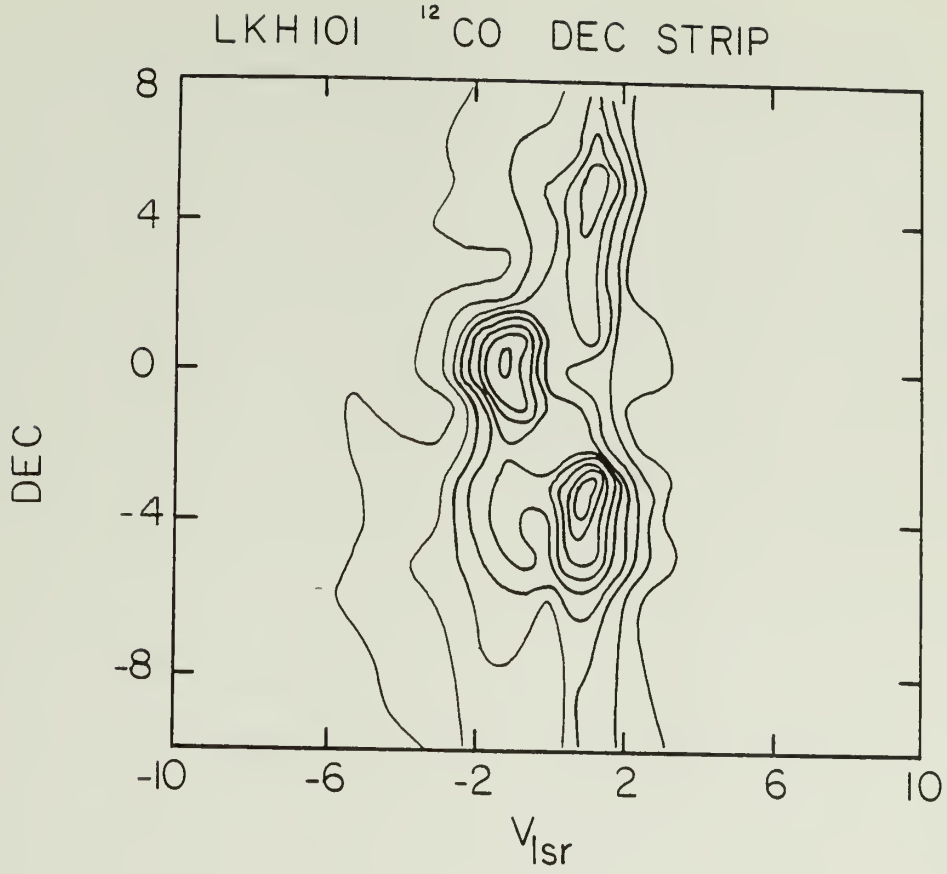

Figure 58

A north-south spatial velocity strip running through LkHα 101 at $\Delta\alpha = 0$ showing the clumpy distribution of CO emission. Contours are chosen at intervals of 2.5 °K.

APPENDIX II

OBSERVING AND REDUCTION METHODS

A. Data Acquisition

In this section a brief description of the data aquisition and reduction methods will be given. Between Winter 1978 when observations were started, and Spring 1980, a variety of frontends and backends were used. These are summarized in Tables 15 and 16.

Several calibration methods were employed during this period. Prior to March 1980, when a calibration chopper became available, a two step comparison scheme was used to calibrate the temperature scale. A standard position in each source was observed once every hour in order to track gain fluctuations in the system and variations in atmospheric transparency. All spectra obtained in an observing period were scaled with this gain curve in order to eliminate the time and elevation dependent effects. The temperature scale is established by observing one of several "standard" sources at elevations covered by the gain curve. The scaled spectra of a particular observing session were multiplied by the constant factor required to bring the standard source to the temperature given in Table 17. This method resulted in a calibration accuracy of about 20% for the ^{12}CO line. In March 1980, when the calibration chopper was mounted on the telescope, many of the reference positions used in calibrating the earlier CO maps were reobserved.

For fainter lines such as C_2H, HCN, and CS, a standard position could not be monitored in every source. Gain curves for the observing session were measured by repeated observations of the brighter sources such as Orion A. Calibration uncertainties for these transitions are somewhat larger than for ^{12}CO .

A number of observing modes, including position switching and frequency switching, were used during different phases of observing. Initially, only position (beam) switching was available. Typically, a spectrum was obtained by observing an emission free region for 30 seconds, then the source for 30 seconds, and repeating the cycle 3 to 10 times. In Winter 1979, frequency switching became available and was used for narrow line sources. This method was particularly useful when observing sources in the inner galactic plane where emission-free regions are difficult to locate. The local oscillator (klystron) was stepped 5 to 15 MHz between 2 and 10 times each second in order to obtain the reference portion of each observing cycle. When possible, the system was configured so that the spectral line appeared in the backend during both "source" and "reference" portions of the cycle, separated by the LO offset frequency. Folding of the spectrum would result in an effective increase of a factor of two integration time (at the expense of a factor of two smaller usable bandwidth) since the line was detected during both halves of the observing cycle. Frequency switched data suffers from incomplete cancellation of standing waves which show up as a sinusoidal ripple in the baseline. Two methods can be used to surpress baseline ripple: 1) A phase modu-

TABLE 15

FRONTEND PARAMETERS

Description	Frequency	Dates Used	SSB Receiver Temperature
Bonn Receiver*	2 - 3 mm CO, CS(2-1)	Feb 1978 - May 1978	800 °K - 1100 °K
FCRAO 3mm room temp mixer	80 - 100 GHz CS(2-1),HCN,C_2H	Oct 1978 - Jan 1980	1100 °K - 1600 °K
FCRAO 2mm room temp mixer	110 - 115 GHz CO	Dec 1978 - Mar 1980	1200 °K - 1800 °K
FCRAO 7mm room temp mixer	40 - 50 GHz CS(1-0)	Oct 1979 - Jan 1980	600 °K - 1000 °K
FCRAO cooled mixer	115 GHz	Mar 1980 - May 1980	500 °K - 600 °K

* on loan from the Max Planck Institute for Radioastronomy, Bonn

TABLE 16

BACKENDS

Description	number of channels	bandwidth per channel	total bandwidth	Dates Used
meter wave 1/4 MHz	64	1/4 MHz	16 MHz	Feb 1978 - May 1978
Autocorrelator	128 - 256	< 0.04 MHz (variable)	< 10 MHz (variable)	Sept 1978 - May 1980
1 MHz filterbank	256	1 MHz	256 Mhz	Feb 1978 - May 1980
filterbank #1	256	1/4 MHz	64 MHz	Jan 1980 - May 1980
filterbank #2	256	1/4 MHz	64 MHz	Mar 1980 - May 1980

TABLE 17

CALIBRATION SOURCES

Source	α_{1950}	δ_{1950}	Assumed T_A
Orion A	$05^h32^m47^s$	-05°24'28"	$T_A(^{12}CO) = 70$ °K
DR21	$20^h37^m14^s$	42°08'50"	$T_A(^{12}CO) = 28$ °K
W3	$02^h21^m51^s$	61°52'19"	$T_A(^{12}CO) = 28$ °K
W51	$19^h21^m22^s$	14°24'45"	$T_A(^{12}CO) = 30$ °K
M17SW	$18^h17^m27^s$	-16°14'54"	$T_A(^{12}CO) = 40$ °K

lator that consists of a segmented, rotating 1/4 wave plate (Goldsmith and Scoville 1979) randomizes the phase of the standing wave during the observation. 2) An emission free region is observed with the frequency switching technique to obtain a spectrum containing only baseline ripple. A soothed version of this reference spectrum (generated by running a Hanning smoothing function through the spectrum with a length scale of 8 km s^{-1}) is subtracted from each spectrum prior to folding. The resulting baselines are generally good so long as the reference position and the spectrum are observed within 10 minutes of each other. A combination of methods 1 and 2 resulted in the most reliable observations obtaiable with frequency switching. For observations requiring exceptional baseline stability (such as long integrations used in searching for faint line wings), a double position switching mode was used in which the "on" portion of the observing cycle is bracketted by the "off" position observations.

When the cooled receiver became available, an automatic mapping program became available that would automatically carry out all the reference position and on position observations. In the frequency switching mode this routine was used to obtain an emission free reference spectrum every 5 observations that could be subtracted from the data to yield stable baselines. High quality, uniformly sampled maps were obtained with this routine. A number of sources were remapped, resulting in considerable redundancy that served as a check on the accuracy of the results.

All data processing was performed at Quabbin using the SPECTRA data reduction program. After scaling and calibration, spectra obtained at the same position on the sky were averaged to yield better signal-to-noise ratios. When different backends were used, the spectra were interpolated and resampled (using the GENerate function) at the lower resolution. First-order baselines were fit and subtracted prior to the evaluation of the spectral line parameters (peak temperature, integral under the line, etc.) which were used in generating maps. Spatial velocity diagrams were generated from the calibrated and reduced data sets.

B. Mass Estimates from CO Observations

CO column densities are computed from the line observations according to the formulae reviewed by Solomon (1978) (see also Scoville and Solomon 1973). The optical depth of ^{13}CO is computed from

$$\tau(^{13}CO) = \ln \left(\frac{1}{1 - T_A{}^{13} / T_A{}^{12}} \right)$$

where $T_A{}^{13}$ and $T_A{}^{12}$ are the peak ^{12}CO and ^{13}CO line temperatures scaled to above the atmosphere. The column density of ^{13}CO is then given by

$$N(^{13}CO) = 2.8 \times 10^{14} \frac{\tau(^{13}CO)\left(T_{1-0} + 1 \right) \Delta V}{1 - \exp\left(-5.5 / T_{1-0} \right)}$$

where ΔV is the HPFW of the ^{13}CO line. It is assumed that the excitation temperature, T_{1-0}, is equal to the rotational temperature (used in computing the partition function), which in turn is equal to the gas kinetic temperature. Since the ^{12}CO line is usually thermalized and optically thick, $T_A{}^{12}$ is a good measure of T_{1-0}.

There has been a great deal of argument over the factor to be used in converting ^{13}CO column densities into H_2 column densities (Dickman 1979). Here we use $N(H_2) = 10^6\ N(^{13}CO)$, following Solomon Sanders, and Scoville (1980), which corresponds to 15% of all available carbon being locked up in CO and an isotopic ratio $[^{13}C]/[^{12}C] = 1/89$. Conversion of H_2 column densities into a cloud mass entails dividing the cloud into shells of constant column density as determined by mapping. The mass is obtained by multiplying the area of each zone by its column density and summing all zones.

An independent check on the mass is obtained by computing a Virial mass given by

$$M \sim 0.5\ \frac{R_c(\Delta V)^2}{G}$$

In regions where shocks and other sources of disturbance occur, the Virial mass will be very different from the true mass if gravity does not dominate the dynamics. The factor of two agreement between Virial and CO mass estimates found for most of the clouds studied suggests

that most molecular gas in clouds associated with HII regions is still gravitationally bound. External disturbances affect the gas only in a mild manner; a notable exception to this is the Pelican Nebula (S117).

BIBLIOGRAPHY

Allen,C.W. (1973) Astrophysical Quantities,(Athlone Press,London).

Ambartsumian,V.A. (1954) Bull.Obs.Bynrokan,15,3.

Becklin,E.E,Matthews,K.,Neugebauer, and G.,Willner,S.P. (1978)Ap.J.,220,831.

Beer,A. (1964) M.N.R.A.S.,261.

Beichman,C.,Wynn-Williams,C.G.,and Becklin,E.E. (1979) Ap.J.,232,L47.

Berkhuijsen, E.M. (1974) AA,35,429.

Blaauw,A. (1964) Ann.Rev.Astr.and Astroph.,2,213.

Blaauw,A.,Hiltner,W.A., and Johnson,H.L. (1959) Ap.J.,130,69.

Black,D.C., and Bodenheimer,P. (1975) Ap.J.,199,619.

Black,J.H., and Dalgarno,A. (1977) Ap.J.,236,598.

Blair,G.N.,Davis,J.H., and Dickinson,D.F. (1978) CFA preprint #957.

Blair,G.N.,Evans,N.J., and Van den Bout,P.A. (1975) Ap.J.,200,L161.

Blitz,L. (1978) Ph.D. Thesis, Columbia University,N.Y.

Blitz,L., and Lada,C.J. (1979) Ap.J.,227,152.

Bodenheimer,P., and Black,D.C. (1978) in Protostars and Planets,ed. T.Gehrels (U.of.A. Press).

Bodenheimer,P.,Tenorio-Tagle,G., and Yorke,H.W. (1980) preprint.

Bohlin,R.C. (1975) Ap.J.,200,402.

Brown,R.L.,Broderick,J.J., and Knapp,G.R. (1976) M.N.R.A.S.,175,87P.

Burton,W.B., and Gordon,M.A.(1976) Ap.J.,207,L189.

Calvet,N., and Cohen,M.(1978) M.N.R.A.S.,182,687.

Castor,J.,McCray,R., and Weaver,R.(1975) Ap.J.,200,L107.

Caswell,J.L. (1968) A.J.,73,949.

Cesarsky,C.J.,Cesarsky,D.A.,Churchwell,E., and Lequeux,J. (1978) A.A.,68,33.

Cohen, M. (1979) private communication.

Cohen,M. (1973) M.N.R.A.S.,164,395.

Cohen,M., and Kuhi,L. (1979) Ap.J.Supp.,41,743.

Cong,H.Y. (1976) Ph.D. Thesis,Columbia University.

Crampton,D. (1971) M.N.R.A.S.,153,303.

Crawford,A.N., and Barnes,J.V. (1970) A.J.,75,952.

Dalgarno,A., and McCray,R.A., (1972) Ann.Rev.Astr.Astroph.,10,375.

Deharveng,L., and Maucherat,M. (1978) A.A.,70,19.

deJong,T. (1977) A.A,55,137.

deJong,T. (1980) preprint.

DeNoyer,L. (1979) Ap.J.,232,L165.

Dickman,R.L. (1979) Ap.J.Supp.,37,407.

Dieter,N. (1967) Ap.J.,150,435.

Downes,D.,Rinehart,R. (1966) Ap.J.,144,937.

Draine,B.T. (1978) Ap.J.Supp.,36,595.

Dyson,J.E. (1868) Astroph. & Space Sci.,1,388.

Dyson,J.E. (1973) A.A.,23,381.

Eiroa,C.,Elsasser,H., and Lahulla,J.H. (1979) A.A.,74,89.

Elias,J.H. (1978) Ap.J.,223,859.

Elmegreen,B.G.,Dickinson,D.F.,and Lada,C.J. (1978) Ap.J.,220,853.

Elmegreen,B.G., and Lada,C.J. (1978) Ap.J.,219,467.

Elmegreen,B.G., and Lada,C.J.(1977) Ap.J.,214,725.

Elmegreen,B.G., and Moran,J.M. (1979) Ap.J.,227,L93.

Evans,N.J.,Blair,G.N., and Beckwith,S. (1977) Ap.J.,217,448.

Evans,N.J.,Becklin,E.E.,Beichman,C.,Gatley,Ian,Hildebrand,R.H.,
Keene,J.,Slovak,M.H.,Werner,M.W.,Whitcomb,S.E. (1980) preprint.

Felli,M., and Churchwell,E.(1972) A.A.Supp.,5,369.

Felli,M.,Habing,H.J., and Israel,F.P. (1978) A.A.,59,215.

Felli,M., and Harten,R.H. (1978) Westerbork preprint.

Felli,M.,Tofani,G.,Harten,R.H., and Panagia,N. (1978) A.A.,69,199.

Field,G.B.(1978) in Protostars and Planets ed. T.Gehrels (U.of A.
Press,Tucson).

Flannery,B.P.,Roberge,W., and Rybick,G.B., (1980) Ap.J.,236,598.

Genzel,R., and Downes,D.(1977) A.A.Supp.,30,145.

Georgelin,Y.M. (1975) Ph.D. Thesis, Universite de Province.

Georgelin,Y.P.,Georgelin,Y.M., and Roux,S. (1973) A.A.,25,337.

Goldreich,P., and Kwan,J. (1974) Ap.J.,189,441.

Goldsmith,P.G., and Langer,W.D. (1978) Ap.J.,222,881.

Goldsmith,P.G., and Linke,R. (1980) preprint.

Goldsmith,P.G., and Scoville,N.Z. (1979) preprint.

Good,J.,Schloerb,P.,Scoville,N.Z., and Bally,J. (1980) in preparation.

Goudis, C. (1976a) Astr.& Space Sci.,39,173.

Goudis, C. (1976b) Astr.& Space Sci.,44,281.

Goudis,C., and Johnson,P.G. (1978) A.A.,63,259.

Habing,H.J. (1968) B.A.N.,19,421.

Habing,H.J., and Israel,F.P. (1979) Ann.Rev.Astr.and Astroph.,17,345.

Herbig,G. (1958) Ap.J.,128,259.

Herbig,G. (1959) Ap.J.,130,57.

Herbig,G., and Kuhi,L. (1963) Ap.J.,137,398.

Herbst,W., and Assousa,G.E.(1977) Ap.J.,217,473.

Hogg,H.S. (1959) Handuck der Physik,ed.S.Flugge
(Berlin:Springer-Verlag) 53,194.

Huntress,W.J., and Prassad,S.S. (1980) Ap.J.Supp.,43,1.

Israel,F.P. (1978) A.A.,60,233.

Israel,F.P. (1978) A.A.,60,233.

Israel,F.P. (1979) private communication.

Israel,F.P., and Felli,M. (1978) A.A.,63,325.

Kahn,F.D. (1954) B.A.N.,12,187.

Kandel,R.S., and Sibille,F. (1978) A.A.,68,217.

Knapp,J.R.,Kuiper,T.B.H.,Knapp,S.L., and Brown,R.L. (1976) Ap.J.,206,493.

Kurutz,R.L. (1979) Ap.J.Supp.,40,1.

Kutner,M.,Tucker,K.D.,Chin,G., and Thaddeus,P.(1977) Ap.J.,215,521.

Kwan,J., and Scoville,N.Z. (1976) Ap.J.,206,718.

Lada,C.J., and Wooden,D. (1978) Ap.J.,232,158.

Lada,C.J., and Harvey,P. (1980) preprint.

Lada,C.J., and Black,J.H. (1978) Ap.J.,203,L75.

Lada,C.J.,Blitz,L., and Elmegreen,B.G. (1978) in Protostars and Planets;ed
T. Gehrels

Lada,C.J., and Elmegreen,B.G. (1979) A.J.,84,336.

Lada,C.J.,Elmegreen,B.G.,Cong,H.,Thaddeus,P. (1978) Ap.J.,226,L39.

Landau,L.D., and Lifshitz,E.M. (1959) Fluid Mechanics, Pergamon Press,Paris.

Langer,W. (1979) private communication.

Langer,W., (1976) Ap.J.,206,699.

Lasker,B.M. (1966) Ap.J.,143,700.

Liszt,H.T. (1973) Ph.D. Thesis, Princeton University.

Little,L.T.,Macdonald,G.H.,Riley,P.W., and Matheson,D.N. (1979) M.N.R.A.S.,188,429.

Loren,R.B. (1976) Ap.J.,209,466.

Lucas,R.,LeSqueren,A.M.,Kazes,I., and Encrenaz,P.J. (1978) A.A.,66,155.

Martin,R.N., and Barrett,A.H. (1978) Ap.J.Supp.,36,1.

Mathews,H.E.,Baars,J.W.M.,Wendeker,H.J., and Goss,W.M. (1977) A.A.,55,1.

Mathews,W.G. (1969) Ap.J.,157,583.

Mathews,W.G., and O'Dell,C.R. (1969) Ann.Rev.Astr.and.Astroph.,7,67.

Maucherat,A.J. (1975) A.A.,45,193.

Meaburn,J. (1971) A.A.,13,110.

Merril,K.M. (1980) private communication.

Milman,A.S. (1975) Ap.J.,202,673.

Milman,A.S.,Knapp,G.R.,Kerr,F.J.,Knapp,S.L., and Wilson,W.J. (1975) A.J.,80,93.

Munch,G. (1958) Rev.Mod.Phys.,30,1035.

Muschovias,T.Ch. (1974) Ap.J.,192,37.

Muschovias,T.Ch. (1976) Ap.J.,206,753.

Oort,J.H. (1954) B.A.N.,12,177.

Oort,J.H., and Spitzer,L. (1955) Ap.J.,121,6.

Osterbrock,D.E. (1974) Astrophysics of Gasseous Nebulae, W.H.Freeman & Co.,(San Francisco)

Penzias,A.A. (1975) in Atomic and Molecular Physics and the Interstellar Medium,ed.R.Balian,P.Encrenaz,J.Lequeux

Penzias,A.A.,Solomon,P.M.,Jefferts,K.B., and Wilson,R.W. (1972) Ap.J.,174,L43.

Pipher,J.L.,Sharpless,S.,Savedoff,M.P.,Keridge,S.J.,Krassner,J., Schurmann,S.,Soifer,B.J., and Pottasch,S. (1958) B.A.N.,14,29.

Pottasch,S. (1958) B.A.N.,14,29.

Price,S.D., and Walker,R.G. (1976) AFGL Four Color Sky Survey, AFGL-TR-76-0208.

Riegel,K.W. (1967) Ap.J.,148,87.

Rodriguez,L.F.,Moran,J.M.,Ho,P.T.P.,and Gottlieb, E.W. (1980) Ap.J., 235,845.

Rodriguez,L.F.,Ho,P.T.P., and Moran,J.M. (1980) preprint.

Sargent,A. (1977) Ap.J.,218,736.

Sargent,A.N. (1979) Ap.J.,233,163.

Schloerb,P., and Scoville,N.Z. (1979) Ap.J.,235,L33.

Schmitz,M.,Brown,L.W.,Mead,J.M., and Nagy,T.A. (1978) Merged Infrared Catalog,NASA Technical Memorundum 79683.

Scoville,N.Z., and Herch,K. (1979) Ap.J.,229,578.

Scoville,N.Z., and Kwan,J. (1976) Ap.J.,210,L39.

Scoville,N.Z., and Solomon,P.M. (1973) Ap.J.,180,31.

Scoville,N.Z., and Solomon,P.M. (1974) Ap.J.,187,L67.

Scoville,N.Z., and Solomon,P.M.(1975) Ap.J.,199,L105.

Sharpless,S. (1959) Ap.J.Supp.,4,257.

Sibille,F.,Bergeat,J.,Lunel,M., and Kandel,R. (1975) A.A.,40,441.

Simonson III,C.S., and Someren-Greve,H.W. (1976) A.A.,49,343.

Smith,L.F. (1968) in Wolf-Rayet Stars; ed.Gelbie,K.B.,Thomas,R.N.

Smith,L.F.,Biermann,P., and Mezger,P.G. (1978) A.A.,66,65.

Snell,R. (1979) Ph.D. Thesis, University of Texas at Austin.

Solomon,P.M. (1978) in Infrared Astronomy; ed.Setti,G.,Fazio,G.G. (Reidel).

Solomon,P.M.,Sanders,D.B., and Scoville,N.Z.(1980) in preparation.

Spitzer,L. (1978) Diffuse Matter in Space, Interscience.

Tenorio-Tagle,G. (1979) A.A.,71,59.

Tenorio-Tagle,G.,Yorke,H.W., and Bodenheimer,P. (1980) preprint.

Thompson,R.I,Strittmatter,P.A.,Erickson,E.F.,Witterborn, and Strecker,D.W. (1977) Ap.J.,218,170.

Walker,M.F. (1959) Ap.J.,130,57.

Watson,W.D. (1972) Ap.J.,176,103.

Weaver,R.,McCray,R.,Castor,J.,Shapiro,P., and Moore,R. (1977) Ap.J.,218,377.

Welin,G. (1973) A.A.Supp.,9,183.

Wendeker,H. (1968) Zs.f.Ap.,68,368.

Wilson,O.C.,Munch,G.,Flather,E.M., and Coffeen,M.F. (1959) Ap.J.Supp.,4,199.

Wilson,W.J.,Schwartz,P.R.,Epstein,E.Z.,Johnson,W.A.,Etcheverry,R.D., Mori,J.J.,Berry,G.G., and Dyson,H.B. (1974) Ap.J.,191,357.

Woltjer,L. (1972) Ann.Rev.Astr. & Astroph.,10,129.

Woodward,P.R. (1978) Ann.Rev.Astr.and Astroph.,16,555.

Woodward,P.R.(1976) Ap.J.,207,484.

Zuckerman,B.,Kuiper,T.B.H., and Rodriguez-Kuiper,E.N. (1976)
Ap.J.,209,L137.